Light management strategies to tackle incomplete absorption in ultrathin CIGS solar cells

Rui Bastos
Master in Engineering Physics
Department of Physics and Astronomy
Faculty of Sciences of University of Porto & Faculty of Engineering of University of Porto
2026

Light management strategies to tackle incomplete absorption in ultrathin CIGS solar cells

Rui Bastos

Dissertation carried out as part of the Master in Engineering Physics

Department of Physics and Astronomy

2026

Supervisor
Dra. Jennifer Teixeira, Research Scientist, International Iberian Nanotechnology Laboratory (INL)

Co-supervisor
Prof. Dr. João Ventura, Principal Researcher, Faculty of Sciences of University of Porto



Acknowledgements

Em primeiro lugar, gostaria de agradecer ao Pedro Salomé por me ter possibilitado esta oportunidade de trabalhar a minha tese no grupo e no INL. Foi uma experiência enriquecedora, um ano do qual levarei inúmeras memórias e aprendizagens. Gostaria de agradecer à Jennifer por todo o apoio durante a tese, sempre disponível para qualquer dúvida ou ajuda que precisasse. Facilitou-me imenso este percurso e estou bastante agradecido. Também gostaria de agradecer ao João Ventura por ter acompanhado a tese ao longo de todo o processo, enviando sugestões e tendo vindo ao INL regularmente. Gostaria de agradecer também ao Enzo, que me introduziu a todos os processos de fabrico na sala limpa e ao ambiente no INL. Ganhei bastante rotina de trabalho, um *brutal* gosto pela nanofabricação, e perdi mais de 30€ em apostas menos sensatas. Por fim, gostaria de agradecer a todo o grupo do NOA por todo o apoio que me deram, em especial ao António, Fernandes, Vilão, Ana Rita e Xavier. Ao Fontoura, Afonso, Jaime, Manuel, Ricardo, por estes 5 anos e pelos restantes ainda. Aos meus avós por todo o carinho e suporte que sempre me deram. À minha Aninha por todo o apoio que me deu, ajudou-me em todos os momentos que tive, mais fáceis ou mais difíceis, e sempre me motivou a fazer mais e melhor, obrigado por tudo. Agradecer aos meus irmãos que, apesar de chatos, no final de contas, sou o único irmão do meio que eles têm. Sem eles não teria a paciência que tenho hoje, e por isso obrigado. Por fim, agradecer aos meus pais por todo o apoio que me deram toda a minha vida, sem eles não teria sido possível, este mestrado também é deles.

This work was funded under project Hi-BITS, grant agreement 101122203 funded by the European Union. Views and opinions expressed are, however, those of the author(s) only and do not necessarily reflect those of the European Union or CINEA. Neither the European Union nor the granting authority can be held responsible for them.

The work developed in this Thesis was financially supported through the project ”R2U Technologies - modular systems” (C644876810 00000019), supported by Component C5– Capitalisation and Business Innovation, under the Portuguese Resilience and Recovery Plan, through the NextGenerationEUFund.



Resumo

Esta tese focou-se no desenvolvimento de processos de nanofabricação reprodutíveis para estratégias de manipulação de luz no contacto traseiro para melhorar o desempenho de células solares Cu(In,Ga)Se_2 (CIGS) ultrafinas, em substratos flexíveis e rígidos. Litografia por nanoimpressão foi utilizada devido à sua escalabilidade e compatibilidade com a indústria. Um processo de fabricação de nanopilares de SiO_x em substratos flexíveis de aço inoxidável (INOX)/TiW/MoNa/Mo foi desenvolvido e otimizado. Caracterização ótica revelou um aumento na refletância difusa após integrar as estruturas de SiO_x, indicando melhor dispersão de luz e potencial para uma melhoria do comprimento do percurso ótico. Um estudo foi realizado para investigar as perdas de absorção através da diminuição da espessura da camada absorvente, mostrando uma redução da densidade de corrente curto-circuito com o decréscimo da espessura da camada absorvente. As estruturas fabricadas foram integradas em células solares CIGS ultrafinas. Apesar de uma melhoria no desempenho ótico na região do infravermelho próximo, os dispositivos mostraram degradação do desempenho elétrico. Análise de microscopia eletrónica de varrimento (MEV) sugeriu que as nanoestruturas disromperam a morfologia do crescimento de CIGS, contribuindo para maiores perdas elétricas. Para aplicações bifaciais, arranjos de nanopilares de Au encapsulados por um dielétrico foram desenvolvidos em substratos de vidro sodo-cálcico revestidos por ITO. Diferentes arquiteturas de pilares, materiais dielétricos, e geometrias de abertura de contacto foram fabricados e otimizados. Caracterização morfológica por MEV e microscopia de força atómica (MFA) confirmou a bem-sucedida fabricação das estruturas pretendidas. Medidas óticas mostraram um aumento na transmitância e refletância difusa relativamente às referências lisas de ITO, demonstrando as capacidades de dispersão de luz das nanoestruturas. A integração de nanopilares de Au encapsulados em substratos flexíveis de INOX/TiW/MoNa/Mo foi estudada. Apesar de um processo de nanofabricação completo não ter sido alcançado, foi demonstrado que o encapsulamento dielétrico preveniu efetivamente a difusão de Au para a camada absorvente. Em suma, os resultados demonstraram o potencial das interfaces traseiras nanoestruturadas para melhorar manipulação de luz em células solares CIGS ultrafinas, realçando os desafios associados com preservar o desempenho elétrico do dispositivo após integração.

Palavras-chave: nanofabricação, manipulação de luz, camada absorvente ultrafina, células solares CIGS

Abstract

This thesis focused on the development of reproducible nanofabrication process flows for rear light-management structures to improve the optical performance of both flexible and rigid ultrathin Cu(In,Ga)Se_2 (CIGS) solar cells. Nanoimprint lithography was employed due to its scalability and compatibility with industrial approaches. A process flow for the fabrication of SiO_x nanopillars on flexible stainless steel (SS)/TiW/MoNa/Mo substrates was developed and optimized. Optical characterization revealed an increase in diffuse reflectance after integrating the SiO_x structures, indicating enhanced light scattering and the potential for optical path length improvement. A study was performed to investigate the absorption losses throughout the decrease of the absorber layer thickness, showing a reduction in short-circuit current density with decreasing absorber thickness. The fabricated structures were integrated into ultrathin CIGS solar cells. Although an enhanced optical performance in the near-infrared region was demonstrated, the devices showed degradation of electrical performance. Scanning electron microscopy (SEM) analysis suggested that the nanostructures disrupted the CIGS growth morphology, contributing to increased electrical losses. For bifacial applications, dielectric-encapsulated Au nanopillar arrays were developed on ITO-coated soda-lime glass substrates. Different pillar architectures, dielectric materials, and contact opening geometries were fabricated and optimized. Morphological characterization by SEM and atomic force microscopy (AFM) confirmed the successful fabrication of the intended structures. Optical measurements showed increased diffuse transmittance and reflectance relative to flat ITO references, demonstrating the light scattering capabilities of the nanostructures. The integration of encapsulated Au nanopillars on flexible SS/TiW/MoNa/Mo substrates was explored. Although a complete process flow was not achieved, it was demonstrated that dielectric encapsulation effectively prevented Au diffusion into the absorber. Overall, the results demonstrate the potential of nanostructured rear interfaces for improving light management in ultrathin CIGS solar cells, while highlighting the challenges associated with preserving device electrical performance after integration. The developed process flows provide a foundation for the implementation of rear light management strategies in ultrathin solar cells.

Keywords: nanofabrication, light management, ultrathin absorber, CIGS solar cells

Table of Contents

List of Figures vi
List of Abbreviations ix

1. Introduction 1
2. Theoretical Background 3
   2.1. CIGS solar cells 3
      2.1.1. Bifacial CIGS 8
      2.1.2. Ultrathin Flexible CIGS 9
   2.2. Light Management 10
      2.2.1. Front Strategies 11
      2.2.2. Rear Strategies 13
      2.2.3. Spectral Conversion 17
   2.3. Nanofabrication 18
      2.3.1. Lithography 18
      2.3.2. Etching 19
3. Experimental Methods 21
   3.1. Development of ultrathin flexible CIGS solar cells with integrated SiO_x pillars 21
      3.1.1. Ultrathin flexible CIGS solar cells 21
      3.1.2. Development of SiO_x pillars on SS flexible substrates 23
   3.2. Development of Au pillars encapsulated by a dielectric on a bifacial substrate 25
      3.2.1. Overview of the Fabricated Series 25
      3.2.2. Fabrication Process Flow 26
   3.3. Characterization 28
4. Results and Discussion 31
   4.1. SiO_x Pillars on SS Flexible Substrates Process Flow Optimization 31
      4.1.1. RR removal 31
      4.1.2. SiO_x etch 31
      4.1.3. Final Resist Strip 37
      4.1.4. Optical Evaluation 39
   4.2. Ultrathin Flexible CIGS Solar Cells 40
      4.2.1. Figures of Merit 40
   4.3. Ultrathin Flexible CIGS solar cells with SiO_x pillars 42
      4.3.1. Figures of Merit 43
      4.3.2. SEM analysis 45

4.4. Encapsulated Au Pillars on ITO - Process Flow Optimization 45
4.4.1. Pillars RR strip 46
4.4.2. Au Etch.....46
4.4.3. Au Resist Strip 49
4.4.4. RR removal from Contact Openings Imprint.....49
4.4.5. Dielectric etch.....51
4.4.6. Exposed Au Wet Etch 51
4.4.7. Final Resist Strip.....52
4.5. Au Pillars on ITO Characterization 53
4.5.1. SEM Analysis 53
4.5.2. AFM Analysis 54
4.5.3. UV-Vis-NIR Spectrophotometry Analysis.....55
4.6. Encapsulated Au Pillars on SS Flexible Substrates Process Flow Development 58
5. Conclusion and Future Work.....61

Bibliography 63

List of Figures

2.1. **a)** Schematic representation of the studied CIGS solar cell; **b)** Representative cross-section SEM image of a CIGS solar cell. 3
2.2. Graphical comparison between the relative absorption of CIGS and Si for different thicknesses [39]. 5
2.3. Example of a usual bifacial CIGS solar cell strucutre, with a TCO as both the front and the back contact [60]. 8
2.4. Simulated CIGS absorbance of thin ($2000\,\mathrm{nm}$) and ultrathin ($500\,\mathrm{nm}$) solar cell devices [10]. 10
2.5. Schematic illustration of the main optical mechanisms in a CIGS solar cell: **a)** with, and **b)** without light-management approaches [64]. 11
2.6. **a)** Quantum efficiency measurements for the simulated CIGS cell with and without ARC, in comparison with experimental results from [67]; **b)** Comparison of V_{oc} and J_{sc} values for different MgF_2 thickness values. Both data taken from [66]. 12
2.7. Reflectance of different back contact materials (Mo, Ag, and Ag encapsulated by ITO) before and after annealing [69]. 13
2.8. Simulated CIGS absorbance for the devices with: a Mo rear contact in a $500\,\mathrm{nm}$ CIGS solar cell; perfect reflector in a $500\,\mathrm{nm}$ CIGS solar cell; and a Mo-based $2\,\mu\mathrm{m}$ CIGS solar cell [10]. 14
2.9. Schematic illustration of the effects resulting from plasmonic NPs interaction with light: **a)** near-field and **b)** far-field scattering [10]. 16
2.10. J_{sc} curves for a flat Mo back contact, a grid (structure A) or pillar (structure B) back mirrors made of Ag or Cu [79]. 16
2.11. Schematic representation of an anisotropic and an isotropic etch. 19

3.1. **a)** UNO diagram: 1) LL chamber; 2) Sputter Station; 3) Upper Electric Cabinets; 4) Lower Cabinets. **b)** Sputter station diagram: 1) Inner chamber; 2) Transfer chamber; 3) Pneumatic Cylinder Assy; 4) Cooling Hub. 21
3.2. Schematic overview of the process flow for the fabrication of SiO_x pillars on SS flexible substrates. 23
3.3. Schematic overview of the process flow for the fabrication of Au pillars encapsulated by a dielectric on a lines configuration, on an ITO rigid substrate process flow. 26

4.1. Representative cross-section SEM images of the imprinted pillars pattern on the resist layer on SiO_x-coated Si substrates: **a)** after imprint; **b)** after $7\,\mathrm{s}$ O_2 strip. 32
4.2. Representative cross-section SEM image of the pillars after the "APS SiO_2 Etch" etch tests: **a** Sample with an ITO-coated SLG substrate; **b)** 5x5 cm^2 SS sample; **c)** 15.6x15.6 cm^2 SS sample. 33
4.3. Representative top-view SEM images of the SiO_x etch tests using the "Slow SiO_x Etch" recipe. After: **a)** RR removal, **b)** $90\,\mathrm{s}$, **c)** $100\,\mathrm{s}$, and **d)** $120\,\mathrm{s}$ "Slow SiO_x Etch". 34
4.4. SEM-EDS analysis of the agglomerates formed between the pillars when using the "Slow SiO_2 Etch". 34
4.5. Representative cross-section SEM images of the SiO_x etch tests using the "Al_2O_3 Etch" recipe from the ICP module in the STPS system. The following etch times were tested: **a)** no etch, **b)** $60\,\mathrm{s}$, **c)** $90\,\mathrm{s}$, **d)** $120\,\mathrm{s}$. 35
4.6. Representative cross-section SEM images of the SiO_x etch tests using the "SiO_x Etch" recipe. After: **a)** RR removal, **b)** $30\,\mathrm{s}$, **c)** $45\,\mathrm{s}$, and **d)** $60\,\mathrm{s}$ "SiO_x Etch". 36
4.7. Representative top-view SEM images of the "SiO_x Etch" etch. After: **a)** $45\,\mathrm{s}$, **b)** $60\,\mathrm{s}$. ..36

4.8. Representative cross-section SEM images of the resist strip tests. The following sequences were tested: **a)** MP plasma ashing; **b)** MP and HP plasma ashing; **c)** MP and HP plasma ashing and $2\,\mathrm{min}$ O_2 strip; **d)** MP and HP plasma ashing, $2\,\mathrm{min}$ O_2 strip and $30\,\mathrm{min}$ of MS3200 at $80\,^{\circ}\mathrm{C}$. 37
4.9. Representative cross-section SEM images of the resist strip tests matrix. The following tests were performed: **a)** MS3200 without ultrasounds; **b)** MS3200 with ultrasounds; **c)** MP plasma ashing and $30\,\mathrm{min}$ MS3200 without ultrasounds; **d)** MP plasma ashing and $30\,\mathrm{min}$ MS3200 with ultrasounds. 38
4.10. Representative cross-section SEM images of the resist strip reproducibility tests. The following tests were performed: **a)** plasma ashing and $30\,\mathrm{min}$ of MS3200 with ultrasounds; **b)** plasma ashing and $5\,\mathrm{min}$ O_2 strip. 39
4.11. Optical performance comparison between SiO_x pillars on Mo and a flat Mo back contact, regarding the following components: **a)** Relative total reflectance; **b)** Relative diffuse reflectance. 40
4.12. **a)** J_{sc} comparison between different thicknesses on both runs; **b)** V_{oc} comparison between different thicknesses on both runs. 41
4.13. **a)** FF comparison between different thicknesses on both runs; **b)** η comparison between different thicknesses on both runs. 41
4.14. EQE measurements of the same contact in every cell. 42
4.15. Comparison of the figures of merit between the $45\,\mathrm{s}$ etch of SiO_x, $60\,\mathrm{s}$ etch of SiO_x and reference sample: **a)** J_{sc}; **b)** V_{oc}; **c)** FF; **d)** η. 44
4.16. EQE measurements of the ultrathin CIGS solar cell with SiO_x pillars. 44
4.17. Representative SEM images of the ultrathin solar cells with integrated SiO_x pillars: **a)** Cross-section **b)**: Top-View. 45
4.18. Representative cross-section SEM images of the RR removal tests. **a)** R150 after imprint; **b)** R100 after imprint; **c)** R150 after 6 s O_2 strip; **c)** R100 after $12\,\mathrm{s}$ O_2 strip. ...46
4.19. Representative cross-section SEM images of Au pillars on ITO after a 110° IBE process for architectures: **a)** R150; **b)** R100. 47
4.20. Representative cross-section SEM images of Au pillars in ITO after the 110° (540 s) IBE, followed by: **a)** 130° (120 s) followed by 165° (900 s), R150 architecture; **b)** 165° (240 s), R100 architecture. 49
4.21. Representative cross-section SEM images of the resist strip tests after the Au etch. The following processes were tested: **a)** MS3200 at $80\,^{\circ}\mathrm{C}$ with ultrasounds with a magnification of 50800x and **b)** 8467x; **c)** 3 cycles of LP plasma ashing; **d)** 3 cycles of HP plasma ashing + $2\,\mathrm{min}$ of O_2 strip. 50
4.22. Representative cross-section SEM images of the SiO_x lines sample: **a)** After imprint; **b)** After $12\,\mathrm{s}$ O_2 strip. 50
4.23. Representative cross-section SEM images of encapsulated Au pillars after SiO_x etch by: **a)** IBE; **b)** RIE. 51
4.24. Representative cross-section SEM images of the encapsulated Au pillars: **a)** Before immersion in Technietch ACI2; **b)** After immersion in Technietch ACI2. 52
4.25. Representative cross-section SEM images of the encapsulated Au pillars: **a)** Before 3 cycles of LP plasma ashing; **b)** After 3 cycles of LP plasma ashing. 53
4.26. Representative top-view SEM images of Al_2O_3 passivated samples from the series A, with **a)** and **b** lines passivation scheme, **c)** and **d)** holes passivation scheme. The measurements are represented by yellow lines. 54
4.27. AFM analysis of a SiO_x encapsulated sample from series B with the lines scheme: **a)** Line scan, **b)** 3D profile. 55
4.28. Comparison between series A and B regarding the following components: **a)** Relative total transmittance, and **b)** Relative total reflectance. 56

4.29. **a)** Relative diffuse transmittance spectra from the A series samples, and **b)** Relative diffuse reflectance spectra from the A series samples. 56
4.30. **a)** Relative diffuse transmittance spectra from the B series samples, and **b)** Relative diffuse reflectance spectra from the B series samples. 57
4.31. **a)** Relative diffuse transmittance spectra from the C series samples, and **b)** Relative diffuse reflectance spectra from the C series samples. 58
4.32. Cross-sectional TEM images of the studied cells: **a)** reference; **b)** Au pillars cell. 59

List of Abbreviations

AFM	Atomic Force Microscopy
ALD	Atomic Layer Deposition
APS	Advanced Plasma System
ARC	Anti-Reflective Coating
ASL	Anti-Sticking Layer
BIPV	Building-Integrated Photovoltaic
c-Si	Crystalline Silicon
DC	Direct Current
DCo	Down-Conversion
DI	Deionized
DS	Down-Shifting
DWL	Direct Write Lithography
EBL	E-Beam Lithography
EDS	Energy-dispersive X-ray Spectroscopy
EQE	External Quantum Efficiency
FF	Fill Factor
FIB	Focused Ion Beam
FTDT	Finite-Difference Time-Domain
FTO	Fluorine-doped Tin Oxide
GGI	Gallium to Group III
HP	High Power
IBE	Ion Beam Etching
ICP	Inductively Coupled Plasma
ICP-RIE	Inductively Coupled Plasma-Reactive Ion Etching
IPA	Isopropanol
IPS	Intermediate Polymer Stamp
ITO	Indium Tin Oxide
JV	Current Density-Voltage
LL	Loadlock
LP	Low Power

LSPR	Localized Surface Plasmon Resonance
MP	Medium Power
NIL	Nanoimprint Lithography
NIR	Near-Infrared
P	Power
PECVD	Plasma Enhanced Chemical Vapor Deposition
PL	Photolithography
PV	Photovoltaic
PVD	Physical Vapor Deposition
RF	Radio Frequency
RIE	Reactive Ion Etching
RR	Residual Resist
RT	Room Temperature
SEM	Scanning Electron Microscopy
SIMS	Secondary Ion Mass Spectroscopy
SLG	Soda-Lime Glass
SQ	Schockley-Queisser
SS	Stainless Steel
T	Temperature
TCO	Transparent Conductive Oxide
TEM	Transmission Electron Microscopy
UC	Up-Conversion
UV	Ultraviolet

1. Introduction

The increasing global demand for energy, combined with the environmental impact associated with fossil fuel consumption, has intensified the search for sustainable and renewable energy sources [1]. At the same time, concerns regarding greenhouse gas emissions and climate change have accelerated the transition towards low-carbon energy technologies. In this context, renewable energy systems have become essential to ensure long-term energy sustainability and reduce dependence on non-renewable resources. Among the different renewable energy technologies currently available, solar photovoltaic (PV) energy has emerged as one of the most rapidly growing solutions in the market, doubling production and installation every 3 years on average. [2] Over the last decades, PV technologies have experienced progress in terms of both efficiency and cost reduction, enabling their large-scale implementation worldwide. Silicon-based PV modules currently dominate the market, mainly due to high efficiency values and an established industrial infrastructure [3]. Nonetheless, conventional silicon (Si) solar cells still present several limitations that restrict their use in certain scenarios.

As urban areas continue to expand, the integration of PV systems directly into buildings has gained significant interest as a strategy to maximize energy generation without requiring additional land occupation [4, 5]. This concept, commonly referred to as Building-Integrated PV (BIPV), aims to incorporate solar cells directly into architectural elements such as facades, roofs, and windows. In contrast to traditional PV installations, BIPV systems are expected not only to generate electricity efficiently but also to fulfill structural and aesthetic functions within the building. The development of BIPV technologies introduces additional requirements beyond high efficiency values, including reduced weight, flexibility, aesthetic versatility, and compatibility with large-area fabrication [5, 6]. Consequently, researched has been directed towards alternative thin-film PV technologies, capable of delivering these requirements.

Among the various thin-film PV materials investigated, $Cu(In,Ga)(S,Se)_2$ (CIGS) solar cells have attracted attention due to their excellent optoeletronic properties and high absorption coefficient [7]. Unlike crystalline Si (c-Si), which requires absorber thicknesses on the order of hundreds of micrometers, CIGS is capable of absorbing most of the solar spectrum's photons within only a few micrometers [8]. This characteristic makes CIGS particularly attractive for lightweight and flexible PV applications, such as BIPV.

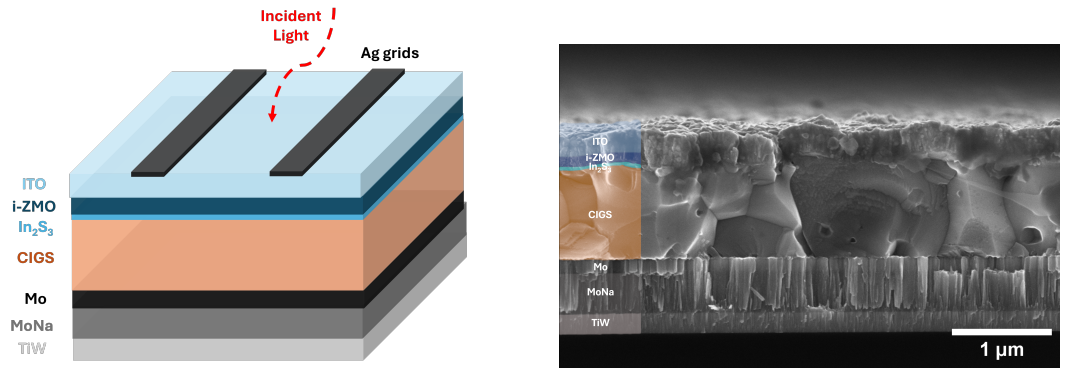
Driven by the need to reduce material consumption, lower fabrication costs, enable highly flexible devices and innovative applications, recent research has increasingly focused on ultrathin CIGS absorbers, i.e. submicrometer absorber layer [9]. However, decreasing the absorber thickness introduces majors challenges, being the main one the reduced optical path length which limits photon absorption, especially at longer wavelength values, resulting in lower photocurrent and reduced device efficiency.

To overcome this limitation, light-management strategies have emerged as a key approach for ultrathin CIGS solar cells. By employing nanostructured surfaces, textured interfaces, dielectric scattering layers, or plasmonic nanostructures, it is possible to enhance light trapping and increase the effective optical path length within the absorber without increasing its physical thickness [10]. Such approaches aim to compensate for the absorption losses associated with ultrathin absorbers and improve the overall performance of the device. Nevertheless, the optical gains that these nanostructures can allow for are highly sensitive to their geometry, dimensions, periodicity, and surface quality, requiring nanofabrication procedures capable of producing nanoscale features with high accuracy and reproducibility. Consequently, the development of robust nanofabrication process flows has become a critical challenge in translating light-management concepts into high-performance PV devices. Thus, in this thesis novel nanofabrication process flows are explored to produce periodic dielectric and metallic nanostructures, with the aim of increasing the optical path length in ultrathin CIGS solar cells.

2. Theoretical Background

2.1. CIGS solar cells

CIGS solar cells is a complex system composed by many layers, each with its specific funtion. These layers include the substrate, the back contact, the absorber layer (p-type), the buffer layer (n-type), and the transparent conductive oxide (TCO). A schematic representation of the studied CIGS solar cell and a representative cross-section scanning electron microscopy (SEM) image can be seen in Fig. 2.1a), and b), respectively.



(A) (B)

FIGURE 2.1: **a)** Schematic representation of the studied CIGS solar cell; **b)** Representative cross-section SEM image of a CIGS solar cell.

The substrate should ensure vacuum compatibility, thermal stability, suitable thermal expansion, chemical inertness and surface smoothness. These aspects are important to ensure since the deposition is easier on smooth substrates and the cell will undergo vacuum depositions at high temperatures (specially during the absorber layer deposition) [11]. Many materials have been used and researched, but soda-lime glass (SLG) is one of the most commonly used as it is thermally stable, chemically inert, has a similar thermal expansion coefficient as the absorber, and presents a smooth surface [12]. For lightweight and flexible substrates, metallic foils (stainless steel (SS), titanium) and polyimide films are the most used [13]. One of the most interesting features of SLG is that it is able to release sodium (Na) into the absorber layer, which allows for an increased free carrier density by at least one order of magnitude [14]. Na improves the cell efficiency, but controlling the amount of Na that diffuses into the absorber layer during CIGS growth is still a challenge. This aspect relies on both the uniformity of Na on the substrate, as well as the ability of the back contact (usually molybdenum, Mo) to uniformly enable Na diffusion into the absorber layer [15]. One of the researched ways to counter this problem is to add a

diffusion barrier, blocking Na diffusion into CIGS and adding it directly using an external source [16, 17]. It is possible to control the Na doping by depositing a thin-film of sodium fluoride (NaF) prior to the absorber deposition or adding a MoNa layer as the bottom layer of the rear contact [18].

The rear contact layer acts as both an electrical contact and an optical reflector, directing light back into the absorber layer [19]. This layer mainly serves the purpose of extracting generated holes from the device and delivering them to an external circuit for utilization [20]. Similarly to the substrate, the back contact provides stability and mechanical support for the cell. In chalcogenides-based solar cells, a Mo bilayer deposited by sputtering, is usually used as back contact. The Mo film is simultaneously characterised by high conductivity and strong adhesion. The bottom layer (sputtered with high pressure) is designed to have good adhesive properties, while the top layer (sputtered with low pressure) is designed to be low ohmic and conduct the current, providing an electrode with good adhesion and good electrical conductivity [21]. It also does not degrade during the deposition of the absorber layer at high substrate temperature, and does not react strongly with the absorber [22, 23]. During CIGS deposition, selenium (Se) will also react with Mo and form molybdenum diselenide ($MoSe_2$) [22]. This new interfacial layer is beneficial since it allows for a quasi-ohmic contact [24]. The growth of the $MoSe_2$ layer can be promoted by tailoring the properties of the Mo film [22]. Furthermore, it can enhance the overall performance of the solar cell by improving charge collection and reducing recombination losses [25]. Many deposition techniques are used for this layer, including Ion-beam sputtering, Direct Current (DC) sputtering, and Radio Frequency (RF) sputtering, with the latter two being the most commonly used [22, 26, 27]. DC sputtered films possess good uniformity, good adhesion properties over large surface areas and a higher deposition rate than RF sputtering [24]. Nevertheless, RF sputtered films are more conductive and display improvements in open circuit voltage (V_{oc}) and short circuit current-density (J_{sc}) [22].

The most important layer of a CIGS solar cell is the one that follows, the absorber layer. The function of this layer is to generate and absorb electron-hole pairs from sunlight's incoming photons and its properties, such as thickness and bandgap, play a significant role in enhancing the overall performance of the cell [28]. CIGS solar cells are widely used due to their efficiency, low-cost, easy integration and tunable optical bandgap (1.0-$1.7\,\text{eV}$) [29, 30]. The latter can be tuned by varying the Ga/In ratio which can improve the V_{oc} [31]. The bandgap energy is increased by raising the Ga concentration [30]. In 2024, a record efficiency of 23.64% was obtained by introducing silver (Ag) in the absorber

([Ag]/([Ag]+[Cu])=0.19) [32]. CIGS has also received attention due to its direct bandgap [31]. This is a big advantage over c-Si since PV materials with direct bandgap transitions absorb light more effectively than those with indirect bandgaps, allowing for thinner devices [33]. Hence, CIGS presents an higher absorption coefficient than c-Si, which allows to decrease the usage of raw materials, making them less expensive [7, 34]. For example, for a photon of $1.5\,\mathrm{eV}$ ($827\,\mathrm{nm}$), the c-Si absorption coefficient is $10^3\ \mathrm{cm}^{-2}$, while that of CIGS is around $10^5\ \mathrm{cm}^{-2}$ [35, 36]. A comparison between the absorption coefficient values of CIGS and c-Si for different thicknesses can be observed in Fig. 2.2. Moreover, with a thickness of around $1\,\mu\mathrm{m}$, CIGS cells can absorb most parts of the photons in the interest spectral region [31]. Compared to c-Si, CIGS solar cells are not as widely commercialized since it is difficult to find high quality and large-scale CIGS based solar cells [29]. Indium (In) is not as common as Si, with its concentration in the earth's crust being comparable to Ag (0.1 part per million) [37, 38].

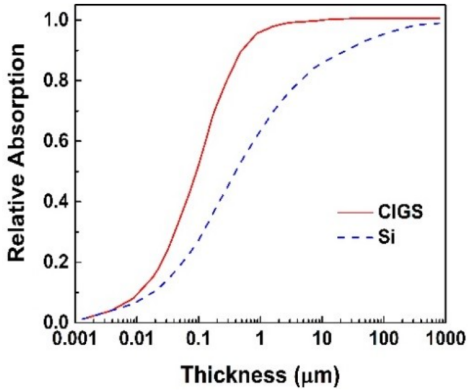


FIGURE 2.2: Graphical comparison between the relative absorption of CIGS and Si for different thicknesses [39].

CIGS deposition occurs by mainly 2 techniques, thermal co-evaporation and two stage chalcogenization [40]. The first is a physical vapor deposition (PVD) technique where copper (Cu), In, Ga and Se are simultaneously evaporated in a vacuum environment. Each element is heated in a separate source and the temperature ranges from 400 to $600\,^{\circ}\mathrm{C}$ [40]. This technique allows for a large grain size, high efficiency values and to create CIGS films with different compositions and gradients [41]. Two stage chalcogenization refers to a method where the absorber layer is created in two separate steps, the precursor deposition and the chalcogenization [42]. On the first step, Cu, Ga and In are deposited onto the cold substrate by sputtering or evaporation. Subsequently, the chalcogenization takes place, where the CIG is exposed to the chalcogen (Se, S) atmosphere at elevated

temperatures. The latter method promises potential for high throughput and an improved composition control [43].

To complete the pn-juntion, a buffer layer is deposited on top of the absorber. Its primary functions are to improve cell performance by reducing recombination losses at the absorber interface, facilitating charge carrier movement, optimizing the band alignment of the device and transmit the maximum amount of light possible into the absorber so that electron-hole pair generation occurs as efficiently as possible [44]. For that reason, it is believed that the bandgap of the buffer should be wider and have low electron affinity in comparison to CIGS [45]. This layer also protects the absorber layer from corrosion during the window layer deposition. The thickness of the buffer layer must be carefully optimized, as excessively thick layers increase parasitic optical absorption and carrier recombination, whereas excessively thin layers may fail to fully passivate interface defects and form a uniform junction with the absorber layer. Usual values of thickness are 50 to $200\,\mathrm{nm}$ [44]. Cadmium Sulfide (CdS) has been the conventional buffer layer since it satisfies most of the requirements, being usually deposited via chemical bath deposition [46, 47]. However, research is actively exploring alternatives due to CdS's limitations [48]. This material presents high lattice mismatch and optical absorption losses, specially in the short wavelength range [44]. This latter problem arises from the fact that the bandgap of CdS is $2.4\,\mathrm{eV}$, resulting in photons being unintentionally absorbed in this layer at higher photon energy [49]. In addition, cadmium is a toxic element in the environment, which may endanger human health [30]. For that reason, many other alternatives for this layer, such as indium sulfide (In_2S_3), zinc sulfide (ZnS), zinc selenide (ZnSe), tin sulfide (SnS), zinc oxide (ZnO), and tin oxide (SnO_2), are being researched [30, 44, 46, 48, 50, 51].

The last layer to be deposited in a CIGS cell is the front contact, also known as optical window or TCO layer. This must be a transparent layer since it needs to allow sunlight to penetrate while minimizing reflection, absorption and electrical resistance [20]. In order to maximize light transmission and minimize optical losses, the thickness and conductivity of the front contact must be optimized [52]. This layer is usually divided into two materials, intrinsic zinc oxide (ZnO, with a thickness of around $50\,\mathrm{nm}$) and aluminum-doped zinc oxide (Al:ZnO, also referred to as AZO, with a thickness of around $200\,\mathrm{nm}$), both deposited by sputtering [17]. The first is used to limit electronic losses, while the latter is the TCO component, used to collect the carriers. Moreover, indium tin-oxide (ITO) is also usually used as a TCO in CIGS solar cells, as it offers good transparency, does not degrade in exposure to sunlight or temperature fluctuations, and provides ample conductivity [20].

There are four important parameters in solar cells metrics: I_{sc}, the current delivered by the device under short circuit (V = $0\,\mathrm{V}$); V_{oc}, voltage under open circuit (I = $0\,\mathrm{A}$); fill factor (FF), ratio between the maximum power P_{max} and the product $V_{oc} \cdot I_{sc}$; and power conversion efficiency (η) of the cell, ratio of the electrical power output over the total incoming sunlight power P_{sun} [53]. The latter parameter can be calculated as defined in Eq. 2.1. It is important to note that often results are shown as J_{sc}, the current per unit area that flows through a solar cell when it is short-circuited.

$$\eta = \frac{J_{sc} \cdot V_{oc} \cdot FF}{P_{sun}} \tag{2.1}$$

Under the Shockley–Queisser (SQ) model, the limit for the maximum efficiency of a single-junction solar cell is around 33.16% at a bandgap energy of $1.34\,\mathrm{eV}$ ($928\,\mathrm{nm}$) and 32.85% at a bandgap energy of $1.15\,\mathrm{eV}$ ($1080\,\mathrm{nm}$) [54].

Despite substantial research and performance improvements, CIGS solar cells have struggled to displace c-Si as the dominant PV technology. Si PV has benefited from decades of optimization in wafer production, cell processing and module integration, which have driven costs downwards and production efficiency values above 20% in commercial products. As of 2024, Si solar cells dominate around 98% of the PV production market, while CIGS only represent around 1% [55]. CIGS thin-film solar panels also cost about $0.60 for each watt, while c-Si panels cost around $0.24 [56].

Nonetheless, CIGS retains distinct properties that make it promising for niche PV applications where the limitations of c-Si become more evident. One such emerging application is bifacial CIGS solar cells, which are designed to absorb light from both the front and rear surfaces, enabling energy capture from reflected and diffuse irradiance in addition to direct sunlight [57]. This type of cells has great potential to be applied, for example, in BIPV, agrivoltaics, and other types of transparent applications, as well as tandem solar cells [58, 59]. This need also motivated ultrathin flexible CIGS solar cells. These cells consist of a solar cell where the CIGS layer is thinner than $900\,\mathrm{nm}$, promising to increase fabrication throughput and decrease manufacturing costs by reducing the usage of critical raw materials [9].

2.1.1 Bifacial CIGS

Bifacial solar cells are designed to absorb sunlight from both their front and rear faces, enabling them to harvest not only direct solar irradiance, but also albedo from the environment, with an example of a usual bifacial CIGS solar cell structure represented in Fig. 2.3. This dual-sided illumination concept has been extensively exploited in c-Si PV to increase energy yield per unit area, particularly in installations with high ground albedo such as snowy or desert environments [59]. Due to this enhancement in energy output on outdoor circumstances, bifacial CIGS solar cells have reached efficiencies over 20% on rigid glass substrates and over 16% on flexible ones [57].

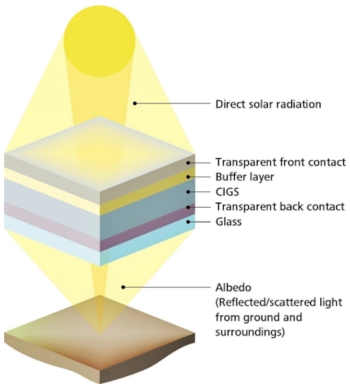


FIGURE 2.3: Example of a usual bifacial CIGS solar cell strucutre, with a TCO as both the front and the back contact [60].

Unlike traditional monofacial CIGS cells, which use an opaque back contact to reflect unabsorbed light back into the absorber and collect carriers, bifacial designs require the rear contact to be transparent and conducting to allow light to enter from the backside. This is typically achieved by replacing the opaque back contact of Mo with a TCO, such as ITO or fluorine-doped tin oxide (FTO), which serves both as an electrical contact and an optical window [59]. However, one of the main challenges in bifacial CIGS cells arises from interface reactions at elevated deposition temperatures. Conventional high-temperature CIGS growth (>550 °C) can lead to the formation of gallium oxide (GaO) at the interface between the absorber and the TCO rear contact, which impedes carrier transport, increases the resistivity and reduces performance under both rear and front illumination. Some works have addressed this issue using modified low-temperature deposition processes that reduce such oxide formation, resulting in improved interface quality and lower recombination losses at the rear interface [57, 61].

2.1.2 Ultrathin Flexible CIGS

Another of the most promising directions for CIGS PV is the development of ultrathin and flexible solar cells. Conventional CIGS solar cells typically have absorber layers with thicknesses between 1.5 and $2\,\mu\mathrm{m}$ in order to ensure efficient absorption of the solar spectrum, and minimize recombination losses at the rear interface. In contrast, ultrathin CIGS devices reduce the absorber thickness below $900\,\mathrm{nm}$, while still maintaining reasonable performance [9]. Reducing the absorber thickness offers several advantages. First, it significantly reduces the consumption of critical raw materials, particularly In and Ga, which are relatively scarce and contribute to the overall cost of CIGS module production. Lower material usage also enables higher manufacturing throughput by reducing deposition time during absorber growth. Additionally, ultrathin absorbers allow the fabrication of lightweight and mechanically flexible PV devices when deposited on alternative substrates such as polyimide, metal foils, or ultrathin glass. Flexible CIGS solar cells fabricated on such substrates have already demonstrated efficiency values approaching those of rigid devices, with reports of flexible CIGS cells reaching efficiency values above 22%, compared to record values of about 23% for devices fabricated on rigid SLG substrates [9].

Despite these advantages, reducing the absorber thickness introduces several important challenges. As the absorber becomes thinner, incomplete optical absorption becomes a major loss mechanism, particularly in the near-infrared (NIR) region of the solar spectrum where the absorption coefficient of CIGS decreases. Such losses can be observed in Fig. 2.4, where Oliveira et al. simulated the CIGS absorbance of thin ($2000\,\mathrm{nm}$) and ultrathin ($500\,\mathrm{nm}$) solar cell devices [10]. This reduction in absorption leads to a decrease in J_{sc} values if no additional optical management strategies are implemented. Furthermore, ultrathin devices become more sensitive to recombination losses at the rear interface, since photogenerated carriers are produced closer to the back contact, an interface with a high density of defects. These reasons explain why the world-record efficiency for a $500\,\mathrm{nm}$ CIGS solar cell still stands at 15.2% [62]. To mitigate recombination effects, researchers have explored the incorporation of rear surface passivation layers and patterned dielectric structures between the absorber and the back electrode. These layers reduce recombination while maintaining electrical contact through localized openings, thereby improving the overall carrier collection of the ultrathin cell [9]. Nevertheless, there's still the incomplete absorption challenge to be overcome.

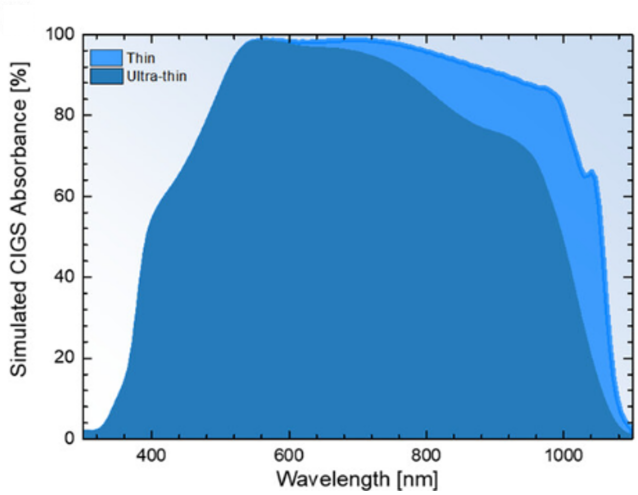
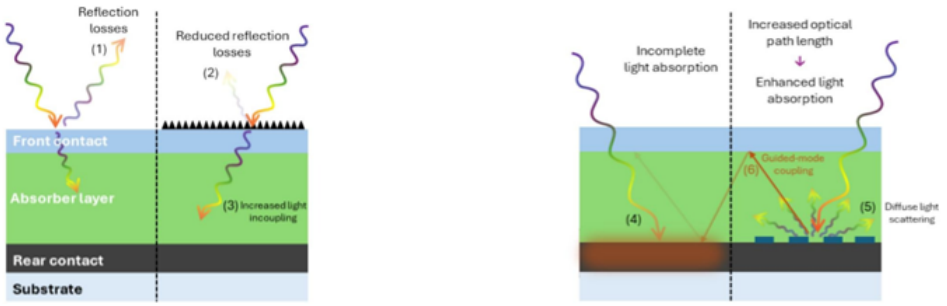


FIGURE 2.4: Simulated CIGS absorbance of thin ($2000\,\mathrm{nm}$) and ultrathin ($500\,\mathrm{nm}$) solar cell devices [10].

2.2. Light Management

Ideally, all incident photons with energy higher than the bandgap should be absorbed in the CIGS layer, producing and maximizing the photocurrent in the cell [63]. However, optical losses prevent efficient light absorption. This phenomenon has a negative impact on the solar cell power output and, therefore, efficiency. In substrate-based CIGS solar cells, optical losses can be broadly classified as front-side reflection losses and rear-side absorption losses, occurring before and after light interaction with the absorber, respectively, being these phenomena depicted in Fig. 2.5a) and b), respectively. Front-side losses originate from the refractive index (n) mismatch between air and the transparent front contact and can be minimized using anti-reflective texturing that allow for grade index structures that improve light incoupling [10]. Rear-side losses arise from the incomplete absorption of long wavelength photons, which reach the back contact before being absorbed. Introducing periodic nanostructures at the rear interface enhances scattering, diffraction, and guided-mode coupling, increasing the effective optical path length within the absorber and thereby improving light absorption, particularly in ultrathin CIGS solar cells.



(A) (B)

FIGURE 2.5: Schematic illustration of the main optical mechanisms in a CIGS solar cell: **a)** with, and **b)** without light-management approaches [64].

2.2.1 Front Strategies

Front contact reflection is a significant optical loss mechanism, as well as the reflection in each of the following layers until reaching the absorber. In 2014, Kosyachenko et al. evaluated optical and recombination losses in thin-film solar cells based on CIGS. These results, displayed in Table 2.1, showed that reflection and parasitic absorption losses amount to 17–18% of total efficiency, from which 8% is just due to the reflection at each interface before reaching the absorber.

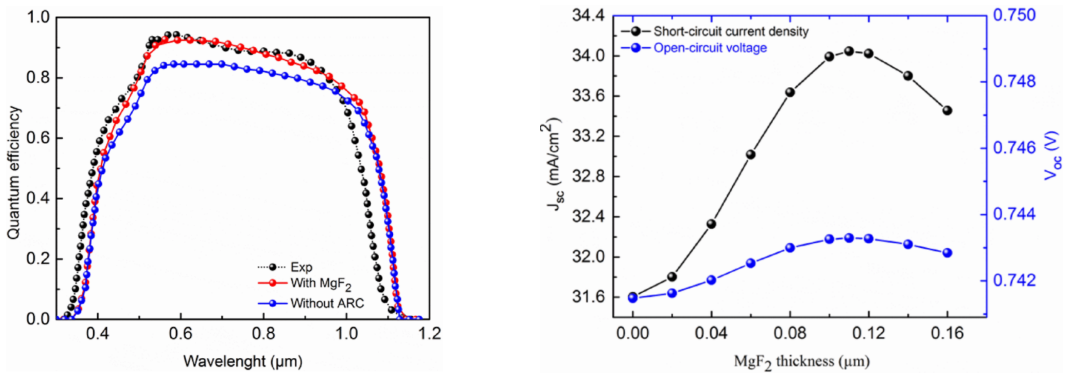
TABLE 2.1: Optical loss contributions in the different top interfaces and layers of two different CIGS cells [65].

	$CuIn_{0.69}Ga_{0.31}Se_2$	$CuIn_{0.34}Ga_{0.66}Se_2$
Reflection losses		
Air/ZnO interface	1.9% (0.8 mA/cm^2)	1.4% (0.5 mA/cm^2)
ZnO/CdS interface	0.9% (0.4 mA/cm^2)	1.0% (0.3 mA/cm^2)
CdS/CIGS interface	1.3% (0.5 mA/cm^2)	1.1% (0.4 mA/cm^2)
Shading from grid	4.0% (1.7 mA/cm^2)	4.0% (1.3 mA/cm^2)
Total reflection losses	**8.1% (3.4 mA/cm^2)**	**7.5% (2.5 mA/cm^2)**
Parasitic Absorption losses		
Absorption in ZnO	2.9% (1.2 mA/cm^2)	1.9% (0.6 mA/cm^2)
Absorption in CdS	6.3% (2.6 mA/cm^2)	7.9% (2.6 mA/cm^2)
Insufficient absorptivity	0.2% (0.1 mA/cm^2)	0.4% (0.1 mA/cm^2)
Total absorption losses	**9.4% (3.9 mA/cm^2)**	**10.2% (3.4 mA/cm^2)**
Total optical losses	**17.5% (7.3 mA/cm^2)**	**17.7% (5.8 mA/cm^2)**

One common light-management strategy is to add an anti-reflective coating (ARC) on the window layer. The reduction of reflection using an ARC is based on the principle of thin-film interference. When light is incident on the ARC layer, part of the wave is reflected at the air/ARC interface, while another portion propagates through the coating and is reflected at the ARC/window layer interface. These two reflected waves can interfere

either constructively or destructively, depending on their relative phase difference. By carefully selecting the n and thickness of the ARC, it is possible to achieve destructive interference between the reflected waves, effectively cancelling them and minimizing the overall reflected intensity [65]. Magnesium fluoride (MgF_2) is a typical material used to coat ZnO since it has a n_{arc} close to the theoretically ideal $(n_2)^{\frac{1}{2}}$, where n_2 is the n of ZnO [65]. Another important aspect of this material is that it is a transparent dielectric layer, which avoids the introduction of parasitic absorption losses [63]. This directly enhances J_{sc} and the efficiency of the solar cell.

In 2020, Khadir et al. carried out a numerical investigation of ARC effect on the performance of a CIGS solar cell using the Atlas module from SILVACO Technology Computer-Aided Design (T-CAD) [66]. This work studied the effect of an ARC on V_{oc}, J_{sc} and η for different thicknesses of ARC and main layers, and compared these results with experimental results from Nishinaga et. al. [67]. The simulations showed that, when using a $0.11\,\mu m$ MgF_2 monolayer, efficiency increased from 18.99 to 20.52% (an improvement of 8.10%). In Fig. 2.6 it is possible to observe the results from the mentioned work. Fig. 2.6a) clearly shows the improvement achieved by the ARC layer in the quantum efficiency spectra in the 400-$1000\,nm$ range, while Fig. 2.6b) confirms that the ideal thickness for the MgF_2 monolayer was of $0.11\,\mu m$.



(A) (B)

FIGURE 2.6: **a)** Quantum efficiency measurements for the simulated CIGS cell with and without ARC, in comparison with experimental results from [67]; **b)** Comparison of V_{oc} and J_{sc} values for different MgF_2 thickness values. Both data taken from [66].

Besides ARC, front surface texturization is another widely used strategy to improve light coupling into solar cells [10]. By introducing micro or nanoscale structures at the front interface, the transition between air and the solar cell surface becomes more gradual. This creates an effective n grading, where the n progressively increases from that of air to that of the device materials. Additionally, front texturization can modify the propagation

direction of the incoming light, instead of travelling normally through the device, photons may enter at oblique angles, increasing their optical path length inside the device. This effect increases the probability of photon absorption, which can increase parasitic losses in the top layers, or the absorption by the CIGS solar cell. Therefore, front texturing can simultaneously act as an antireflection mechanism and as a light-trapping strategy, improving overall optical performance.

2.2.2 Rear Strategies

One of the big drawbacks of Mo is its low reflectivity ($<$30% in air), preventing light to be redirected effectively back to the absorber layer [10, 68]. Substitution of the back contact material has been studied by many groups [69–72]. For example, Ag, Au, Cu and Al are materials with suitable optical properties for a rear contact. Nonetheless, these elements possess high diffusivity and react with the CIGS layer. One strategy explored to counter this problem is to encapsulate the metallic mirror in ITO. This way, the mirror would reflect the photons on the rear end without diffusing into the CIGS layer. For example, in a 2019 study, Gouillart et al. successfully improved J_{sc} by $4.6\,\mathrm{mA\,cm^{-2}}$ employing this method [69]. As displayed in Fig. 2.7, the reflectance of the back contact is highly improved by the Ag mirror ($150\,\mathrm{nm}$-thick). Even when coupled with an ITO layer, the reflectance improves for both 30 and $200\,\mathrm{nm}$ ITO thickness values. The ITO implementation may be problematic for Na diffusion, but this may be bypassed by performing alkali pre and post-deposition treatments [73].

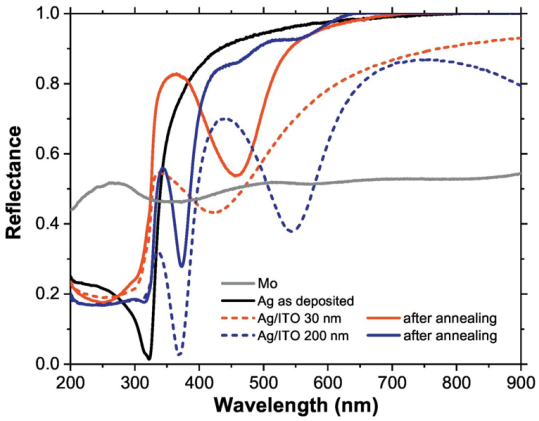


FIGURE 2.7: Reflectance of different back contact materials (Mo, Ag, and Ag encapsulated by ITO) before and after annealing [69].

In 2022, Oliveira et al. performed optical simulations in three CIGS device architectures: (1) $500\,\mathrm{nm}$ CIGS with a typical Mo rear contact; (2) $500\,\mathrm{nm}$ CIGS with a perfect reflective interface; and (3) $2\,\mu\mathrm{m}$ absorber with a typical Mo rear contact. The objective of this work

was to quantify the possible increase in J_{sc} values using a perfect reflector as the rear contact [10]. These simulations were performed using the *Ansys Lumerical finite-difference time-domain* (FDTD) software, and the results are displayed in Fig. 2.8. An improvement of $1.8\,\mathrm{mA\,cm^{-2}}$ over the Mo back contact was observed for the perfect reflector. It is possible to notice that this enhancement comes mostly from the improved absorbance in the NIR. However, it is important to note that there is still a gap of $2.1\,\mathrm{mA\,cm^{-2}}$ between the perfect reflector in a $500\,\mathrm{nm}$ CIGS solar cell and the $2\,\mu\mathrm{m}$ absorber, since a perfect metallic mirror would only double the optical path length.

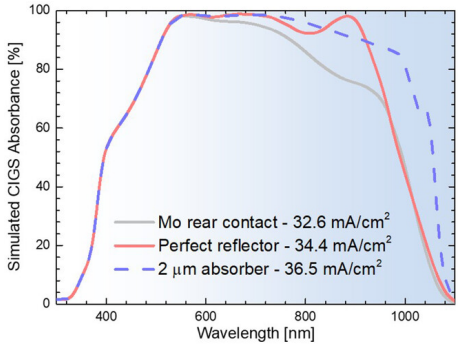


FIGURE 2.8: Simulated CIGS absorbance for the devices with: a Mo rear contact in a $500\,\mathrm{nm}$ CIGS solar cell; perfect reflector in a $500\,\mathrm{nm}$ CIGS solar cell; and a Mo-based $2\,\mu\mathrm{m}$ CIGS solar cell [10].

Random surface texturization has long been employed as an alternative strategy to enhance light trapping beyond the limitations of a planar reflective interface [74]. In this approach, the rear contact is intentionally roughened, creating randomly distributed surface features capable of scattering incident light into different directions. This effect can significantly increase the effective optical path length through multiple internal reflections and, under ideal Lambertian scattering conditions, the optical path length enhancement can theoretically approach a factor of $4n^2$ [75]. The factor $4n^2$ (often called the Yablonovitch limit) is the maximum theoretical light-trapping enhancement that can be achieved in a solar cell using random Lambertian texturing [76]. However, to reach this limit, the features size must be hundreds of nanometers to several micrometers, comparable to the wavelength of the incident radiation [10]. This requirement becomes problematic in ultrathin CIGS solar cells since the dimensions of the textured structures become comparable to the absorber thickness itself. In this scenario, large features disrupt the growth of CIGS and subsequent layers, leading to increased surface roughness, and structural defects that degrade electrical performance [10].

Rather than random texturization, periodically nanostructured materials can alternatively

be implemented on the rear contact. These enable additional optical mechanisms that further enhance the optical path length while having smaller feature sizes [10]. In metallic nanostructures, such as Au or Ag, the dominant mechanism is the excitation of localized surface plasmon resonances (LSPR). These resonances arise from the coherent oscillation of free electrons driven by the external electromagnetic field, and depend on the size, shape, and composition of the nanostructure [10]. Upon illumination, the incident electromagnetic field interacts with the free electrons, inducing their displacement relative to the positively charged lattice [77]. As electrons accumulate on one side of the nanoparticle, a restoring Coulomb force is established due to charge separation, resulting in the formation of an electric dipole. This interaction between the external driving field and the restoring force leads to a collective oscillatory motion of the electron cloud, analogous to a driven harmonic oscillator [10]. This phenomenon is referred to as LSP. The resonance condition is achieved when the frequency of the incident radiation matches the natural frequency of this collective oscillation. At this point, the amplitude of the electron oscillation is maximized. Consequently, both scaterring processes and CIGS absorption are significantly increased. The resonance condition is achieved when the real part of the metal dielectric function satisfies:

$$\mathrm{Re}[\epsilon(\omega)] = -2\epsilon_m, \tag{2.2}$$

where $\epsilon(\omega)$ is the dielectric response of the nanostructure and ϵ_m is the dielectric constant of the surrounding medium [78]. The resulting enhancement in optical performance arises from two main mechanisms, near-field and far-field scattering, as observable in Fig. 2.9. In near-field scattering, the nanoparticle generates a strongly confined evanescent electromagnetic field in its immediate surroundings. This evanescent field enhances light absorption in the surrounding medium, which is particularly useful if it is located in the absorber layer of a solar cell [77]. Far-field scattering involves the re-emission of radiation into the surrounding medium. In this case, the nanostructure redirects incident light into a broad angular distribution [10]. Additionally, the angular redistribution of light can increase the probability of total internal reflection inside the absorber layer, effectively extending the optical path length.

In 2017, Goffard et al. simulated nanostructured metallic back mirrors for CIGS devices with absorber layers ranging from 100 to $500\,\mathrm{nm}$ in thickness [79]. On top of the Mo layer,

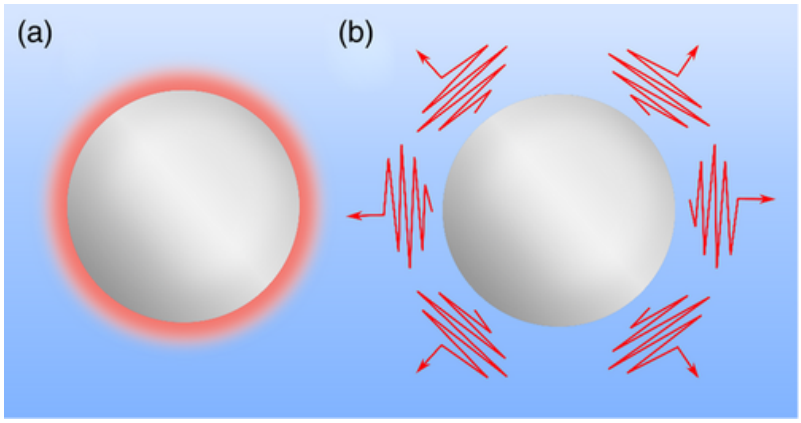
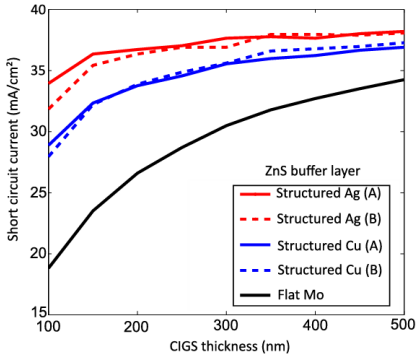


FIGURE 2.9: Schematic illustration of the effects resulting from plasmonic NPs interaction with light: **a)** near-field and **b)** far-field scattering [10].

periodic arrays of metallic nanostructures, such as grids (structure A) and pillars (structures B), of Ag and Cu were fabricated. Fig. 2.10 shows the simulated J_{sc} for different CIGS thickness values, on the different back contacts architectures. A $500\,\mathrm{nm}$ CIGS absorber deposited on a standard Mo back contact yielded a J_{sc} of $23.5\,\mathrm{mA\,cm^{-2}}$. When the Ag patterned nanostructures were implemented on the back contact, J_{sc} exceeded $36\,\mathrm{mA\,cm^{-2}}$, corresponding to a significant improvement of more than 50%. Despite being outperformed by Ag, Cu also presented an increase in J_{sc} values. Moreover, it was observed that the optical gains resulting from the structures were more significant for thinner absorbers, showing the importance of integrating light-management structures as the absorber thickness is reduced.



(A)

FIGURE 2.10: J_{sc} curves for a flat Mo back contact, a grid (structure A) or pillar (structure B) back mirrors made of Ag or Cu [79].

Dielectric nanostructures can also be used for optical path length enhancements. Even though they do not exhibit plasmonic behavior due to the absence of free electrons, they can still support resonant optical modes and are also used as a light-management strategy on the rear contact. When illuminated, the incident electromagnetic field induces

bound charge oscillations within the material, generating displacement currents [80]. If the nanostructure dimensions are comparable to the wavelength of light, these currents can support resonant modes, leading to electromagnetic field confinement inside the particle. In contrast with metallic nanostructures, this mechanism relies on direct polarization rather than free-electron motion, presenting no parasitic absorption [81]. This characteristic becomes important in bifacial solar cells, where light incident from the rear side should also be efficiently utilized. Since dielectric nanostructures do not significantly absorb rear-incident photons, they preserve the bifacial response of the solar cell, while still providing optical enhancements. Nonetheless, their near-field enhancement is generally weaker than in plasmonic systems, requiring larger particle sizes to achieve the same optical enhancement [82].

2.2.3 Spectral Conversion

In a solar cell, further energy losses are cause by the mismatch between the incident solar spectrum and the spectral absorption properties of the material [83]. Only photons of energy close to the bandgap are efficiently converted. An incident photon with lower energy than the bandgap will not be absorbed and no charge carriers are generated. The absorption of a photon with a higher energy than the bandgap will generate a carrier, albeit with excess energy, which is can be lost by a thermalization process [84].

Spectral conversion strategies seek to reshape the incident solar spectrum so that more photons arrive at the CIGS absorber in spectral regions where it converts light more efficiently. For that, there are three main techniques: down-conversion (DCo), down-shifting (DS) and up-conversion (UC). The first two involve absorbing higher energy photons and re-emitting them at lower energy values, normally at $600\,\mathrm{nm}$, which is the usual external quantum efficiency (EQE) peak of a CIGS cell [10], aiming to minimize thermalizations losses. Since higher energy photons can be lost by parasitic absorption at the window and buffer layers, the DCo and DS layers are usually deposited on the front contact [10, 84]. While DS is a one-to-one conversion process, DC converts one photon in two, also termed as ”quantum cutting” [85]. This can lead to a quantum efficiency of more than 100% pushing the SQ efficiency limit up to 40% [86, 87]. Conversely, UC combines the energy of two or more sub-bandgap photons into one that can be absorbed [84]. UC layers are usually deposited at the rear contact due to two main reasons: it does not hamper photon transmission before reaching the CIGS layer, and these low energy photons are neither absorbed nor reflected before reaching the back contact [88]. At least two photons are

needed to produce one usable photon, which results in quantum yield being limited to 50% [10]. Nonetheless, the research is still mostly on a theoretical level.

2.3. Nanofabrication

Nanofabrication refers to the set of techniques used to create structures with dimensions in the nanometer range [89]. These methods are central to modern micro and nanotechnology, enabling precise control over geometry, surface morphology, and material properties at length scales where physical phenomena such as quantum confinement, plasmonic resonances, and wave interference become relevant. Fabrication approaches are generally divided into two main categories: bottom-up and top-down methods [90]. Bottom-up strategies rely on the self-assembly of atoms, molecules, or nanoparticles into functional structures, often enabling excellent material quality but limited control over long-range ordering and deterministic patterning. In contrast, top-down approaches are based on the selective removal or modification of bulk material to define nanoscale features with high spatial precision.

2.3.1 Lithography

For top-down approaches, there are three main types of lithographic techniques: optical, such as photolithography (PL) and direct-write lithography (DWL); electronic, such as electron-beam lithography (EBL); and mechanical, such as nanoimprint lithography (NIL). PL represents the most established and widely used patterning technique forming the backbone of modern microelectronics manufacturing [64]. In this technique, ultraviolet (UV) light passes through or is reflected by a patterned mask, interacting with the photoresist. Depending on the resist chemistry, the exposed regions either become more soluble (positive resist) or less soluble (negative resist) in the developer solution. After development, a physical resist pattern remains, which can subsequently act as a mask for etching or deposition steps. Several properties like throughput, patterning resolution, and cost (CAPEX and OPEX), are considered when choosing a lithography technique. Despite having high throughput, PL resolution is fundamentally limited by the Rayleigh resolution limit, highly dependent on light wavelength used during exposure [91, 92]. The resolution may be further improved by reducing the used wavelength, like in deep-UV PL ($193\,\mathrm{nm}$) and extreme-UV PL ($13.5\,\mathrm{nm}$) systems, even though this requires highly complex machinery and high capital and operational costs [64, 92].

NIL emerges as a cost-effective alternative, with an inherent high resolution (sub $10\,\mathrm{nm}$), while offering high throughput potential, particularly when implemented in a roll-to-roll (R2R) configuration [64]. In this technique, a rigid or flexible mold (master stamp), containing the desired nanoscale features, is mechanically pressed into a thin layer of a deformable polymer (resist), transferring the mold's pattern through direct physical deformation. The polymer layer is subsequently hardened and permanently set using a thermal or UV-based curing process.

2.3.2 Etching

Etching is a fundamental step in nanofabrication that is broadly divided into two main categories: wet and dry etching. Wet etching is a purely chemical process where the wafer is immersed in a solution bath, leading to chemical reactions and the subsequent dissolution of the target material. Because it relies on specific chemical reactivities, this method offers high etching selectivity, removing the target material while leaving other materials intact [93]. However, due to its chemical nature, it is inherently isotropic, meaning it etches equally in all directions, as illustrated in Fig. 2.11. Conversely, dry etching enables high anisotropy (Fig. 2.11) and is mostly a plasma-based approach utilizing techniques such as ion beam etching (IBE), also knows as ion milling, and reactive ion etching (RIE) [94]. IBE employs an argon (Ar) plasma and an electrical field to accelerate Ar^+ towards the wafer surface. Since the plasma is inert, the material is removed entirely through physical sputtering, resulting in low etching selectivity. On the other hand, RIE introduces specific gases into the chamber to generate chemically reactive species that are carefully chosen to form volatile compounds upon contact with the target material [94]. By combining this chemical reactivity with the physical sputtering action of the plasma ions, RIE successfully achieves both high anisotropy and significantly improved etching selectivity.

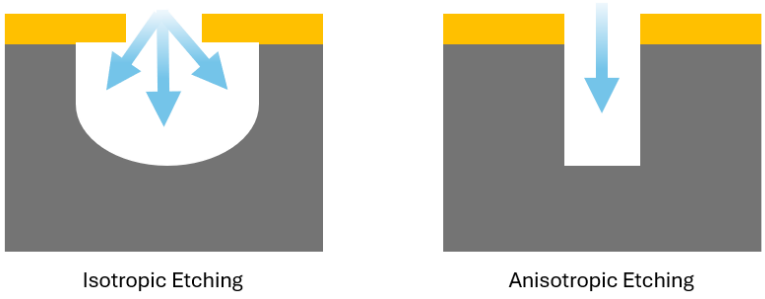


FIGURE 2.11: Schematic representation of an anisotropic and an isotropic etch.

Throughout the research conducted in this thesis, various structures with nanoscale features were fabricated and characterized. Consequently, NIL was employed as the patterning technique, offering both the high resolution necessary for nanoscale precision and a high throughput process flow that facilitated rapid feedback between characterization and fabrication adjustments. Furthermore, due to its low cost and inherent scalability, the use of NIL established a viable pathway for transitioning the fabrication of light-management nanostructures into an industrial-scale environment. Complementing these lithographic steps, a combination of wet and dry etching techniques was implemented throughout the fabrication process flow. These etching processes were carefully selected for each application, with adjusted conditions according to material compatibility, desired anisotropy, and the required etching selectivity.

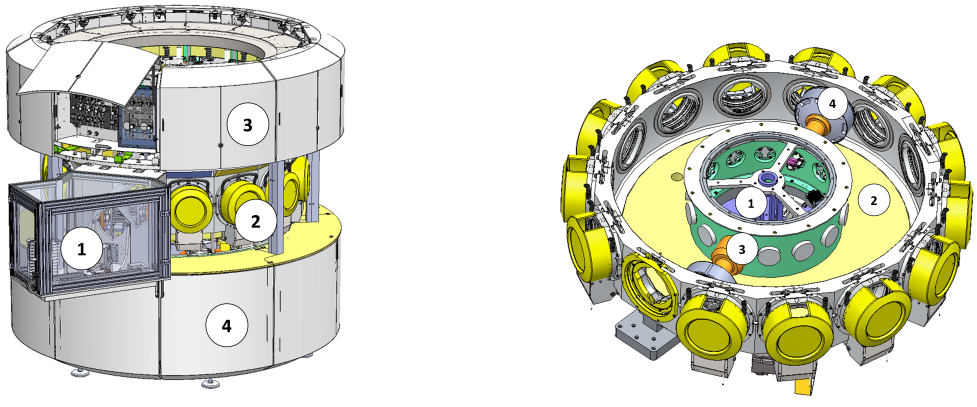
3. Experimental Methods

3.1. Development of ultrathin flexible CIGS solar cells with integrated SiO_x pillars

The development of ultrathin flexible CIGS solar cells with integrated SiO_x pillars was divided into 2 main parts. These consisted on the characterization of the thickness reduction impact on CIGS solar cells, and then on the development and optimization of a process flow for the fabrication of SiO_x pillars on a SS flexible substrate.

3.1.1 Ultrathin flexible CIGS solar cells

The fabrication of the ultrathin CIGS solar cells was carried out using an industrial sputtering system, the Midsummer UNO, designed for the deposition of high-quality CIGS absorber layers and full device stacks [95]. The Midsummer UNO is composed of multiple vacuum chambers organized in a circular configuration, as illustrated in Fig. 3.1a) and b). The system includes a loadlock (LL) chamber, a transfer chamber, and a series of 13 sputtering chambers, each dedicated to the deposition of specific materials. The SS substrates are introduced through the LL and transported between sputtering chambers via a central transfer system (arm) under controlled vacuum conditions [95]. Each sputtering chamber is equipped with independently controlled targets, allowing the definition of deposition parameters such as power, pressure, and time.



(A) (B)

FIGURE 3.1: **a)** UNO diagram: 1) LL chamber; 2) Sputter Station; 3) Upper Electric Cabinets; 4) Lower Cabinets. **b)** Sputter station diagram: 1) Inner chamber; 2) Transfer chamber; 3) Pneumatic Cylinder Assy; 4) Cooling Hub.

The devices were fabricated on $160\,\mu m$-thick $15.6x15.6\,cm^2$ SS substrates in order to ensure a flexible solar cell. The substrates were initially coated with a titanium-tungsten

(TiW, $208\,\mathrm{nm}$) diffusion barrier layer to prevent impurities of the SS substrate from diffusing into the active layers of the solar cell. A Na-doped Mo layer (MoNa, $351\,\mathrm{nm}$) was then deposited to act as a Na source. Finally, a Mo rear contact ($104\,\mathrm{nm}$) was deposited to provide the rear electrical contact of the solar cell.

The absorber structure consisted of a thin CGS seed layer ($65\,\mathrm{nm}$), followed by an In_2Se_3 layer ($48\,\mathrm{nm}$), and a CIGS absorber divided into three sublayers with different Gallium to Group III (GGI, [Ga]/([Ga]+[In])) ratios: CIGS 10% ($300\,\mathrm{nm}$), CIGS 7% ($300\,\mathrm{nm}$), and CIGS 5% ($300\,\mathrm{nm}$). These sublayers's thickness values correspond to the $0.9\,\mu\mathrm{m}$ total absorber thickness. This Ga grading enables bandgap engineering across the absorber thickness, improving carrier collection and reducing recombination losses at the rear interface by creating a quasi-electric field that drives electrons away from the rear interface, which is typically defect-rich and prone to recombination [96].

After the absorber deposition, a second In_2Se_3 layer ($35\,\mathrm{nm}$) and an In_2S_3 buffer layer ($33\,\mathrm{nm}$) were deposited to form the p–n junction and reduce interface recombination. The optical window structure was then completed with a ZMO layer ($96\,\mathrm{nm}$), acting as a transparent window layer, followed by an ITO layer ($174\,\mathrm{nm}$), which served as the front electrical contact while maintaining high optical transparency.

One of the key aspects of this work was to explore the fabrication of ultrathin absorber layers with varying thickness values: 1.1, 0.9, 0.7, 0.5 and $0.3\,\mu\mathrm{m}$. The thickness was controlled by adjusting the sputtering energy applied to the CIGS targets, assuming this parameter has a linear relationship with the deposited amount. Therefore, the resulting thickness values should be considered approximate and this methodology remains experimental.

After full fabrication of the solar cell in the Midsummer UNO system, Ag-based grids were deposited on the ITO front contact to ensure proper charge extraction. A Dimatix Materials Printer DMP-2850 from FUJIFILM inkjet system was used to define the 16 contacts for each cell, named from A1 to D4. Three layers of a nano Ag inkjet-printable ink from Dycotec Materials (DM-SIJ-3206) were deposited. An annealling procedure was then carried out using the UF-55 oven from Memmert: $30\,\mathrm{min}$ at $120\,^{\circ}\mathrm{C}$, followed by $30\,\mathrm{min}$ at $230\,^{\circ}\mathrm{C}$.

Following this step, the contacts were separated by mechanical scribing with a diamond-tip pen, isolating the contacts in $1\,\mathrm{cm}^2$ cells. Ideally, the scribing should be executed

with the same pressure in all of the contacts, ensuring uniformity throughout the various cells. However, since this was a manual procedure, and therefore user-dependent, the consistency of the scribing may have varied between different contacts and solar cells, adding a source of error to the measurements, specially in FF. To prepare the cell for characterization, the rear contact must be exposed for charge extraction. For that reason, the solar cell stack was mechanically removed with a scalpel at the edges of the substrate. In was then welded in these exposed areas to ensure a low-resistance electrical contact with the measuring tips.

3.1.2 Development of SiO_x pillars on SS flexible substrates

The schematic overview of the process flow for the fabrication of SiO_x pillars on SS flexible substrates can be seen in Fig. 3.2.

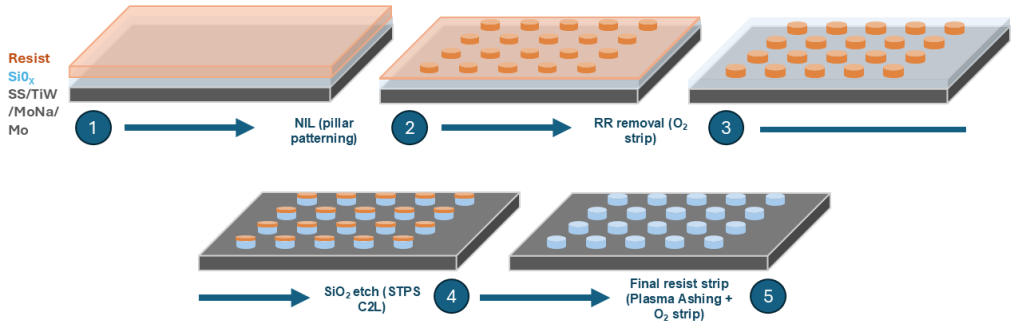


FIGURE 3.2: Schematic overview of the process flow for the fabrication of SiO_x pillars on SS flexible substrates.

SS substrates coated with a TiW/MoNa/Mo rear contact stack deposited in the Midsummer UNO system were used. Prior to thin-film deposition, substrates were cleaned by ultrasonic agitation at room temperature (RT): $15\,\mathrm{min}$ in acetone, followed by $10\,\mathrm{min}$ in isopropanol (IPA), and $5\,\mathrm{min}$ in deionized (DI) water at RT. The substrates were then blow-dried using a nitrogen (N_2) gun. A nominal $150\,\mathrm{nm}$ SiO_x layer was deposited by plasma-enhanced chemical vapor deposition (PECVD), following the conditions: substrate temperature (T) = $200\,^{\circ}\mathrm{C}$; pressure = $550\ \mathrm{mTorr}$; gas flows = $12\ \mathrm{sccm}$ (SiH_4), $1420\ \mathrm{sccm}$ (N_2O), $392\ \mathrm{sccm}$ (N_2); power (P) = $60\,\mathrm{W}$.

A UV-curing resist (mr-NIL6001.0E) was diluted in ma-T 1045, an organic solvent based thinner from the same supplier as the resist, on a 1:2 weight ratio. The resist was then spin-coated using a Karl Süss E-Beam Track system at 3000 rpm for $60\,\mathrm{s}$, followed by a baking process at $65\,^{\circ}\mathrm{C}$ for $90\,\mathrm{s}$ (Fig. 3.2 (1)). This process yielded a final resist thickness of approximately $130\,\mathrm{nm}$.

A pillar master stamp, previously fabricated by EBL, was first cleaned by medium power (MP) plasma ashing using the PVA Tepla GIGAbatch 360M system, following the conditions: $2.45\,\mathrm{GHz}$ P = $500\,\mathrm{W}$, pressure = $0.2\,\mathrm{mbar}$, gas flow = $600\ \mathrm{sccm}$ (O_2), $50\ \mathrm{sccm}$ (Ar), duration = $8\,\mathrm{min}$. The pillar architecture of this master stamp presented a radius (r) of $225\,\mathrm{nm}$, a spacing (a) of $100\,\mathrm{nm}$, and an height (h) of $150\,\mathrm{nm}$. The master stamp was coated with a $30\,\mathrm{nm}$-thick anti-sticking layer (ASL) based on a passivating carbon-fluoride (C_xF_y) polymer by exposure to a octafluorocyclobutane (C_4F_8) plasma in an inductively coupled plasma-reactive ion etching (ICP-RIE) system (SPTS Pegasus), following the conditions: platten T = $20\,^{\circ}\mathrm{C}$, $13.56\,\mathrm{MHz}$ platen P = $0\,\mathrm{W}$, $13.56\,\mathrm{MHz}$ coil P = $2000\,\mathrm{W}$ pressure = $2.5\ \mathrm{mTorr}$. For the NIL process, a two-step UV-NIL procedure by Obducat Eitre 8 NIL was carried out. First, an pattern intermediate polymer stamp (IPS) was patterned by a high pressure contact with the master stamp, following the conditions: T = $22\,^{\circ}\mathrm{C}$, pressure = $15\,\mathrm{bar}$, and UV = off for $60\,\mathrm{s}$, on for the remaining $240\,\mathrm{s}$. The IPS was then coated with a $30\,\mathrm{nm}$-thick ASL. For the second NIL step, the IPS pattern was transferred to the resist using simultaneous thermal and UV (STU) NIL process, following the conditions: T = $65\,^{\circ}\mathrm{C}$, P = $15\,\mathrm{bar}$, and UV = off for $100\,\mathrm{s}$, on for the remaining $180\,\mathrm{s}$ (Fig. 3.2 (2)). The molding and demolding steps require particular care to avoid air bubbles and defects in the imprint.

After patterning, a flat non-patterned residual resist (RR) layer is present, which needs to be removed to ensure proper exposure of the underlying SiO_x layer. The RR removal was carried out by a $6\,\mathrm{s}$ O_2-based RIE (O_2 strip) using the SPTS Pegasus system, following the conditions: platen T = $20\,^{\circ}\mathrm{C}$, pressure = $20\ \mathrm{mTorr}$, $13.56\,\mathrm{MHz}$ platen P = $180\,\mathrm{W}$, $13.56\,\mathrm{MHz}$ coil P = $2500\,\mathrm{W}$, and gas flow = $115\ \mathrm{sccm}$ (O_2) (Fig. 3.2 (3)). The SiO_x layer was subsequently etched using RIE in the SPTS C2L inductively coupled plasma (ICP) system, following the recipe conditions: platen T = $50\,^{\circ}\mathrm{C}$, chamber T = $50\,^{\circ}\mathrm{C}$, pressure = $12\ \mathrm{sccm}$, $13.56\,\mathrm{MHz}$ platen P = $250\,\mathrm{W}$, $13.56\,\mathrm{MHz}$ coil P = $625\,\mathrm{W}$ gas flow = $50\ \mathrm{sccm}$ (CF_4), $70\ \mathrm{sccm}$ (H_2), referred to as the "SiO_x Etch" recipe (Fig. 3.2 (4)). Any remaining resist was removed by a final MP plasma ashing and $5\,\mathrm{min}$ O_2 strip (Fig. 3.2 (5)). The results for the development and optimization of this process flow will be shown and discussed in the

following chapter.

The resulting samples were cleaned by ultrasonic agitation at RT: $15\,\mathrm{min}$ in acetone, followed by $10\,\mathrm{min}$ in IPA, and $5\,\mathrm{min}$ in DI water at RT, before complete solar cell deposition in the Midsummer UNO system.

3.2. Development of Au pillars encapsulated by a dielectric on a bifacial substrate

3.2.1 Overview of the Fabricated Series

Before fabrication, optical FDTD simulations were performed within the NOA/Salomé group at INL, to find the optimum Au pillars array dimensions (r, a, and h) targeting the maximum CIGS absorptance, and therefore, J_{sc} enhancement. Two optimum architectures were determined depending on the illumination conditions: front (r = $150\,\mathrm{nm}$, a = $100\,\mathrm{nm}$, and h = $50\,\mathrm{nm}$) or bifacial illumination (r = $100\,\mathrm{nm}$, a = $200\,\mathrm{nm}$, and h = $60\,\mathrm{nm}$), henceforth referred to as architectures R150 and R100, respectively.

To further evaluate the impact of dielectric encapsulation and pillar dimensions on the optical performance, the fabricated samples were divided into three main series: Series A, B, and C. In order for Au not to diffuse into the CIGS layer, the pillars were encapsulated by a dielectric layer, which was patterned by contact openings to ensure electrical contact between CIGS and ITO. The studied series were defined as follows:

- **Series A (Optimized Architecture for Front Illumination – Dielectric Material Variation): R150 architecture** Different dielectric materials were tested: SiO_x, titanium oxide (TiO_2), and aluminum oxide (Al_2O_3). The encapsulation thickness was kept constant at $20\,\mathrm{nm}$.
- **Series B (Optimized Architecture for Bifacial Illumination – Dielectric Material Variation): R100 architecture** Different dielectric materials were tested: SiO_x, TiO_2, and Al_2O_3. The encapsulation thickness was kept constant at $20\,\mathrm{nm}$.
- **Series C (Optimized Architecture for Front Illumination – Dielectric Thickness Variation): R150 architecture** Different encapsulation thickness values were tested: 10, 20, and $40\,\mathrm{nm}$. Al_2O_3 was used as the dielectric material.

3.2.2 Fabrication Process Flow

The schematic overview of the process flow for the fabrication of Au pillars encapsulated by a dielectric on an ITO rigid substrate process flow can be seen in Fig. 3.3.

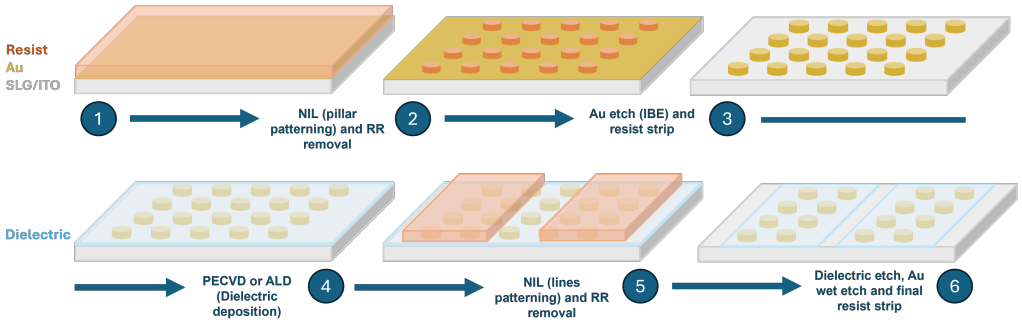


FIGURE 3.3: Schematic overview of the process flow for the fabrication of Au pillars encapsulated by a dielectric on a lines configuration, on an ITO rigid substrate process flow.

ITO-coated SLG (5x$5\,\mathrm{cm}^2$) with a thickness of $1.1\,\mathrm{mm}$ was used as the substrate. These were cleaned by ultrasonic agitation at RT: $15\,\mathrm{min}$ in acetone, followed by $10\,\mathrm{min}$ in IPA and $5\,\mathrm{min}$ in DI water at RT. The substrates were then blow-dried using a N_2 gun. The following fabrication conditions varied slightly depending on the architecture (R150 or R100).

An Au layer was deposited by $100\,\mathrm{W}$ DC sputtering in the Kenosistec UHV PVD tool. The thickness of this layer varied based on the target h of the Au pillar (50 or $60\,\mathrm{nm}$). For the resist layer, mr-NIL 6001.0E was diluted in ma-T 1045 in a 1:3 weight ratio. For R150, the resist was spin-coated at 3000 rpm for $60\,\mathrm{s}$, followed by a baking process at $65\,^{\circ}\mathrm{C}$ for $90\,\mathrm{s}$, yielding a final thickness of $150\,\mathrm{nm}$. Whereas for R100, the same spin-coating was performed at 4000 rpm, yielding a final thickness of $130\,\mathrm{nm}$ (Fig. 3.3 (1)).

Two NIL master stamps were produced by EBL (r = 150 or $100\,\mathrm{nm}$, a = 100 or $200\,\mathrm{nm}$, and h = $200\,\mathrm{nm}$). NIL was then carried out to pattern the resist (Fig. 3.3 (2)), and the RR layer was removed by O_2 strip ($6\,\mathrm{s}$ for R150; $12\,\mathrm{s}$ for R100). The Au was etched using IBE in the Nordiko Ion Milling system, following the conditions: $13.56\,\mathrm{MHz}$ RF P = $300\,\mathrm{W}$, positive grid voltage = $400\,\mathrm{V}$, negative grid voltage = $2500\,\mathrm{V}$, pressure = $0.43\,\mathrm{mTorr}$, gas flow = $60\,\mathrm{sccm}$ (Ar) (Fig. 3.3 (3)). A secondary ion mass spectroscopy (SIMS) probe was used to detect real-time material etching. This allowed to stop the ion milling after a significant decrease in the ^{197}Au signal, and a slight increase in the ^{115}In one, preventing over-etch of the ITO layer. In this system, different milling angles can be used, where a 90° angle corresponds to a milling process where the ion beam is incident normally to the substrate. An intermittent 110° etch ($540\,\mathrm{s}$, $60\,\mathrm{s}$ on/$60\,\mathrm{s}$ off) was first executed as the main etching to

form the Au pillars. As this process caused significant Au redeposition around and on top of the pillars, additional IBE steps were performed. For R150, a continuous $130°$ etch during $120\,\mathrm{s}$, followed by a continuous $165°$ etch for $900\,\mathrm{s}$, while for R100, a continuous $165°$ etch for $240\,\mathrm{s}$. To remove the remaining resist after the etch, the samples underwent 3 cycles of high power (HP) plasma ashing, following the conditions: $2.45\,\mathrm{MHz}$ P = $800\,\mathrm{W}$, pressure = $0.2\,\mathrm{mbar}$, gas flow = $800\ \mathrm{sccm}$ (O_2), $50\ \mathrm{sccm}$ (Ar), duration = $1\,\mathrm{min}$; finalized by a $2\,\mathrm{min}$ O_2 strip.

The different dielectric materials used for this encapsulation were SiO_x, TiO_2 and Al_2O_3. SiO_x was deposited by PECVD, while both TiO_2 and Al_2O_3 were deposited using atomic layer deposition (ALD) (Fig. 3.3 (4)). For TiO_2, the following conditions were used: T = $200\,°\mathrm{C}$, gas flows = $200\ \mathrm{sccm}$ (Tetrakis(dimethylamido)titanium, TDMAT) for $500\,\mathrm{ms}$, followed by a $500\,\mathrm{ms}$ purge + $600\ \mathrm{sccm}$ (ozone, O_3) for $1500\,\mathrm{ms}$, followed by a $3000\,\mathrm{ms}$ purge. For Al_2O_3: T = $200\,°\mathrm{C}$, gas flows = $200\ \mathrm{sccm}$ (trimethylaluminum, TMA) for $150\,\mathrm{ms}$, followed by a $750\,\mathrm{ms}$ purge + $600\ \mathrm{sccm}$ (H_2O) for $150\,\mathrm{ms}$, followed by a $1000\,\mathrm{ms}$ purge.

A second NIL process was used to define the contact openings in the dielectric layer, for which two architectures were used: i) lines ($2.8\,\mu\mathrm{m}$ pitch; $800\,\mathrm{nm}$ width); and ii) holes ($2.0\,\mu\mathrm{m}$ pitch; $400\,\mathrm{nm}$ diameter arranged in a hexagonal array). The corresponding master stamps were fabricated using i) DWL, and ii) EBL. For the lines architecture, the samples were spin-coated with mr-NIL 6001.0E diluted in maT-1045 in a 1:2 weight ratio, while for the holes architecture a 1:1.5 ratio was used. For both architectures, the samples were spin-coated at 4000 rpm for $60\,\mathrm{s}$ and baked at $65\,°\mathrm{C}$, yielding thickness values of $177\,\mathrm{nm}$ and $220\,\mathrm{nm}$ for the lines and holes, respectively (Fig. 3.3 (5)). After the NIL process, the RR layer was removed by $12\,\mathrm{s}$ O_2 strip. The dielectric layer was etched by continuous IBE at $130°$. The IBE duration varied according to the dielectric material and thickness, defined by the SIMS signal of ^{28}Si, ^{48}Ti or ^{27}Al.

After the dielectric etch, some Au pillars are left exposed. To avoid Au diffusion into the CIGS layer, these must be removed. For this purpose, the samples were immersed in a commercial potassium iodide (KI) + iodine (I_2) solution diluted in water (Technietch ACI2), for $1\,\mathrm{min}$ at RT with slight agitation. Lastly, to clear all the remaining resist in the sample, 3 cycles of low power (LP) plasma ashing were performed, following the conditions: $2.45\,\mathrm{MHz}$ P = $230\,\mathrm{W}$, pressure = $0.2\,\mathrm{mbar}$, gas flow = $200\ \mathrm{sccm}$ (O_2), $200\ \mathrm{sccm}$ (Ar), duration = $6\,\mathrm{min}$ (Fig. 3.3 (6)). The results for the development and optimization of this process flow will be shown and discussed in the following chapter.

Developed within the European Hi-Bits project, the Au pillar sample series was designed to enhance the optical performance of bifacial ultrathin-film CIGS solar cells. Because the Midsummer UNO system is incompatible with the rigid ITO substrates, the samples were sent to an external project partner, Uppsala University, for complete solar cell fabrication, via CIGS evaporation. As this deposition process is currently on standby, final solar cell performance results are not included in this work. Nevertheless, to assess the viability of the Au pillar encapsulation and evaluate its effectiveness in preventing Au diffusion into the active layers, dielectric-encapsulated Au pillars were fabricated on SS TiW/MoNa/Mo substrates.

3.3. Characterization

Various characterization methods were employed to evaluate both the fabricated light-management nanostructures and the ultrathin CIGS solar cells. The characterization focused on morphology, topography, optical response, and optoelectronic performance. The SEM from NovaNano FEI 950 was employed for morphological analysis of the fabricated light-management nanostructures and the ultrathin CIGS solar cells. For the Au pillar samples, SEM was used to evaluate geometrical parameters including h, r, a and length/diameter of the contact openings. These dimensions were evaluated using the Fiji software from ImageJ. Despite the SEM system being capable of performing direct measurements, a small deviation was observed. Therefore, a correction was applied using the pitch as a reference. Energy-dispersive X-ray spectroscopy (EDS), coupled with SEM, was used to perform elemental analysis of the fabricated nanostructures. For the ultrathin CIGS solar cells, SEM was used for cross-sectional imaging in order to confirm the thickness of the absorber layer and to evaluate the morphology of the SiO_x pillars cell layers. Transmission electron microscopy (TEM) was additionally employed during the study of Au pillars integration into ultrathin flexible CIGS solar cells, using the FEI Titan G2 ChemiSTEM system. Due to its superior imaging resolution compared to SEM, TEM allowed a more detailed investigation of the fabricated structures and interfaces. The cross-sectional lamellas were prepared using a were prepared using a FEI Helios NanoLab 450S focused ion beam (FIB) system. The Dimension Icon atomic force microscope from Bruker was used on tapping mode at $0.5\,\mathrm{Hz}$ to characterize the topography of the fabricated nanostructures, and the results were analyzed using the Gwyddion 2.70 software. Atomic force microscopy (AFM) provides high-resolution 3D h profiles, enabling the assessment of fabrication-related features such as over-etching, and whether the contact openings are well defined. The optical behavior of the fabricated nanostructures was

analyzed using UV-Vis-NIR spectrophotometry, enabling the measurement of both the total and diffuse components of transmittance and reflectance. The measurements were performed using the integrating sphere of the Lambda 1050+ UV/Vis/NIR system from PerkinElmer, ranging from 300 to $1200\,\mathrm{nm}$ with a step of $5\,\mathrm{nm}$.

The performance of the ultrathin CIGS solar cells was evaluated through current density-voltage (JV) and EQE measurements. JV measurements were used to extract three of the main figures of merit: V_{oc}, FF and η. The J_{sc} parameter was obtained via EQE since, unlike JV, it introduces no shading effect during measurements. The JV setup consisted of two main components: a solar simulator and a sourcemeter. The solar simulator was an Oriel Sol3A from NEWPORT, capable of delivering an AM1.5G spectrum under which all measurements were performed. A lamp power of $1300\,\mathrm{W}$ was used, and a reference Si solar cell was employed to calibrate the irradiance. As the sourcemeter, the Keithley 2400 was used. For the EQE measurements, the QuantX 300 system from NEWPORT was used. Measurements were obtained in the 330 to $1150\,\mathrm{nm}$ wavelength range with a $10\,\mathrm{nm}$ step. The final J_{sc} value of each sample was automatically calculated by integrating the product of EQE and AM1.5G spectrum P:

$$J_{\mathrm{sc}} = \frac{q}{hc} \int_{\lambda_{\mathrm{min}}}^{\lambda_{\mathrm{max}}} \mathrm{EQE}(\lambda)\, P_{\mathrm{in}}(\lambda)\, \lambda\, d\lambda, \tag{3.1}$$

where q is the elementary charge, h is Planck's constant, c is the speed of light in vacuum, λ_{min} and λ_{max} are the integration limits (330–$1150\,\mathrm{nm}$, respectively), and P_{in} is the AM1.5G spectrum P.

4. Results and Discussion

4.1. SiO_x Pillars on SS Flexible Substrates Process Flow Optimization

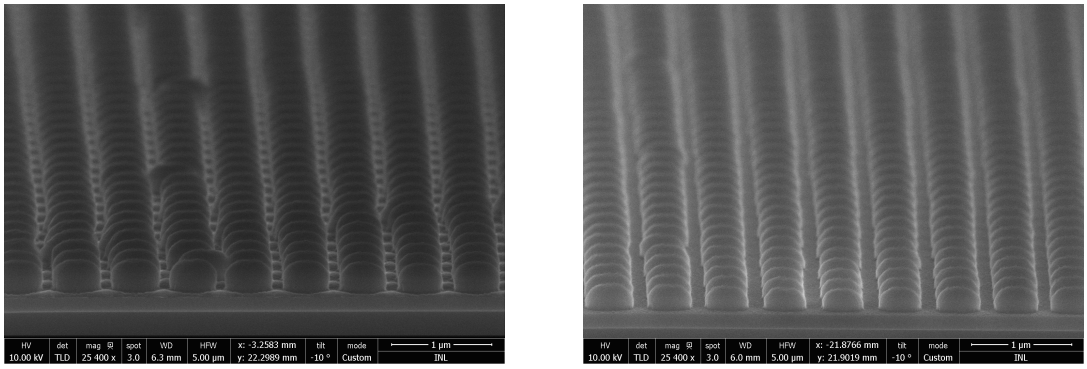
The fabrication of SiO_x pillars (r = 150 nm, a = 100 nm, and h = 150 nm) on flexible SS substrates required the optimization of multiple fabrication steps to ensure good pattern transfer, uniform pillar formation, and compatibility with the subsequent solar cell deposition processes. The dimensions were obtained by previous simulations made within the NOA/Salomé group at INL, with the objective of providing the maximum optical gain possible. The optimization of this process flow was performed through systematic variation of the fabrication parameters, followed by inspection using SEM and AFM. In the end, an optical analysis was performed by UV-Vis-NIR spectrophotometry.

4.1.1 RR removal

After SiO_x deposition on the TiW/MoNa/Mo substrate, a layer of resist was spin-coated. The pillar master stamp architeture was then imprinted on the resist and the RR layer had to be removed, which was done by O_2 strip. Various times of etching were tested: 5, 7 and 9 s. These tests were performed on Si substrates to facilitate SEM imaging. The representative cross-section SEM images of the sample after the imprint and after 7 s O_2 strip can be seen in Fig. 4.1a) and b), respectively. As seen after the imprint, the RR layer is thin (around 20 nm), therefore it was easily removed by every tested time. It is possible to observe that the 7 s sample removed the RR layer and didn't affect the patterned resist. Despite all three tested O_2 strip durations (5, 7, and 9 s) successfully removed the RR layer without causing any noticeable impact to the patterned resist, a 7 s O_2 strip was selected for the subsequent process steps, as it offers a robust processing window.

4.1.2 SiO_x etch

After removing the RR layer, the samples underwent SiO_x etching. Firstly, the SPTS advanced plasma system (APS) of the SPTS system was used. When previously fabricated on 5x5 cm^2 ITO-coated SLG substrates, the recipe "APS SiO_2 Etch" (uses C_4F_8 in a molecular hydrogen (H_2) environment) is used, following the conditions: platen T = 0 °C, chamber T = 100 °C, pressure = 5 mTorr, 13.56 MHz platen P = 700 W, 13.56 MHz coil P = 2000 W, gas flow = 50 sccm (C_4F_8), 30 sccm (H_2), allowing for etch rate values of 460



(A) (B)

FIGURE 4.1: Representative cross-section SEM images of the imprinted pillars pattern on the resist layer on SiO_x-coated Si substrates: **a)** after imprint; **b)** after $7\,\mathrm{s}$ O_2 strip.

and $103\,\mathrm{nm\,min^{-1}}$ for SiO_x and resist, respectively. This procedure yielded high etching selectivity and reproducibility, resulting in a good pattern transfer, as seen in Fig 4.2a). The next step was to test it on a $5\mathrm{x}5\,\mathrm{cm^2}$ SS sample. The etch was successful, resulting equally in a good pattern transfer, as seen in Fig 4.2b). Finally, a whole substrate ($15.6\mathrm{x}15.6\,\mathrm{cm^2}$) was tested on this system. The results showed that the pillars deformed and there are still residues on the samples, indicating bad etching quality, as seen in Fig 4.2c). The thermal contact between the substrate and the support wafer may have not been well established and the substrate may have bent under T changes. This suggests that the substrate was not properly cooled, ultimately changing the chemical reactivity in the plasma chamber during the etching process.

Following these results, a different module of the SPTS system was tested. This module provided less substrate bending as it uses a lower process T. The recipe "Slow SiO_2 Etch", which presented the best SiO_x/mr-NIL6001.0E resist selectivity, was used, following the conditions: platen T = $40\,^{\circ}\mathrm{C}$, chamber T = $50\,^{\circ}\mathrm{C}$, pressure = $5\ \mathrm{mTorr}$, $13.56\,\mathrm{MHz}$ platen P = $50\,\mathrm{W}$, $13.56\,\mathrm{MHz}$ coil P = $1300\,\mathrm{W}$, gas flow = $30\ \mathrm{sccm}$ (CF_4). However, it uses tetrafluoromethane (CF_4), which produces a much higher F/C ratio in the plasma than C_4F_8, used in the last test. This means that the selectivity is worse in the following test, since a lower F/C ratio provides better selectivity of SiO_x over resist [97]. This recipe allowed for etch rate values of 130 and $118\,\mathrm{nm\,min^{-1}}$ for SiO_x and resist, respectively. Various times of etching were tested, such as 90, 100, and $120\,\mathrm{s}$. The representative top-view SEM images of the sample after RR removal and after the different "Slow SiO_x Etch" times (90, 100, and $120\,\mathrm{s}$) can be seen in Fig. 4.3a), b), c), and d), respectively. The sample with $90\,\mathrm{s}$ of etch still presented a layer of SiO_x between the pillars, showing that this etching time was not enough. Furthermore, it can be seen that some agglomerates formed between

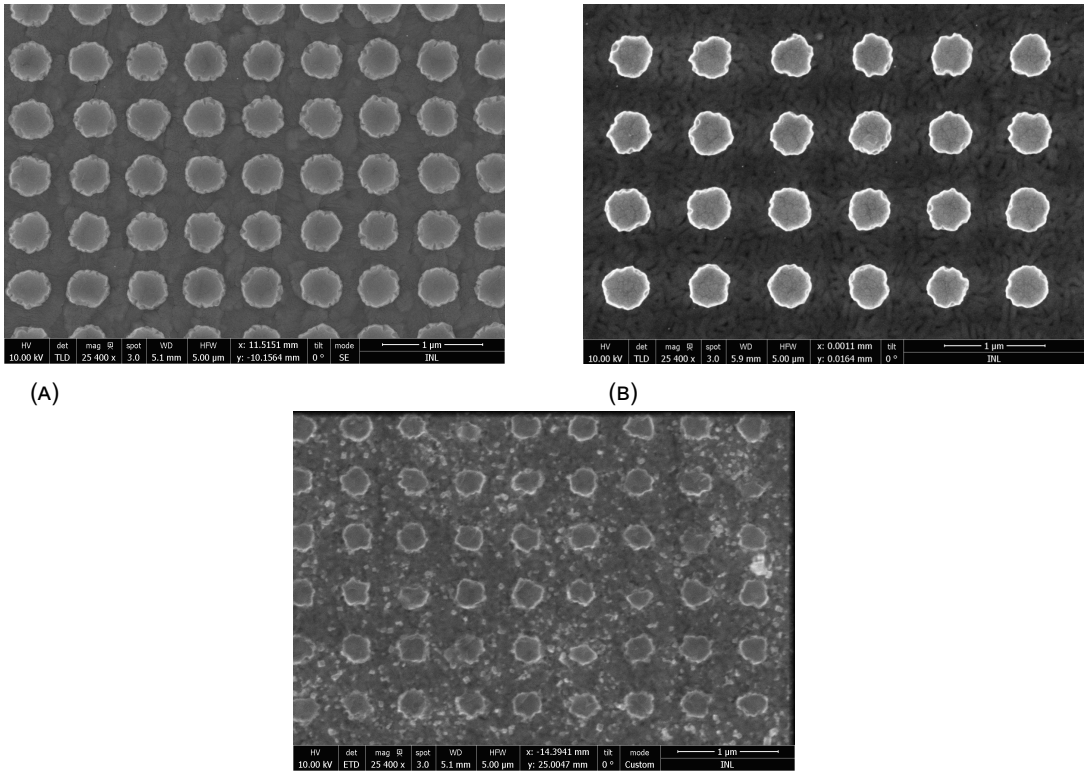


FIGURE 4.2: Representative cross-section SEM image of the pillars after the "APS SiO_2 Etch" etch tests: **a** Sample with an ITO-coated SLG substrate; **b)** $5\text{x}5\,\text{cm}^2$ SS sample; **c)** $15.6\text{x}15.6\,\text{cm}^2$ SS sample.

the pillars. Analyzing the remaining etching times, $100\,\text{s}$ was enough to fully etch the SiO_x layer without compromising the pillars, despite forming some agglomerates. However, for the $120\,\text{s}$ etch, over-etch of the Mo layer was present, and the pillars were deformed. Moreover, for both cases, due to the low selectivity of this process, the remaining resist was either thin or non-existent, indicating it may be difficult to achieve reproducibility. Despite not being ideal, a $500\,\text{nm}$ CIGS solar cell was fabricated out of the $100\,\text{s}$ ICP etch sample. However, the agglomerates influenced the deposition of CIGS and the solar cell presented efficiency values lower than 1%. A SEM-EDS analysis was performed, as seen in Fig. 4.4, and it can be observed that there are F-based residues in the agglomerates.

A new recipe in the ICP module was tested, "Al_2O_3 Etch", which used boron trichloride (BCl_3) instead of F-based chemistry, to avoid the formation of agglomerates. The reference (no etch) and the results for the three testing times (60, 90 and $120\,\text{s}$) can be seen in Fig. 4.5a), b), c), and d), respectively. It is possible to observe that the etch was not performed in every tested etch time. Instead, a new layer formed on top of the SiO_x, avoiding its removal. After a SEM-EDS analysis was performed, it was possible to conclude that this layer was composed of boron (B). This indicates that it may be boron oxide, and that

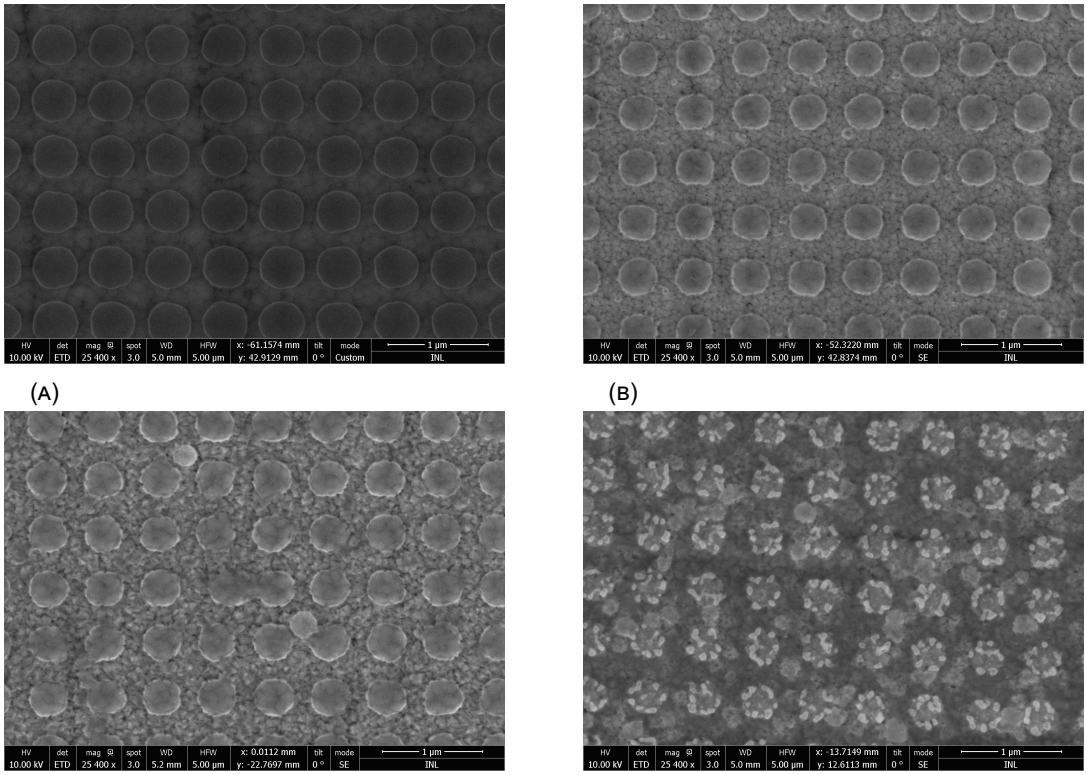


FIGURE 4.3: Representative top-view SEM images of the SiO_x etch tests using the "Slow SiO_x Etch" recipe. After: **a)** RR removal, **b)** $90\,s$, **c)** $100\,s$, and **d)** $120\,s$ "Slow SiO_x Etch".

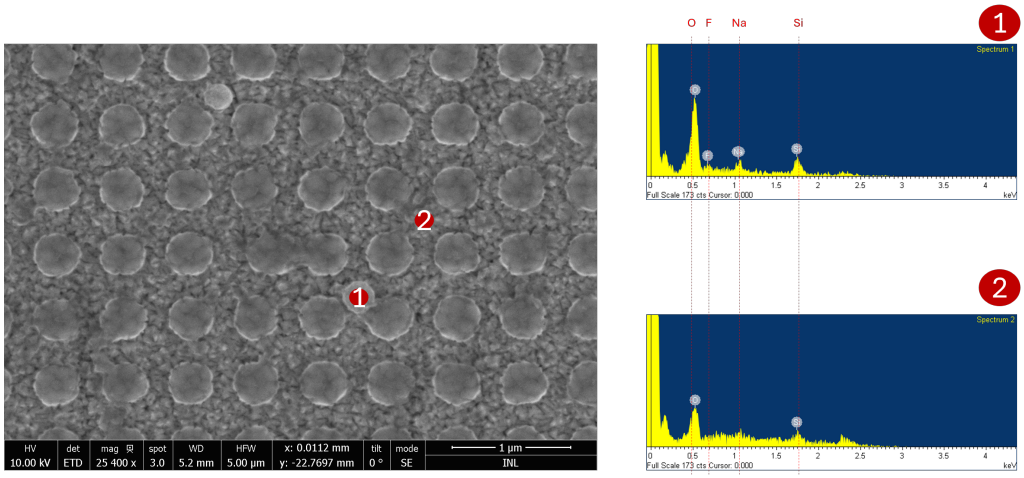


FIGURE 4.4: SEM-EDS analysis of the agglomerates formed between the pillars when using the "Slow SiO_2 Etch".

the etch using this recipe is not viable.

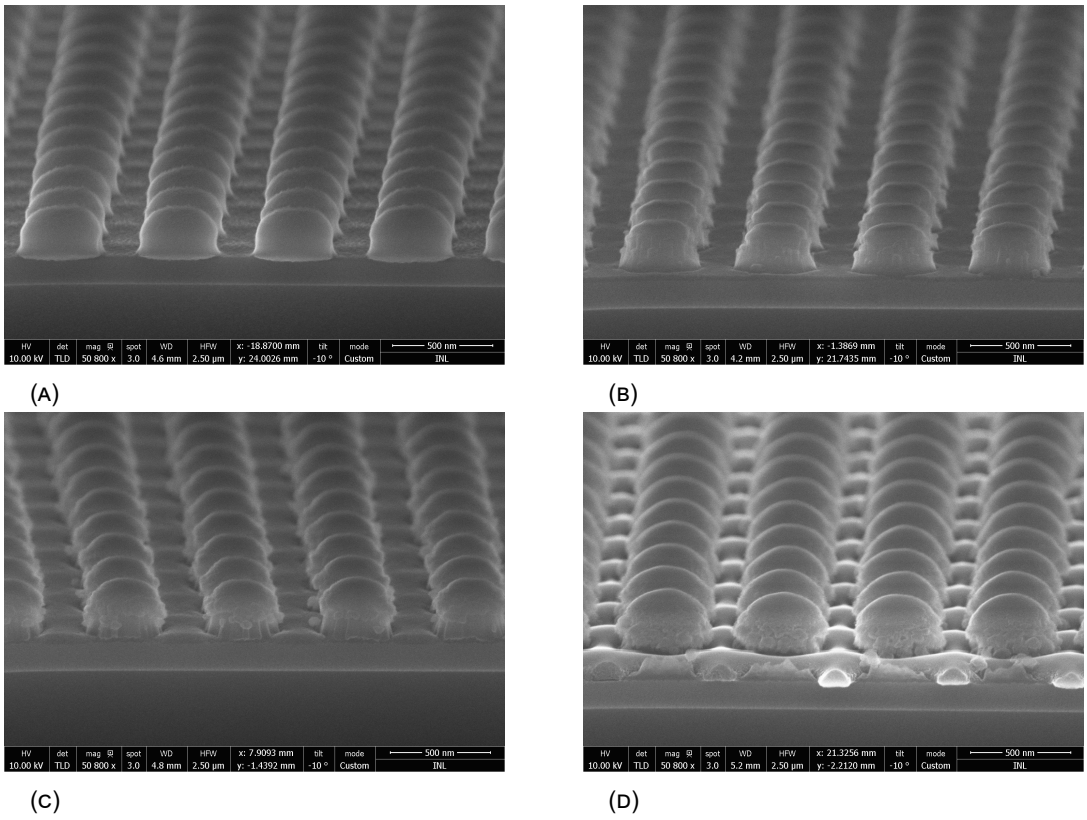


FIGURE 4.5: Representative cross-section SEM images of the SiO_x etch tests using the "Al_2O_3 Etch" recipe from the ICP module in the STPS system. The following etch times were tested: **a)** no etch, **b)** $60\,\mathrm{s}$, **c)** $90\,\mathrm{s}$, **d)** $120\,\mathrm{s}$.

A different module of the SPTS system, C2L, was also tested, with the "SiO_x Etch" recipe. This module allowed the use of CF_4 in a H_2 environment, allowing for a selective and clean etch, good thermal contact and the use of large substrates without bending. This recipe allowed for etch rate values of 163 and $17\,\mathrm{nm\,min^{-1}}$ for SiO_x and resist, respectively. The representative cross-section SEM images of the sample after RR removal and after the different "SiO_x Etch" times (30, 45, and $60\,\mathrm{s}$) can be seen in Fig. 4.6a), b), c), and d), respectively. After $30\,\mathrm{s}$, a thin SiO_x layer remained between the pillars. With $45\,\mathrm{s}$, the layer was fully etched and there was only a small over-etch. The highest time, $60\,\mathrm{s}$, showed a bigger over-etch, but still preserved a good amount of resist on top of the pillars.

This etching process was then tested on a full SS substrate with a Mo back contact. The representative top-view SEM images for the 45 and $60\,\mathrm{s}$ can be seen in Fig. 4.7a), and b), respectively. It is clear that there were no residues or agglomerates in the Mo layer on any of these samples. These were only present in the ICP module samples, which suggests that there was a chemical reaction happening between the surface of the Mo layer and the chemicals used by this module (CF_4). Since a higher concentration of F in plasma favors

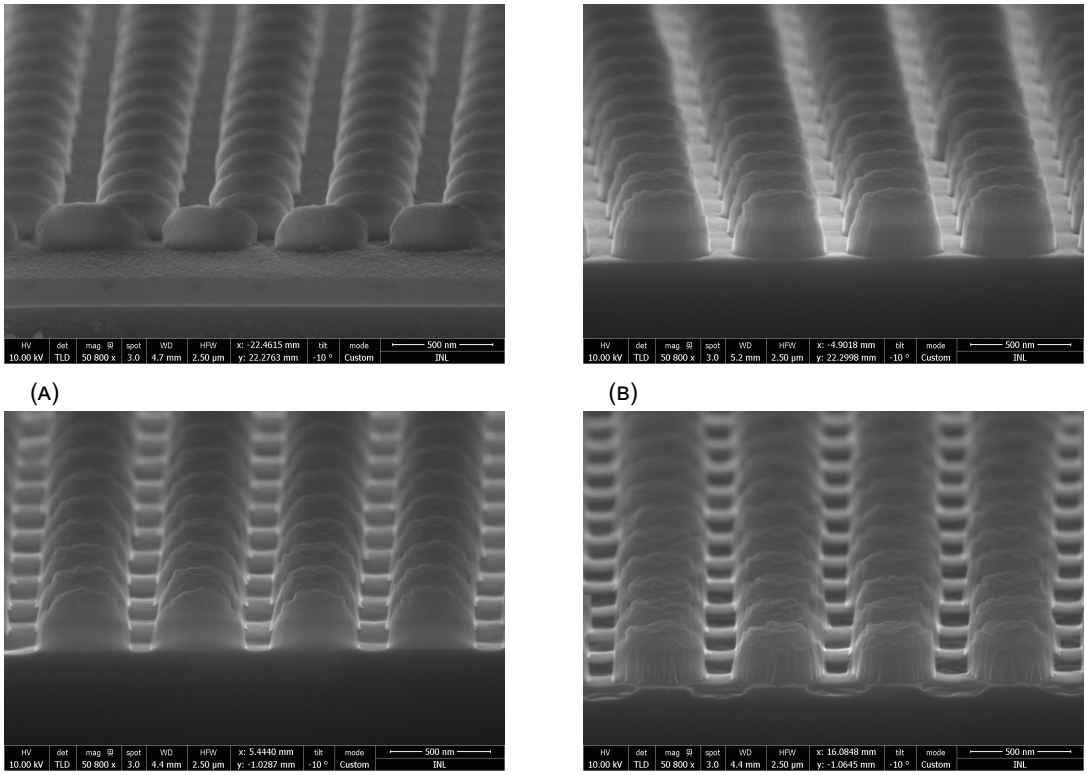


FIGURE 4.6: Representative cross-section SEM images of the SiO_x etch tests using the "SiO_x Etch" recipe. After: **a)** RR removal, **b)** $30\,\mathrm{s}$, **c)** $45\,\mathrm{s}$, and **d)** $60\,\mathrm{s}$ "SiO_x Etch".

the reaction between Na and F, a non-volatile specie composed of Na, F and possibly Mo is formed. Such phenomenon does not happen in the APS or C2L modules because these use an H_2 atmosphere, which reacts with F to form gaseous hydrogen fluoride (HF), reducing the amount of available F in the plasma [98]. It is important to note that the over-etch on Mo is not as severe as in Si. With these results, that were also confirmed by SEM-EDS analysis, both the 45 and $60\,\mathrm{s}$ "SiO_2 Etch" in the C2L module from the SPTS system are able to etch SiO_x effectively on a Mo layer.

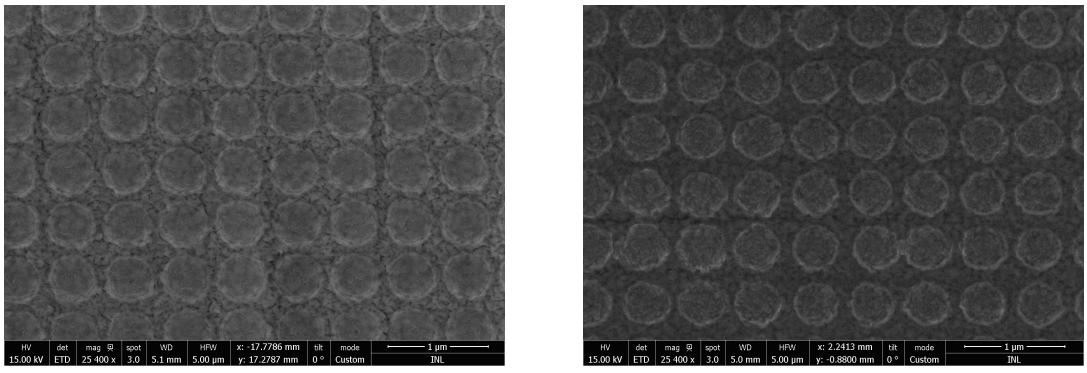


FIGURE 4.7: Representative top-view SEM images of the "SiO_x Etch" etch. After: **a)** $45\,\mathrm{s}$, **b)** $60\,\mathrm{s}$.

4.1.3 Final Resist Strip

The last step of the process flow was to strip the remaining resist off the top of the pillars. When using the APS module for SiO_x etching on $5x5\,cm^2$ SS substrates, the resist is easily removed by MP plasma ashing. However, when using the C2L, complete resist removal is more difficult to achieve. Firstly, a MP plasma ashing cycle (i)) was done, and the following processes were sequentially added: a HP plasma ashing cycle (ii)), $2\,min$ O_2 strip (iii)) and $30\,min$ of Microstrip 3200 (MS3200) at $80\,°C$ with ultrasounds (iv)). The latter is a bulk resist stripper compatible with metals and various other materials, like SiO_x. The test results, obtained by i), i) + ii), i) + ii) + iii), i) + ii) + iii) + iv), can be seen in Fig. 4.8a), b), c), and d), respectively. It can be seen that MP plasma ashing only removes the bulk of the resist (Fig. 4.8a)), while a small residue is left. After adding HP plasma ashing, the results were the same (Fig. 4.8b)). This shows that plasma ashing does not remove anymore resist beyond the bulk. Hence, O_2 strip was used, and the small residue of resist was thinned down (Fig. 4.8c)). To finalize, a MS3200 bath was performed and the results show that the resist was completely removed (Fig. 4.8d)).

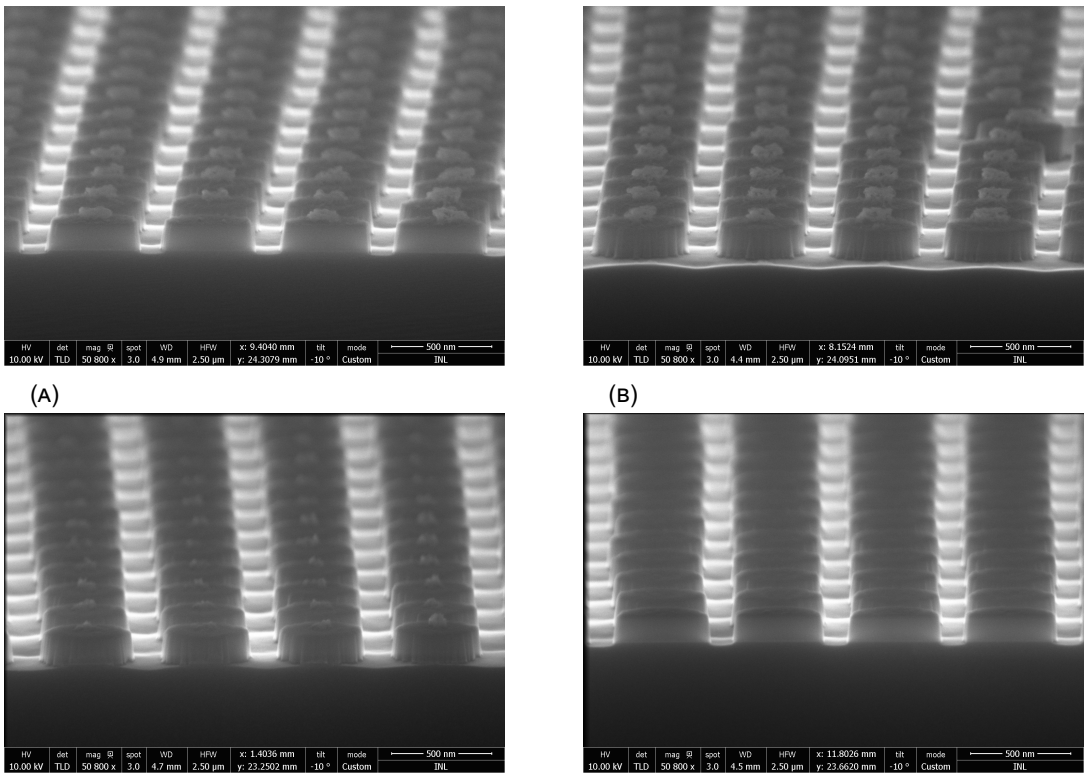


FIGURE 4.8: Representative cross-section SEM images of the resist strip tests. The following sequences were tested: **a)** MP plasma ashing; **b)** MP and HP plasma ashing; **c)** MP and HP plasma ashing and $2\,min$ O_2 strip; **d)** MP and HP plasma ashing, $2\,min$ O_2 strip and $30\,min$ of MS3200 at $80\,°C$.

To first understand the influence of MS3200 on the resist strip, a 2x2 matrix of experiments were performed, including the following variables: MP plasma ashing (yes or no) and MS3200 (ultrasounds or no ultrasounds). The results can be seen in Fig. 4.9a), b), c), and d). From these results it is possible to conclude that MP plasma ashing is crucial in this step, as the MS3200 alone is not capable of fully removing the resist, regardless if ultrasounds are used or not. When using MP plasma ashing, MS3200 only fully removes the resist when using ultrasounds, whereas a static bath appears to have no effect. This suggests that the resist strip is mainly a mechanical rather than a chemical process.

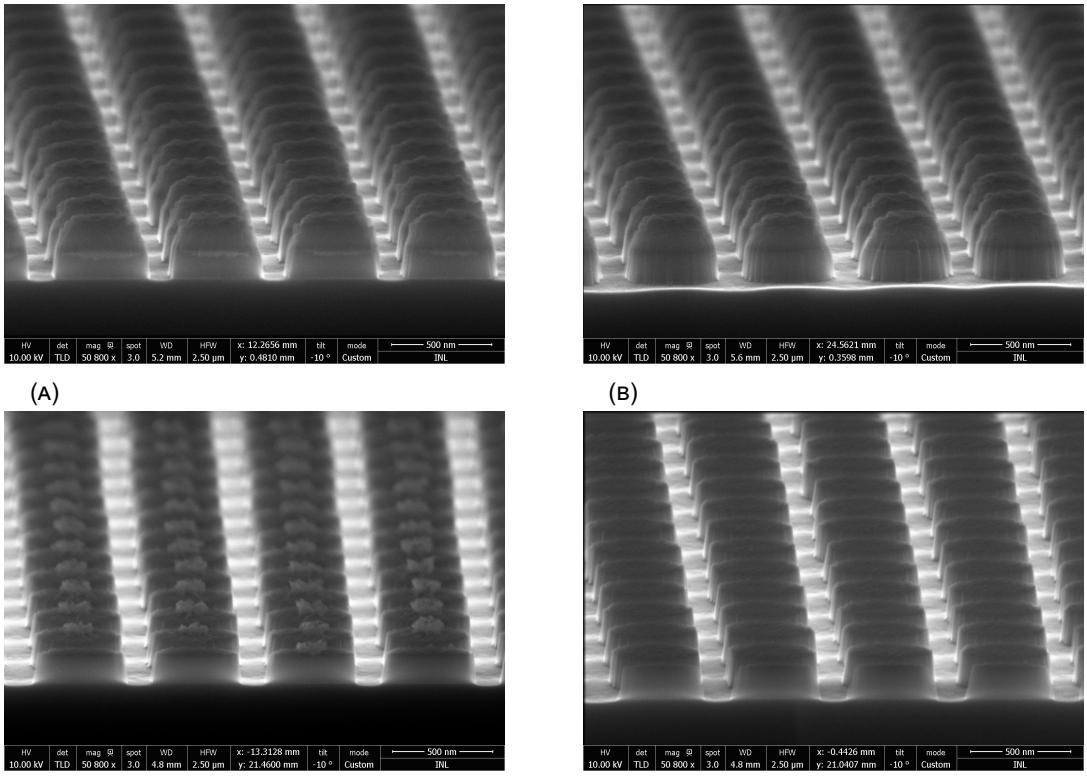
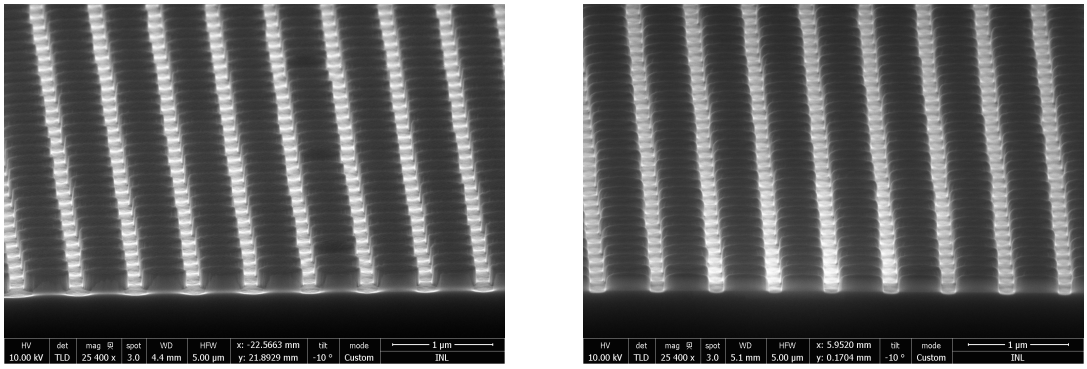


FIGURE 4.9: Representative cross-section SEM images of the resist strip tests matrix. The following tests were performed: **a)** MS3200 without ultrasounds; **b)** MS3200 with ultrasounds; **c)** MP plasma ashing and $30\,\mathrm{min}$ MS3200 without ultrasounds; **d)** MP plasma ashing and $30\,\mathrm{min}$ MS3200 with ultrasounds.

To avoid using a wet process, longer exposure to O_2 strip was tested, since it was observed, in the previous test, that $2\,\mathrm{min}$ O_2 strip reduced significantly the amount of resist after the plasma ashing process. Therefore, $5\,\mathrm{min}$ O_2 strip was tested after MP plasma ashing process, resulting in a full resist strip without affecting pillar morphology.

Two different processes were then established for the full resist strip after the SiO_x etch: i) MP plasma ashing + MS3200 at $80\,^{\circ}\mathrm{C}$ with ultrasounds for $30\,\mathrm{min}$, and ii) MP plasma ashing + $5\,\mathrm{min}$ O_2 strip. Reproducibility tests were then carried out by repeating both

processes three more times. Representative cross-section SEM images of both tests (i, and ii) can be seen in Fig. 4.10a), and b), respectively. Both processes proved to be reproducible, as they show full resist strip without affecting the morphology of the pillars, with equal results between repeated samples. The wet MS3200 process would be favored in an industry environment due to higher throughput and easier automatization. However, for research purposes within INL cleanroom facilities, a wet process would be manual, user-dependent and significantly increase the processing time for each sample. Hence, the dry O_2 strip process was chosen for the samples fabricated herein, due to its shorter processing time and easier processing.



(A) (B)

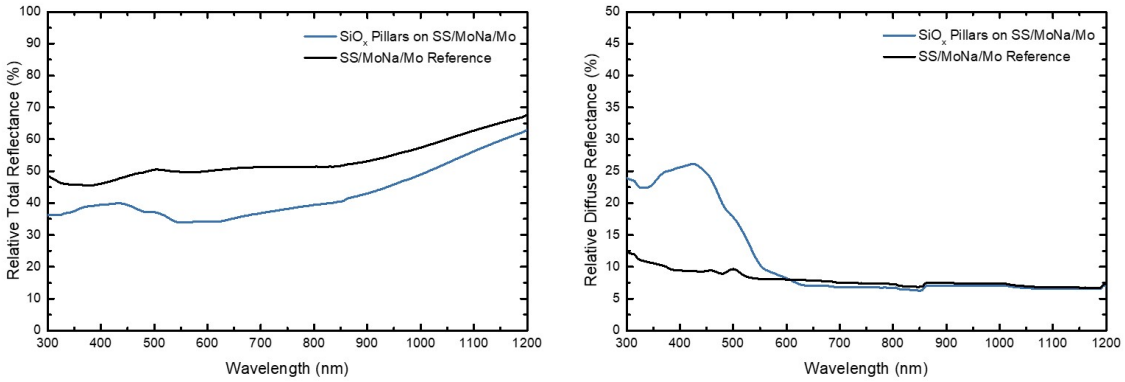
FIGURE 4.10: Representative cross-section SEM images of the resist strip reproducibility tests. The following tests were performed: **a)** plasma ashing and $30\,\mathrm{min}$ of MS3200 with ultrasounds; **b)** plasma ashing and $5\,\mathrm{min}$ O_2 strip.

The optimization of this process flow allowed for reproducible fabrication of SiO_x pillars on a SS/TiW/MoNa/Mo substrate with the scope of integration in ultrathin flexible CIGS solar cells.

4.1.4 Optical Evaluation

UV-Vis-NIR spectrophotometry was employed in order to assess the optical performance of SiO_x pillars on Mo, and compare them with a flat Mo back contact. The comparison results for both the total and diffuse component of reflectance can be seen Fig. 4.11a), and b), respectively. This distinction between components is important, as the total component provides information regarding the overall optical throughput, while the diffuse component is related to light scattering induced by the nanostructures. Regarding the total reflectance component, it is observed that the Mo back contact presents slightly higher reflectance, which is expected since SiO_x has a relatively low n, which leads to an anti-reflection effect. Nonetheless, when evaluating the diffuse component, it is clear that the

scattering abilities of the SiO_x pillars are present. Specially at around $450\,\mathrm{nm}$, a peak is observed, induced by the scattering properties of the nanostructures. Furthermore, there seems to be a cut-off at $550\,\mathrm{nm}$, which corresponds to the nominal pitch of these structures, showing the diffraction effect induced by the array. Moreover, it is important to highlight that these measurements were performed without CIGS deposition, thus the pillars were scattering in a n = 1 surrounding medium. When this pillars reflect in a CIGS surrounding medium, this peak wavelength will raise in value according to the absorber n (3, at $620\,\mathrm{nm}$), corresponding to a wavelength in the NIR region of interest [99].



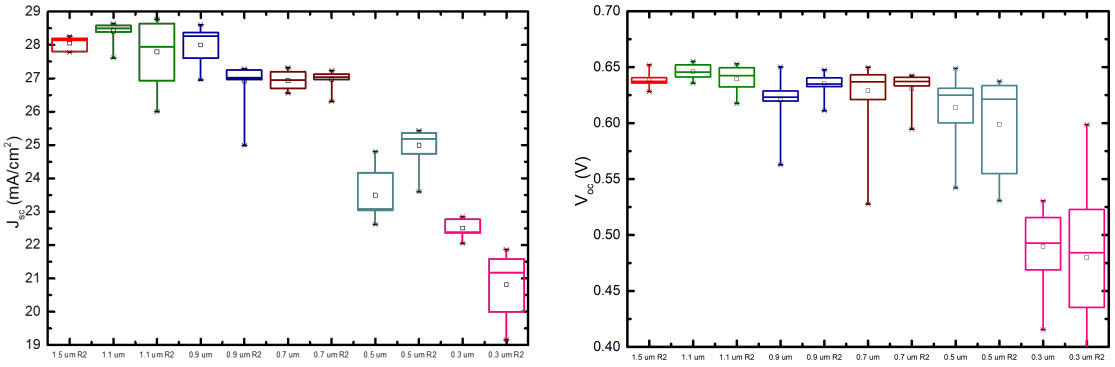
(A) (B)

FIGURE 4.11: Optical performance comparison between SiO_x pillars on Mo and a flat Mo back contact, regarding the following components: **a)** Relative total reflectance; **b)** Relative diffuse reflectance.

4.2. Ultrathin Flexible CIGS Solar Cells

4.2.1 Figures of Merit

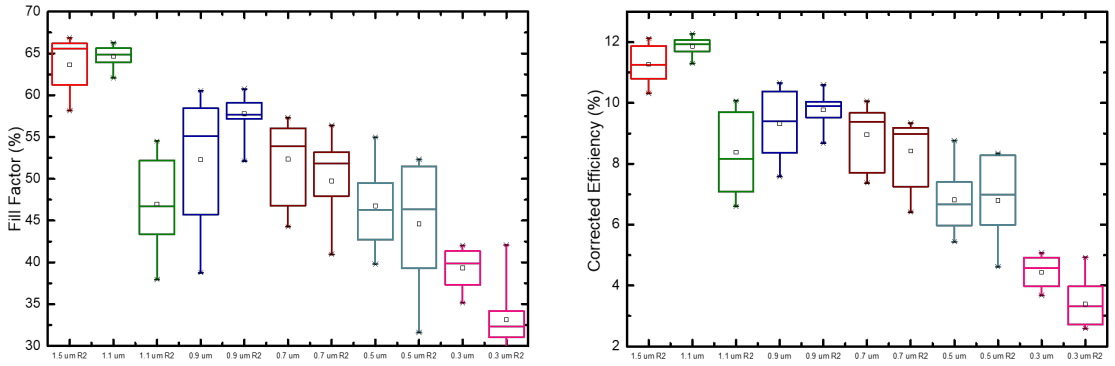
Different thicknesses of the absorber layer were evaluated twice: 1.5 (only once), 1.1, 0.9, 0.7, 0.5 and $0.3\,\mu\mathrm{m}$. In Fig. 4.12a) and b) it is possible to observe the boxplots comparing the J_{sc} and V_{oc} for the different asborber thickness values, respectively. The J_{sc} values follow a descending trend along the decrease of the thickness as expected, since this value reflects how much light is being absorbed by the CIGS layer. A larger drop is noticeable on the 0.5 and $0.3\,\mu\mathrm{m}$ thickness layers. Despite only being measured in the 2^{nd} run, it is worth mentioning that the $1.5\,\mu\mathrm{m}$ cell had a worse absorption than the $1.1\,\mu\mathrm{m}$ cell. The gap between the $1.1\,\mu\mathrm{m}$ cell and the $0.7\,\mu\mathrm{m}$ one was relatively small, which shows that the $0.7\,\mu\mathrm{m}$ thickness still has a good light absorption. For the V_{oc} analysis the values between the 1.5 and the $0.5\,\mu\mathrm{m}$ thickness were similar, which shows that rear recombination was not a limiting factor. However, the $0.3\,\mu\mathrm{m}$ cell presented worse results, as there was a significant drop.



(A) (B)

FIGURE 4.12: **a)** J_{sc} comparison between different thicknesses on both runs; **b)** V_{oc} comparison between different thicknesses on both runs.

Next, both the FF and η of the cell were evaluated, and the results are shown in Fig. 4.13. Analyzing the FF, it is possible to see the same descending trend through the various thickness values, as one would expect. The trend was somewhat linear, with the exception of the $1.1\,\mu m$ cell on the 2^{nd} run, whose FF was much lower than expected. This may be attributed to an error in the inkjet process, where the contact lines were slightly smudged. It is worth noting that the $1.5\,\mu m$ cell had a similar performance to the $1.1\,\mu m$ one. Furthermore, a larger standard deviation was observed in this component, which may be due to the associated error with the scribing procedure. Comparing η, the results were as expected. The same linear trend is observed, with the same exception as in the FF analysis. These results confirm the expected tendency where ultrathin solar cells still present lower efficiencies than it's thin-film counter-parts, with light absorption being the clear limitative parameters.



(A) (B)

FIGURE 4.13: **a)** FF comparison between different thicknesses on both runs; **b)** η comparison between different thicknesses on both runs.

The EQE curves of the cells were also measured. For a better comparison, these curves represent the EQE in the same cell (A2 contact) in every device. These results can be seen in Fig. 4.14. Up until $450\,\mathrm{nm}$, the EQE curves were similar between all absorbers, which is compatible with the fact that only the absorber layer thickness was varied, keeping the top layers of the cell the same. As expected, the absorption spectrum was better for higher thickness values, with $1.1\,\mu\mathrm{m}$ presenting the best results. The results were similar in the range of 1.5 to $0.7\,\mu\mathrm{m}$, in the region below $800\,\mathrm{nm}$. However, for higher wavelengths values, a drop in the absorbance was noticeable in the 0.9 and $0.7\,\mu\mathrm{m}$ curves. As seen in the J_{sc} boxplot, the absorbance of the 0.5 and $0.3\,\mu\mathrm{m}$ cells was clearly lower, as the EQE curve starts to drop in $450\,\mathrm{nm}$.

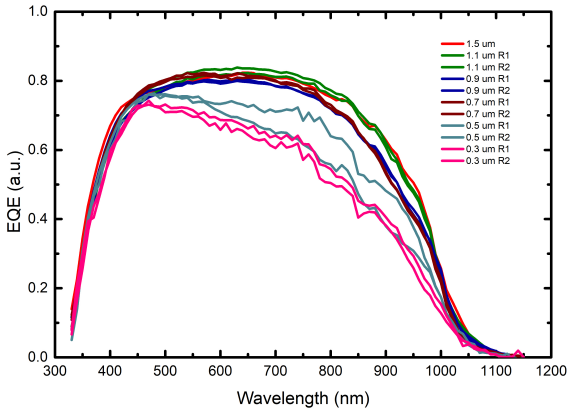


FIGURE 4.14: EQE measurements of the same contact in every cell.

In order to better understand the impact of J_{sc} in the study, the absorber thickness was evaluated using SEM. The results showed a small deviation in regards to the nominal value for all thickness values, with errors ranging from 30 to $70\,\mathrm{nm}$. This, however, is not a significant deviation, and it is not expected to meaningfully influence the absorption of the CIGS layer. Thus, as mentioned before, the J_{sc} behavior can be explained by the descending trend of the absorber thickness.

4.3. Ultrathin Flexible CIGS solar cells with SiO_x pillars

Ultrathin flexible CIGS solar cells with SiO_x pillars were fabricated using 2 different SiO_x etching parameters: 45 and $60\,\mathrm{s}$ on the C2L system. The reference used was a typical $0.5\,\mu\mathrm{m}$ CIGS flexible solar cell where the back contact was deposited on one day and the rest of the device in the following day.

4.3.1 Figures of Merit

The results for the characterization of the studied cells are shown in Fig. 4.15. Starting with the J_{sc} analysis, it is possible to observe that the reference cell presents better results than the cells with light trapping. According to the previously performed optical analysis, the pillars were supposed to enhance light absorption by the solar cell in the NIR region. Nonetheless, these cells presented a loss of about $4\,\mathrm{mA\,cm^{-2}}$, which corresponds to around 16.7%, suggesting that light trapping did not present the desired effect. The same trend can be seen with the V_{oc} analysis, where the reference sample had, once again, the best results. The reference cell presented a V_{oc} of $0.63\,\mathrm{V}$ while the light-management cells obtained $0.54\,\mathrm{V}$, corresponding to a loss of 14.3%. It is worth noting that, in these last two parameters, the performance of the two pillar samples was similar. When analyzing the FF results, it was clear that both the $45\,\mathrm{s}$ etch sample and the reference presented similar results, while the $60\,\mathrm{s}$ etch sample had a 8% deficit in comparison. Finally, the η was obtained, and, as expected by the previous results, the reference cell presented the best η, with 7.65%. The $45\,\mathrm{s}$ etch sample had an η of 5.60%, while the $60\,\mathrm{s}$ only averaged 4.59%. The integration of the SiO_x pillars array in the device lead to a decrease in overall performance of the solar cell. Nevertheless, this must be due to the nanostructures integration in the solar cell processing, rather than the array dimensions.

To better understand if there was an optical gain, the EQE curves were also analyzed, which can be seen in Fig. 4.16. As one can observe, the absorption losses by the pillar samples is located between 400 and $950\,\mathrm{nm}$. This region of the spectrum is responsible for the difference in the J_{sc} values and its the main absorption part in this wavelength range. However, it is very important to note that the absorption between 950 and $1150\,\mathrm{nm}$ is dominated by the pillar samples. This aspect is crucial as it shows that the pillars provided a peak in absorption in this region, located around $1040\,\mathrm{nm}$.

Despite the possible integration problems, the pillar showed a positive impact in the absorption in the NIR region, where the absorption losses by ultrathin solar cells are aggravated. In order to better understand the integration challenges, cross-sectional SEM images were taken from these samples.

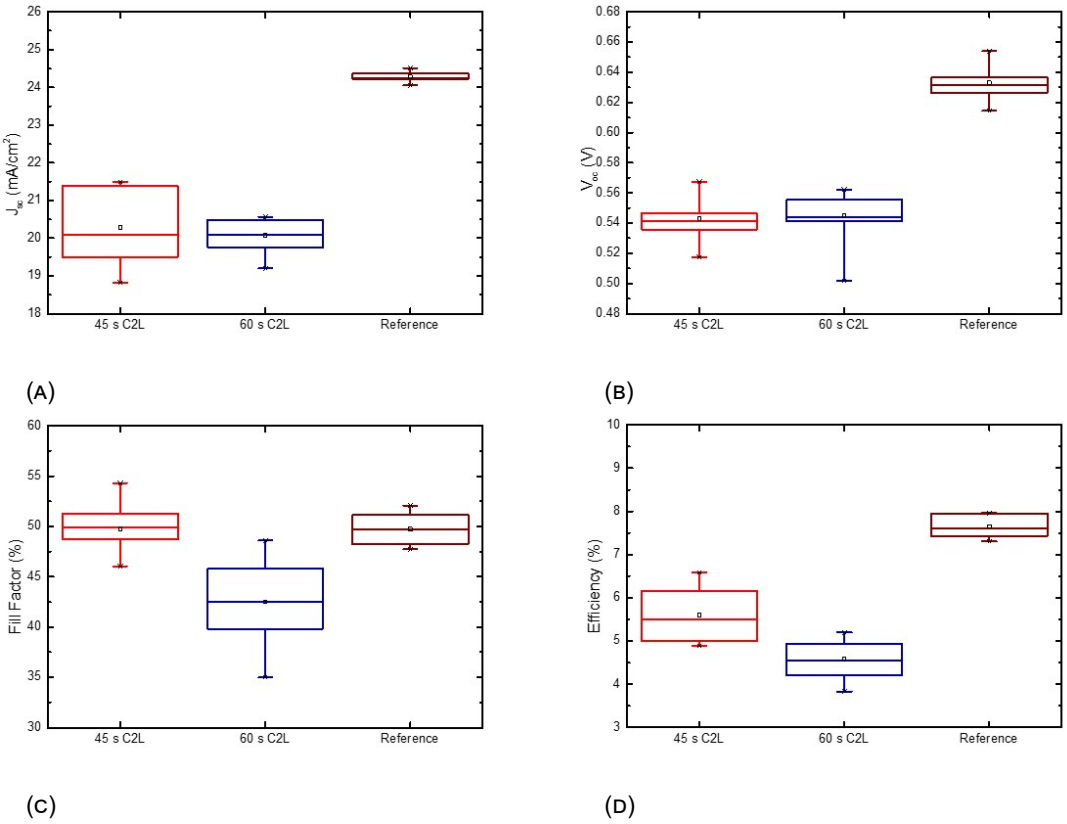


FIGURE 4.15: Comparison of the figures of merit between the $45\,\mathrm{s}$ etch of SiO_x, $60\,\mathrm{s}$ etch of SiO_x and reference sample: **a)** J_{sc}; **b)** V_{oc}; **c)** FF; **d)** η.

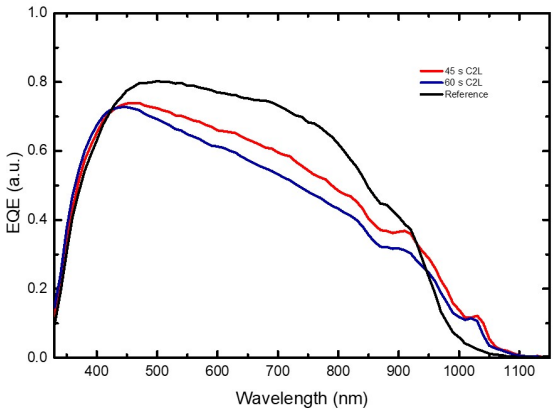
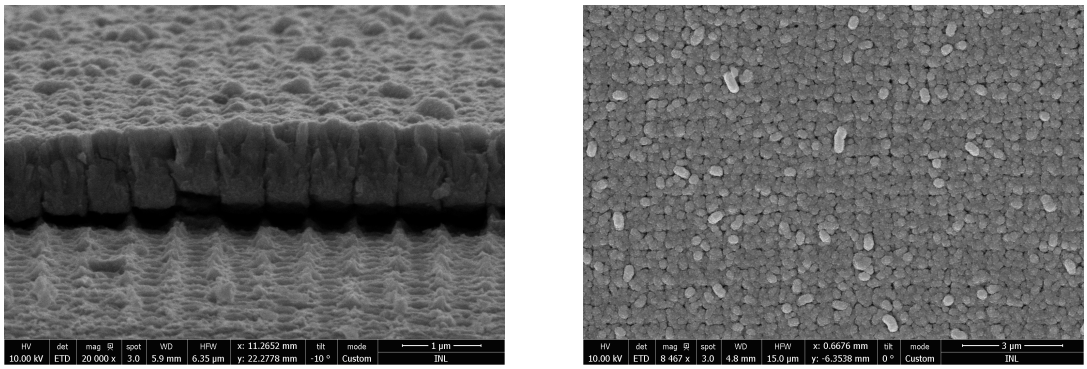


FIGURE 4.16: EQE measurements of the ultrathin CIGS solar cell with SiO_x pillars.

4.3.2 SEM analysis

To better understand the origin of these results, cross-sectional and top-view images of the cells were taken using SEM, and the results can be seen in Fig. 4.17a) and b), respectively. It is clear that all the top layers were divided into columns, due to a disrupted CIGS deposition. This may be one of the reasons why the results were not improved with the presence of these nanostructures. Furthermore, through the SEM top-view image (Fig. 4.17b)), it is possible to confirm this column-like deposition, following the pillar periodicity. Thus, to fully take advantage of the potential optical gains with the SiO_x pillar integration, further studies in relation to CIGS deposition should be performed.



(A) (B)

FIGURE 4.17: Representative SEM images of the ultrathin solar cells with integrated SiO_x pillars: **a)** Cross-section **b)**: Top-View.

4.4. Encapsulated Au Pillars on ITO - Process Flow Optimization

The fabrication of Au pillars (R150 and R100 architectures) encapsulated by dielectric materials required the optimization of several lithographic and etching steps in order to achieve uniform nanostructures with controlled dimensions and minimal surface damage. During the development of the process flow, attention was given to the optimization of RR removal, Au ion milling, dielectric etching, and final cleaning procedures, since these steps strongly influence the morphology and optical response of the fabricated structures, which directly impacts the performance of the solar cell. Similarly to the process flow for the fabrication of SiO_x pillars, the optimization procedure was carried out by varying individual process parameters and evaluating their impact through SEM and AFM characterization. The main optimization criteria included pillar dimensional accuracy, minimization of redeposition effects, reduction of over-etching, preservation of the dielectric encapsulation, and overall pattern uniformity.

4.4.1 Pillars RR strip

After a 50 or $60\,\mathrm{nm}$ Au deposition on the SLG/ITO substrate, a layer of resist was spin-coated. The pillar master stamp architeture was then imprinted on the resist and the RR layer had to be removed, which was done by O_2 strip. Various O_2 strip times were tested for both R150 and R100 architectures. For each architecture the ecthing time was chosen considering full RR removal and minimal damage to the resist pillar morphology. The chosen O_2 strip times were 6 and $12\,\mathrm{s}$ for R150 and R100, respectively. The representative cross-section SEM images of R150 and R100 samples after imprint, and R150 and R100 after RR removal, can be seen in Fig. 4.18a), b), c) and d), respectively. After R150 imprint, a RR layer was present (around $20\,\mathrm{nm}$), as seen in Fig. 4.18a), which was completely removed by $6\,\mathrm{s}$ O_2 strip (Fig. 4.18c)). For R100, the RR layer was slightly thicker (around $40\,\mathrm{nm}$), as seen in Fig. 4.18b), and was completely removed by $12\,\mathrm{s}$ O_2 strip (Fig. 4.18d)).

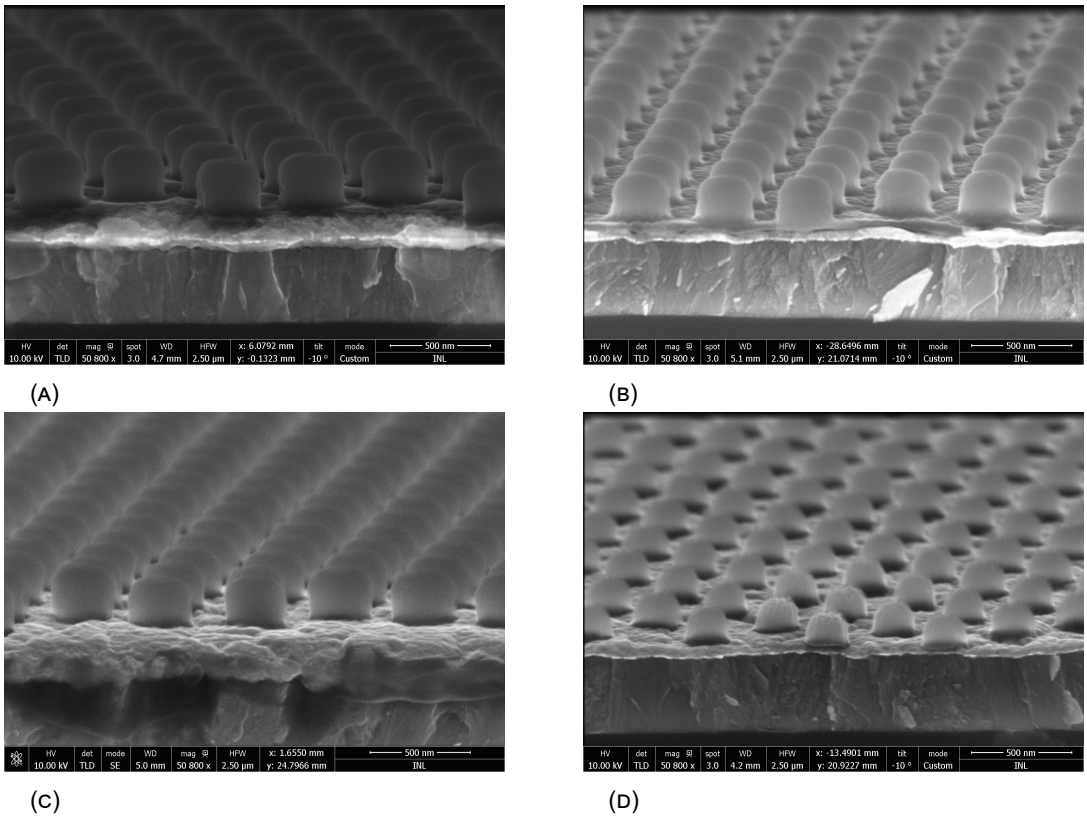


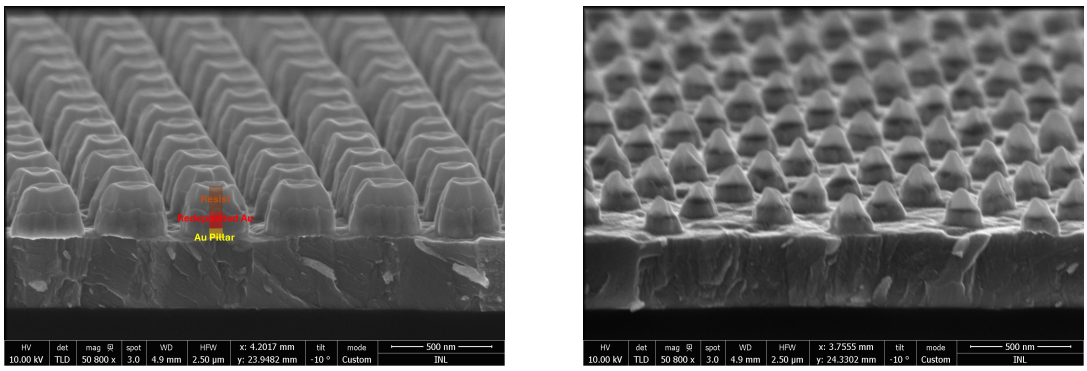
FIGURE 4.18: Representative cross-section SEM images of the RR removal tests. **a)** R150 after imprint; **b)** R100 after imprint; **c)** R150 after 6 s O_2 strip; **c)** R100 after $12\,\mathrm{s}$ O_2 strip.

4.4.2 Au Etch

After complete removal of the RR layer, Au etch was carried out by ion milling using the Nordiko system. An initial set of experiments was conducted to investigate the effect of

the milling angle on the etching process. At the time of these experiments, both R150 and R100 master stamps had not yet been fabricated. Hence, these experiments (not shown) were carried out using a slightly different pillars architecture (r = 100 nm, a = 350 nm, and h = 50 nm). Milling angles ranging from 90 to 130° were studied. It was observed that normal incident angles resulted in a cone-like morphology, while a 130° angle resulted in an aggressive etching on the pillars' sidewall, leading to a volcano-like shape. Given these results, it was concluded that the 110° angle yielded the best cylindrical-like morphology.

This IBE process was then transferred to both R150 and R100 architectures, for which a similar morphology was achieved. Fig. 4.19a) and b), show the representative cross-section SEM images for both R150 and R100 architectures after a 110° IBE, respectively. As seen in both images, a major challenge that arose in this step was the presence of material redeposition after ion milling.



(A) (B)

FIGURE 4.19: Representative cross-section SEM images of Au pillars on ITO after a 110° IBE process for architectures: **a)** R150; **b)** R100.

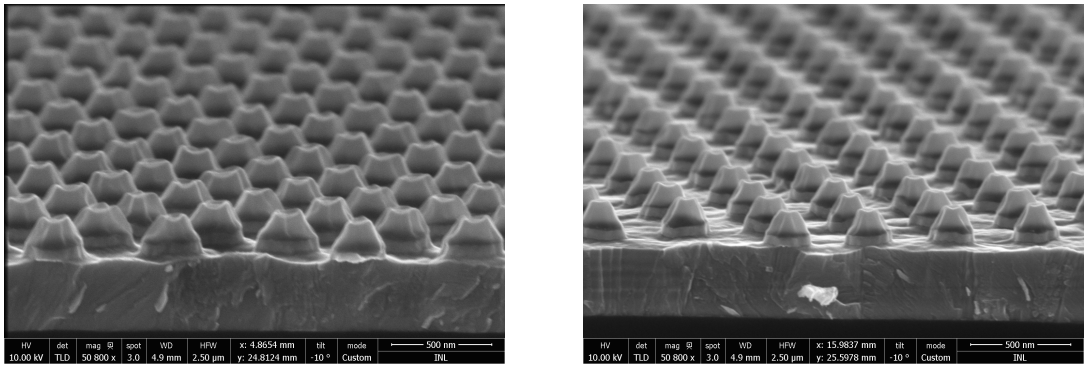
Initially, these upper regions were presumed to consist mainly of hardened resist residues. The resolution and imaging conditions of the SEM were insufficient to clearly distinguish the metallic pillar body from the upper region. Consequently, EDS analysis could not be used to identify the atomic nature of these features, since the measurement would include the underlying Au pillar, leading to a strong Au signal regardless of whether the upper material consisted of resist or redeposited Au. This prevented the unambiguous identification of the material coating during the initial stages of process optimization.

Based on this initial interpretation of hard resist on top of the Au pillars, extensive post-etch studies were conducted to remove the resist residues. Several stripping and cleaning approaches, as well as combinations thereof, were investigated. This included dry O_2 strip and plasma ashing processes, as well as wet approaches based on solvent-based

removers. The latter were based on different chemistries, such as ethanol and hydroxylamine (EKC265), dimethyl sulfoxide (MS3200 and MS3001), and 1-ethylpyrrolidin-2-one (mr-REM500), as well as combinations of thermal treatment and ultrasound-assisted cleaning. Different plasma ashing recipes, bath immersion times, temperatures, and ultrasound conditions, were systematically tested in order to evaluate their effectiveness in removing the material while preserving the integrity of the Au nanostructures. Ultimately, the persistence of these features, together with evidence reported in the literature, indicated that the observed material originated from Au redeposition during the IBE process rather than from residual resist [100, 101].

To address this issue, a multi-angle ion milling strategy was implemented. The initial etching step was performed at $110°$. Different milling angles were subsequently investigated to optimize the removal of redeposited Au. A grazing angle ($165°$) was introduced aiming to etch the redeposited material around the side walls of the structure. For the R150 architecture, due to the tight spacing, this grazing angle showed not to be enough. Therefore, additional angles were introduced prior to the grazing, such as $90°$ and $130°$. The $90°$ etch presented material redeposition and significant ITO over-etch, and was therefore avoided. Conversely, the $130°$ angle was very effective at directly etching the sidewalls, thus removing most of the redeposited Au. Nonetheless, when using longer times, the excessive sidewall etching caused a decrease in the pillars r, away from target dimensions. For this reason, this step was limited to a $120\,\mathrm{s}$ duration. The grazing angle was then employed varying the etching time to finalize the redeposited Au removal. Due to the tight spacing, shading effects take place when using a planar etching angle, thus drastically reducing the etch rate. Therefore, it was observed that even for longer etching times, neither the ITO or the sidewalls of the pillars suffered over-etch, allowing for a fine control of the removal of the redeposited Au in this step. After optimization, $900\,\mathrm{s}$ was chosen for the etching time at this angle. Overall, the IBE angle of $130°$ for $120\,\mathrm{s}$, followed by $165°$ for $900\,\mathrm{s}$, completely removed the redeposited Au for the R150 architecture without compromising the pillar morphology, as shown in Fig. 4.20a). For the R100 architecture, a similar approach was employed. However, this architecture has a significantly larger spacing than the R150, resulting in an excessive sidewall etching when using the same IBE angle combination. Therefore, from new optimization tests, it was observed that a single etching step at $165°$ for $240\,\mathrm{s}$ was enough to fully remove the redeposited Au in this architecture, as shown in Fig. 4.20b).

Reproducible IBE processes were thereby established, ensuring the desired cylindrical



(A) (B)

FIGURE 4.20: Representative cross-section SEM images of Au pillars in ITO after the $110°$ (540 s) IBE, followed by: **a)** $130°$ (120 s) followed by $165°$ (900 s), R150 architecture; **b)** $165°$ (240 s), R100 architecture.

morphology while completely removing redeposited Au residues. The undermentioned IBE processes were used for the following architectures: R150 - intermittent $110°$ etch ($540\,\mathrm{s}$), followed by a continuous $130°$ etch during $120\,\mathrm{s}$, and a continuous $165°$ etch for $900\,\mathrm{s}$; R100 - intermittent $110°$ etch ($540\,\mathrm{s}$), followed by a continuous $165°$ etch during $240\,\mathrm{s}$.

4.4.3 Au Resist Strip

To finalize the Au pillars, the resist strip after the Au etch had to be optimized. Different resist strip tests were carried out, highlighting $30\,\mathrm{min}$ of MS3200 at $80\,^{\circ}\mathrm{C}$ with ultrasounds (presented in 2 different magnifications), 3 cycles of LP plasma ashing, and 3 cycles of HP plasma ashing + $2\,\mathrm{min}$ of O_2 strip, with the results being displayed in Fig. 4.21a), b), c), and d), respectively. Despite MS3200 being effective at removing the resist, as shown in Fig. 4.21a), some patches of Au pillars were removed from the sample, as observed with lower magnification SEM images (Fig. 4.21b)). This may be from the ultrasonic agitation, causing high mechanincal stress, thus deeming the process unreliable. With the 3 cycles of LP plasma ashing, the resist was majorly removed, but there is still the presence of small residues (Fig. 4.21c)). On the other hand, the 3 cycles of HP plasma ashing + $2\,\mathrm{min}$ O_2 strip fully removed the resist and retained the integrity of the pillars (Fig. 4.21d)). Hence, this process was chosen for this step.

4.4.4 RR removal from Contact Openings Imprint

The Au pillars were encapsulated with different dielectric materials (SiO_x, TiO_2, and Al_2O_3) and thickness values (10, 20, and $40\,\mathrm{nm}$), depending on the series. A layer of resist was then spin-coated on the dielectric-encapsulated architecture and, after undergoing the

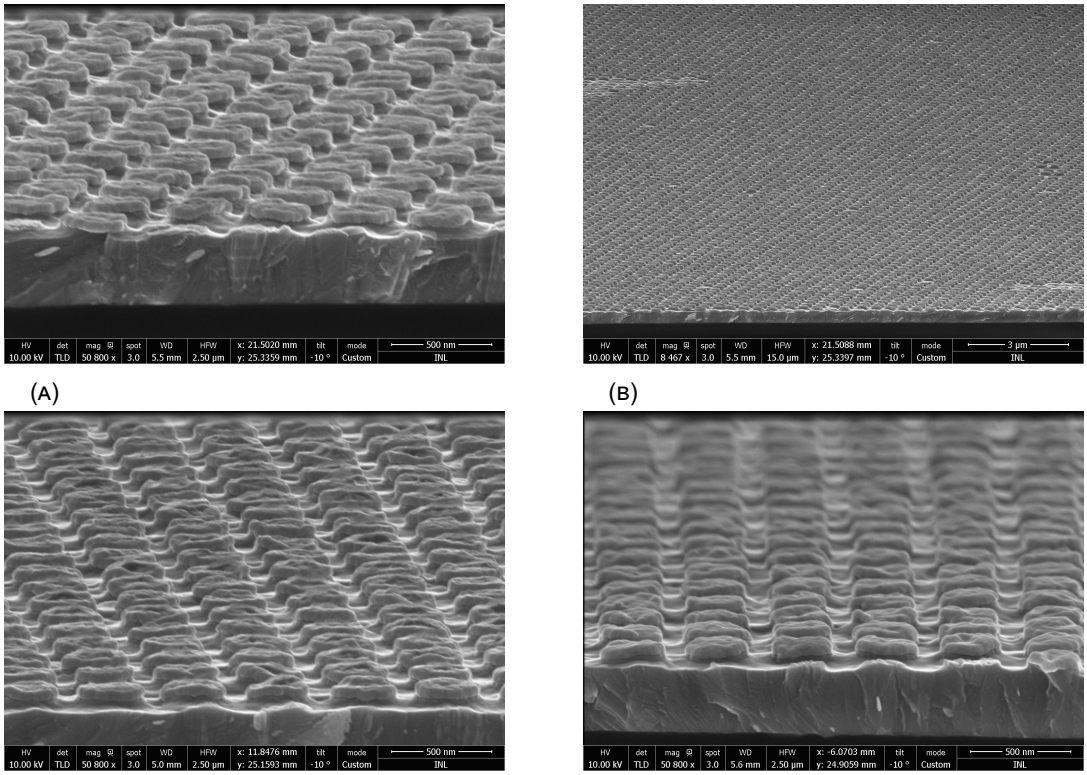


FIGURE 4.21: Representative cross-section SEM images of the resist strip tests after the Au etch. The following processes were tested: **a)** MS3200 at $80\,^{\circ}\mathrm{C}$ with ultrasounds with a magnification of 50800x and **b)** 8467x; **c)** 3 cycles of LP plasma ashing; **d)** 3 cycles of HP plasma ashing + $2\,\mathrm{min}$ of O_2 strip.

lines/holes pattern imprint, the RR layer was removed by $12\,\mathrm{s}$ O_2 strip. The representative cross-section SEM images were taken for the lines samples, showing the RR layer (Fig. 4.22a)), and its full removal (Fig. 4.22b)), completely exposing the underlying encapsulated pillar scheme.

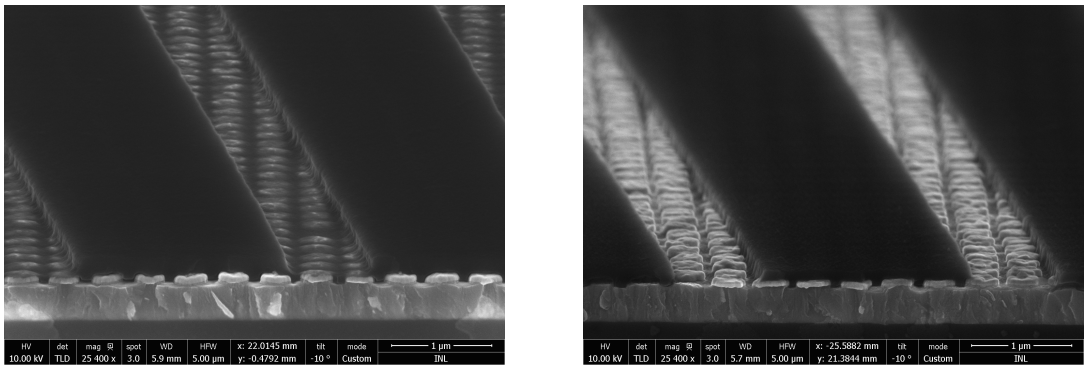
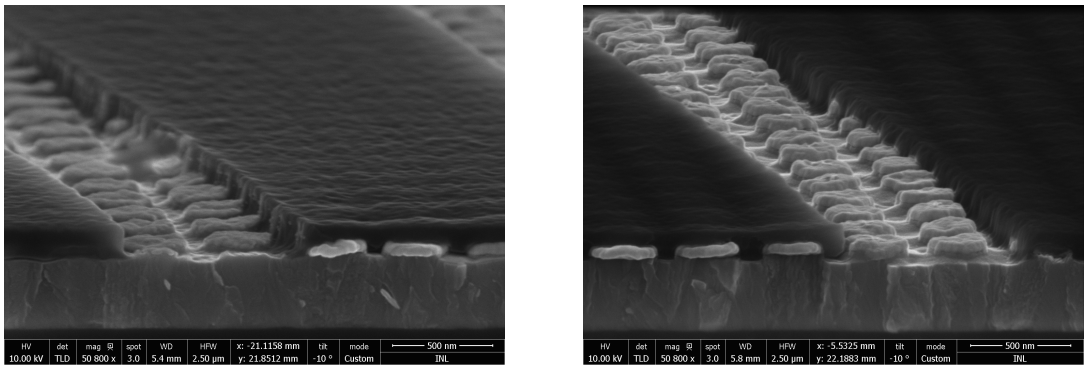


FIGURE 4.22: Representative cross-section SEM images of the SiO_x lines sample: **a)** After imprint; **b)** After $12\,\mathrm{s}$ O_2 strip.

4.4.5 Dielectric etch

To etch the dielectric layer after the RR removal, two systems were tested to etch the SiO_x: IBE and RIE ("Slow SiO_x Etch"), for which representative cross-section SEM images are shown in Fig. 4.23a) and b), respectively. The etch was successful in both cases since the dielectric layer was fully removed in the uncovered regions and the resist was still unaltered. IBE presented a slight ITO and Au over-etch, severely affecting the exposed pillar morphology (Fig. 4.23a)). However, this is not problematic as these exposed Au pillars will be removed in the next process flow step. On the other hand, although RIE also fully removed the dielectric layer (Fig. 4.23b)), Au exposure to the RIE process should be avoided, as Au does not react to create volatile compounds with the etch gases. Au is only physically removed by the accelerated ions, contaminating the chamber of the tool as no volatile components are formed. Another relevant difference is the versatility in each system. RIE relies on chemical reactions between the plasma and the material being etched, requiring recipe adjustments, mainly regarding plasma chemistry, depending on the dielectric. In contrast, IBE is a pure physical process, relying on sputtering of the to-be-etched material, hence being inherently non-selective. This implies that the same etching conditions can be used across different dielectric materials. Therefore, $130°$ IBE was selected for the dielectric etching across the different fabricated series.



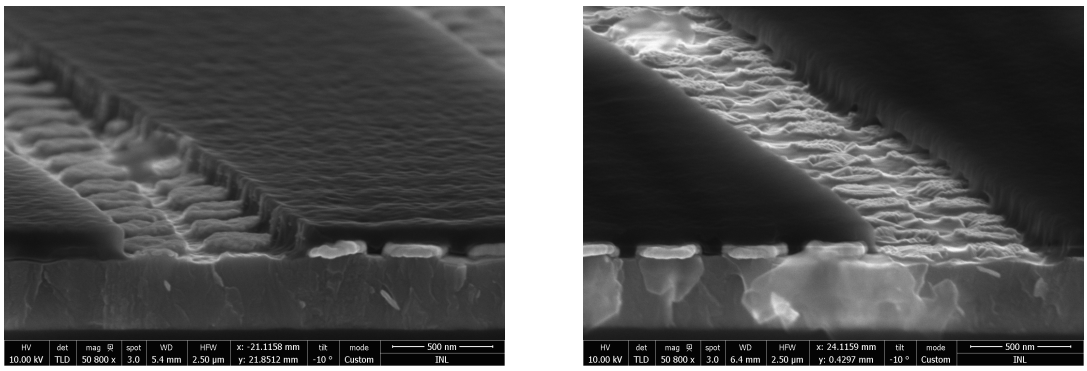
(A) (B)

FIGURE 4.23: Representative cross-section SEM images of encapsulated Au pillars after SiO_x etch by: **a)** IBE; **b)** RIE.

4.4.6 Exposed Au Wet Etch

In order for Au not to diffuse into the CIGS layer, it is imperative that the non-encapsulated pillars be removed. Since some pillars will be partially covered by the dielectric, an isotropic etch is needed to ensure no amount of Au is left exposed. Hence, a wet etching is preferable to the anisotropic nature of dry etching processes. For this reason, the

Technietch ACI2 Au etchant was used. The representative cross-section SEM images of the encapsulated Au pillars before and after immersion in Technietch ACI2, can be seen in Fig. 4.24a) and b), respectively. From the results, it is possible to observe that all the uncovered Au was removed, even the pillars that were previously partially exposed, ensuring no Au will be in contact with the absorber layer. All the pillars that were completely encapsulated by the dielectric material remain intact. Roughness on the ITO layer is observed, following the scheme of the removed Au pillars. These present a pillar-like morphology, resulting from the ITO over-etch due to the ion milling processes of Au and dielectric etch. However, this is not expected to alter the electrical properties of the ITO, as the over-etch is purely physical.

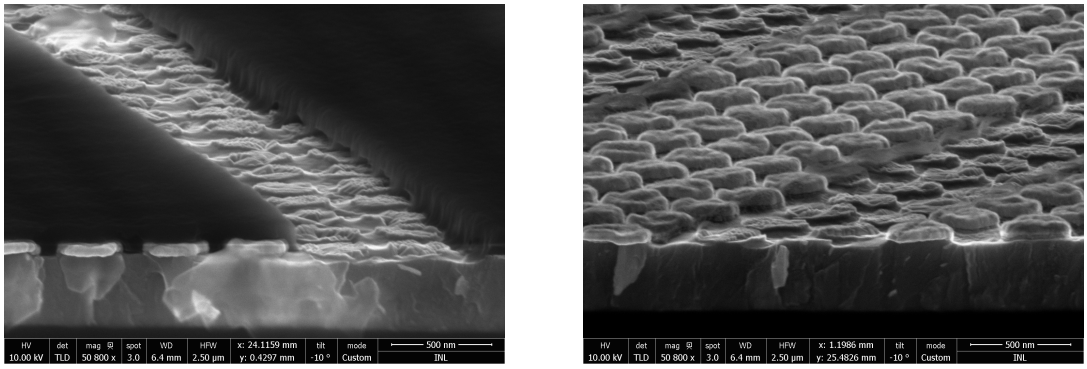


(A) (B)

FIGURE 4.24: Representative cross-section SEM images of the encapsulated Au pillars: **a)** Before immersion in Technietch ACI2; **b)** After immersion in Technietch ACI2.

4.4.7 Final Resist Strip

After etching the exposed Au pillars, any remaining resist must be removed. For that purpose, 3 cycles of LP plasma ashing were performed, since this recipe was already used for other processes within the group. The representative cross-section SEM images of the encapsulated Au pillars before and after 3 cycles of LP plasma ashing, can be seen in Fig. 4.25a) and b), respectively. As it is possible to observe, all the remaining resist was removed without damaging the pillars. Due to this reason, this process was chosen for the remaining fabrication of the series.



(A) (B)

FIGURE 4.25: Representative cross-section SEM images of the encapsulated Au pillars: **a)** Before 3 cycles of LP plasma ashing; **b)** After 3 cycles of LP plasma ashing.

4.5. Au Pillars on ITO Characterization

4.5.1 SEM Analysis

SEM images were taken for all the samples in the 3 series. Fig. 4.26a) and b), show representative top-view SEM images of a sample from series A with Al_2O_3 encapsulation lines, while the holes contact openings are shown in Fig. 4.26c), and d). Examples of the pillar diameter and opening features measurements taken from these images are marked with yellow lines. It is possible to observe distinctively the Au pillar and the encapsulation layer, which was also observed in the TiO_2 passivation samples. Nonetheless, the same could not be said for the SiO_x ones, as the passivation was barely visible, influencing the measurements. This could be due to the different nature of PECVD and ALD techniques. While ALD ensures a conformal deposition by layer growth on the sidewalls of the pillars, PECVD has a much less controlled deposition, which may result in rounded corners from different deposition rates on the sidewalls and on top of the pillars. For the R150 architecture, the Au pillars presented a diameter of $(273 \pm 13)\ \mathrm{nm}$, which corresponds to a 9.0 % error from the nominal value. For R100, a diameter of $(205 \pm 12)\ \mathrm{nm}$ was measured, corresponding to a 5.1 % error. Regarding the contact opening features, the unpassivated width in the lines scheme is $(810 \pm 18)\ \mathrm{nm}$, while for the holes, the radius of the openings presented a value of $(224 \pm 7)\ \mathrm{nm}$. This corresponds to a passivation surface coverage of 71 % and 94 %, for the lines and holes scheme, respectively. Furthermore, as can also be seen in the images from both contact opening architectures, any slightly exposed pillar was removed by Technietch ACI2, confirming the effectiveness of the wet etch process.

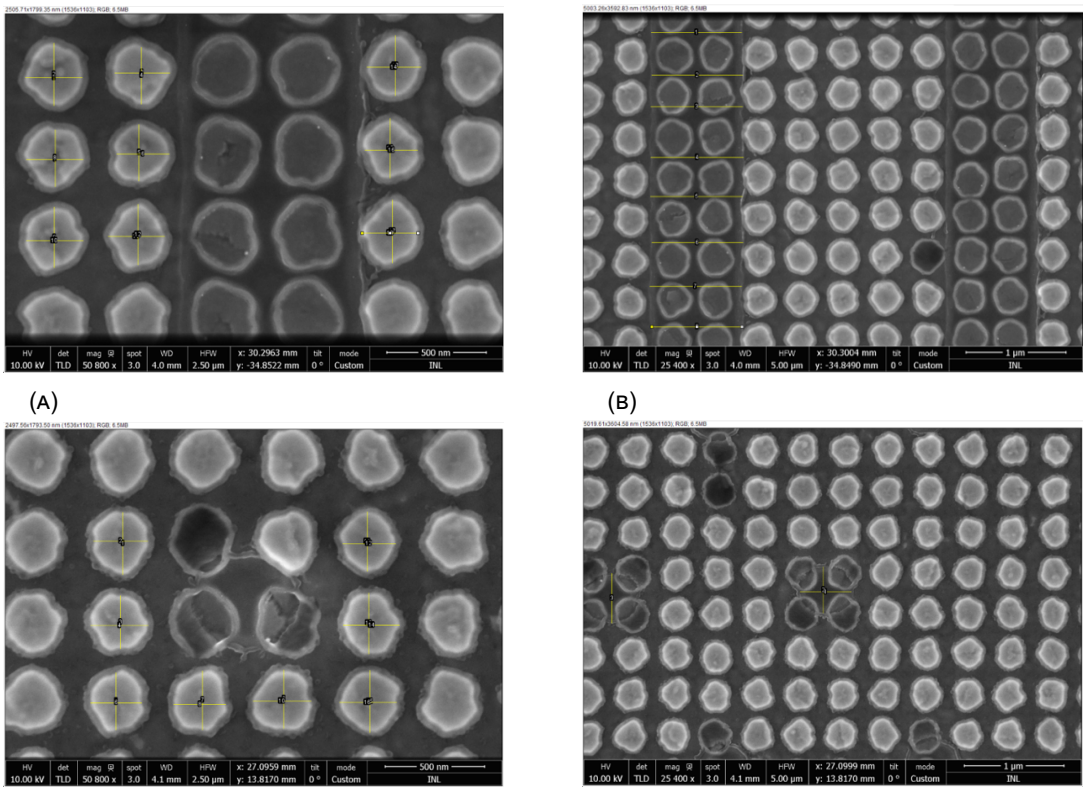
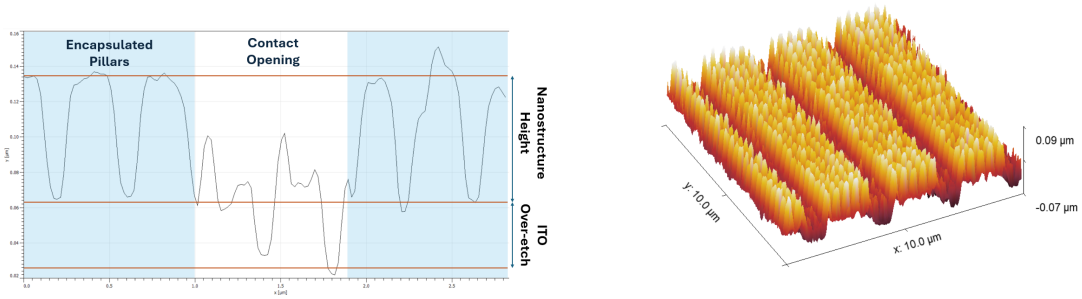


FIGURE 4.26: Representative top-view SEM images of Al_2O_3 passivated samples from the series A, with **a)** and **b** lines passivation scheme, **c)** and **d)** holes passivation scheme. The measurements are represented by yellow lines.

4.5.2 AFM Analysis

AFM measurements were analyzed for all the pillars in the 3 series. Fig. 4.27a), and b), show an AFM line scan and the measured 3D profile, respectively, of a SiO_x encapsulated sample from series B with the lines scheme. Regarding the encapsulated pillar height, the A series presented an average value of $(71.0 \pm 7)\,\mathrm{nm}$, while for the B series, a result of $(73.0 \pm 5)\,\mathrm{nm}$ was obtained. For the C series, the values had to be distinguished because of the different passivation thickness. Heights of (67.9 ± 1.6, 72.1 ± 0.6, and 77.1 ± 1.1) nm were obtained for passivations of 10, 20 and $40\,\mathrm{nm}$, respectively. These values should coincide with the sum of the Au pillar h and the encapsulation thickness. Even though some measurements are according to the target dimensions, some were measured slightly below. Such can be attributed to a Au deposition deviation associated with the tool, and measurements errors induced by the high roughness of the ITO layer (root mean square = $13\,\mathrm{nm}$). Another feature whose measurement is enabled by AFM, is the amount of over-etch of the ITO layer. Across all samples, a value of around $40\,\mathrm{nm}$ was measured for this feature, which is associated with both Au and dielectric ion milling. Even

though this over-etch is a non-desired result from the fabrication process, and should be minimized, it is not expected to impact the optoeletronic performance of the solar cell, as the electrical properties of the ITO should not be affected by a purely physical etch.

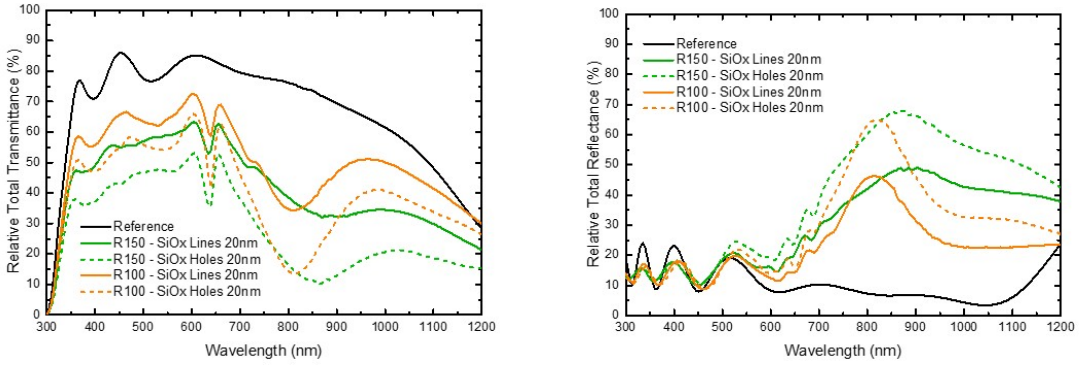


(A) (B)

FIGURE 4.27: AFM analysis of a SiO_x encapsulated sample from series B with the lines scheme: **a)** Line scan, **b)** 3D profile.

4.5.3 UV-Vis-NIR Spectrophotometry Analysis

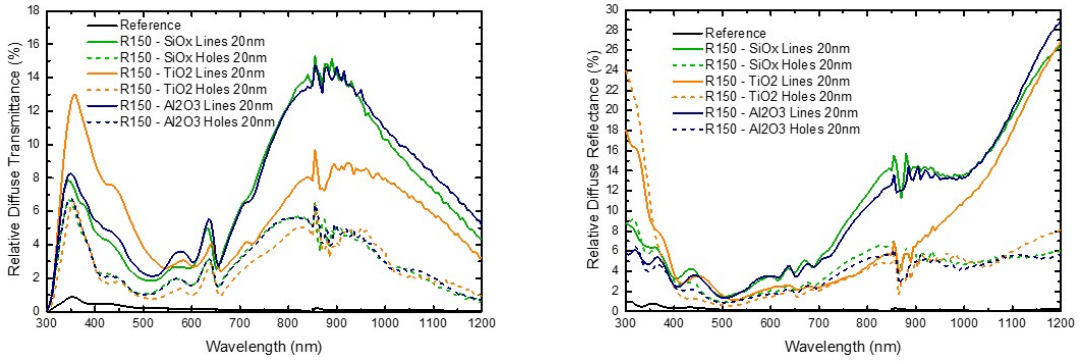
The UV-Vis-NIR analysis was performed in order to assess the bifacial and scattering capabilities of the samples. The total and diffuse components of both the transmittance and reflectance were measured. With the total component, it is possible to observe if the samples provide a bifacial configuration. With the diffuse component, it is possible to understand how much light is scattered and in which regions of the spectrum. The results will be displayed sequentially, starting with the total transmittance and reflectance comparison between series A and B, and the results can be seen in Fig. 4.28a) and b), respectively. Analyzing the relative total transmittance, it is possible to observe that the reference allows more transmission of light to the cell when illuminated from the rear. This is expected, since in the pillars samples these nanostructures reflect a portion of the light when the cell is illuminated from the rear contact. Nonetheless, it is clear that the pillars from series B, which is optimized for a bifacial configuration, absorb, reflect, and loose less light when rear-illuminated. Regarding the relative total reflectance, the reference clearly reflected less light than the pillars samples. As predicted, the A series, which is optimized for front illumination, presents better reflectance than the B series sample. It is important to note that the holes passivation presented much better results in this component. Since the total reflectance is related to reflection and not scattering, it is normal that the holes have better results since the its passivation area is larger, which translates to a much higher number of metallic nanostructures reflecting the light.



(A) (B)

FIGURE 4.28: Comparison between series A and B regarding the following components: **a)** Relative total transmittance, and **b)** Relative total reflectance.

The results for diffuse transmittance and reflectance components from the A series can be seen in Fig. 4.29a) and b), respectively. As one can observe, the pillar architecture has an impact in the scattering abilities of the back contact, which can clearly be seen when comparing the results to the reference. In both cases the lines passivation presented more scattering than the holes. This result is interesting since the holes passivation area is larger. However, one possible reason for the observed effect could be the ion milling processes (Au and dielectric etch). Since the area to be etched is much larger on the lines, these are more prone to over-etch the ITO layer. This over-etch introduces roughness in the layer and, consequently, ITO pillars, inducing additional scattering in the sample. Comparing the materials, TiO_2 presented lower scattering in wavelengths higher than $500\,\mathrm{nm}$. Both Al_2O_3 and SiO_x presented similar curves throughout the analyzed spectrum.

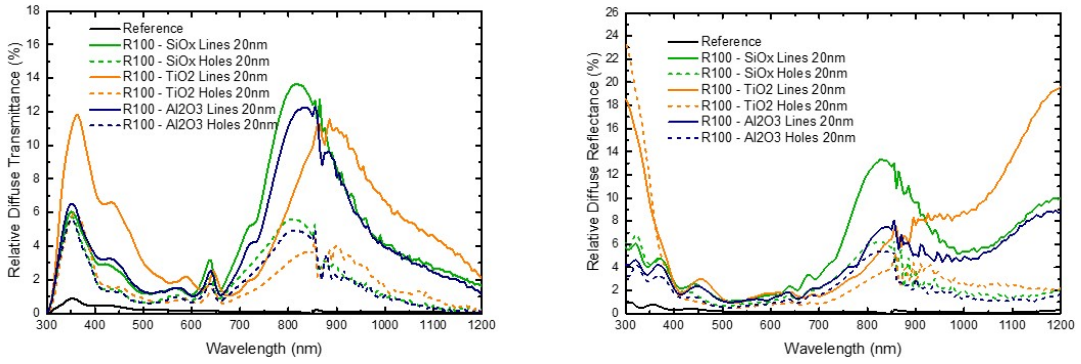


(A) (B)

FIGURE 4.29: **a)** Relative diffuse transmittance spectra from the A series samples, and **b)** Relative diffuse reflectance spectra from the A series samples.

Next, the diffuse transmittance and reflectance components from the B series were analyzed and the results can be seen in Fig. 4.30a) and b), respectively. Once again, the

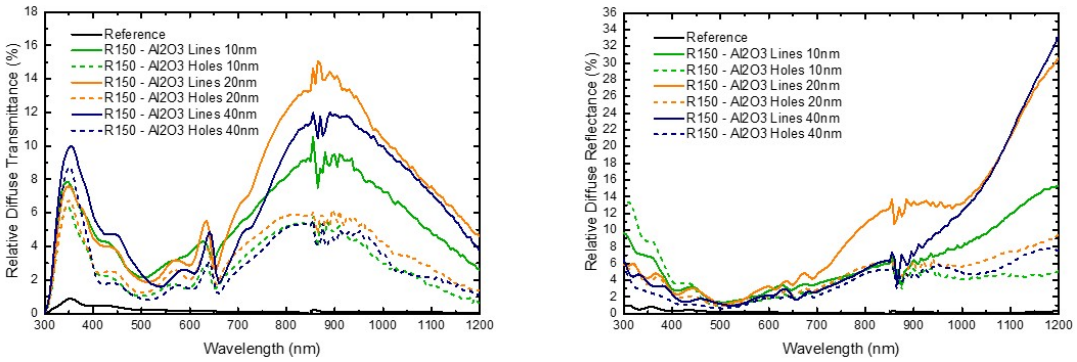
same relationship between lines and holes was observed. From these results, it is important to note that there was a shift in the peak between the materials. TiO_2 presented the biggest redshift compared to SiO_x, while Al_2O_3 displayed a smaller one. This may be explained due to the differences in the n of these materials, since TiO_2 presents an higher n than SiO_x and Al_2O_3, whose n values are similar. The metallic pillars resonate light with a fixed wavelength. Since the wavelength decreases in value in higher n mediums, then the emitted scattered light will have higher wavelengths for higher n encapsulation materials. The difference in scattering was not as evident in this series, with TiO_2 still presenting higher scattering at lower wavelengths. However, in the diffuse transmittance, the scattering at higher wavelengths was relatively similar in intensity, with SiO_x standing out in its peak, but TiO_2 having an higher intensity after the peak. In the reflectance component, SiO_x had a higher peak than the other materials but TiO_2 presented the same behaviour again after the peak.



(A) (B)

FIGURE 4.30: **a)** Relative diffuse transmittance spectra from the B series samples, and **b)** Relative diffuse reflectance spectra from the B series samples.

Finally, the diffuse transmittance and reflectance components from the C series were analyzed and the results can be seen in Fig. 4.31a) and b), respectively. In the last series, lines still presented an higher scattering than holes. The $20\,\mathrm{nm}$ thickness presented better results throughout both spectrums, with exception of the 300-$500\,\mathrm{nm}$ range in the transmittance component ($40\,\mathrm{nm}$ had slightly better results) and in the reflectance ($10\,\mathrm{nm}$ had slightly better results).



(A) (B)

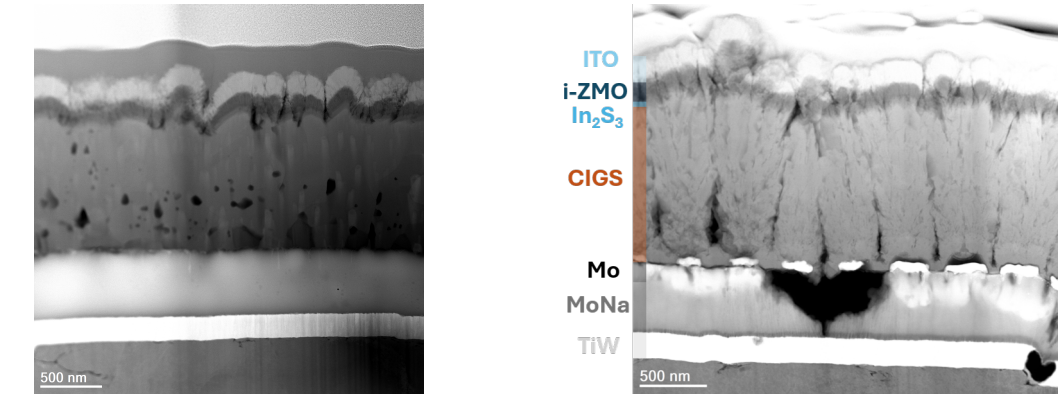
FIGURE 4.31: **a)** Relative diffuse transmittance spectra from the C series samples, and **b)** Relative diffuse reflectance spectra from the C series samples.

4.6. Encapsulated Au Pillars on SS Flexible Substrates Process Flow Development

To assess the viability of the Au pillar encapsulation and evaluate its effectiveness in preventing Au diffusion into the active layers, dielectric-encapsulated Au pillars were fabricated on SS TiW/MoNa/Mo substrates. However, this process flow was not developed and optimized in full by the time of writing.

In the encapsulated Au pillars on ITO process flow, the last step to remove the unpassivated metallic nanostructures was based on TechniEtch ACI2. This metal remover, despite effectively etching Au, also affects Mo. This chemical has a significant etching rate on Mo, making this step not viable for Mo-based substrates. Nevertheless, solar cells were produced in order to study the integration of these nanostructures in SS ultrathin flexible solar cells. The process flow was similar to the one developed on rigid substrates, with a $0.9\,\mu m$ CIGS absorber deposition. TEM was used to evaluate the cross-section of these cells, and both the reference sample and the encapsulated Au pillars cell can be seen in Fig. 4.32a) and b). In Fig. 4.32a), it is possible to observe a reference cell, where the back contact is intact and the deposition of the absorber is good, despite having some holes. However, when switching to the cell with the pillars, several side-effects happen. As visible in Fig. 4.32b), the Au wet ecth isotropically etches the back contact, reaching the TiW layer. Furthermore, the metallic pillars in this region are still present, which should have not happen because the wet etchant was in contact with them. This aspects confirm that the Au etch using TechniEtch ACI2 is not viable for Mo substrates and a new process must be studied. Another effect that was also visible in the CIGS layer with SiO_x pillars is the deposition in columns, which ends up also affecting the upper layers of the solar cell. Nonetheless, the integrity of the Au pillars was kept, and the dimensions of the pillars,

which correspond to the expected, suggest that no Au diffused into the CIGS layer. It is important to note that the encapsulation of these nanostructures was developed with a $10\,\mathrm{nm}$ Al_2O_3 layer, proving even the thinnest encapsulation was able to impede the Au diffusion into the absorber.



(A) (B)

FIGURE 4.32: Cross-sectional TEM images of the studied cells: **a)** reference; **b)** Au pillars cell.

In summary, a process flow for the fabrication of two different Au pillars architectures was developed and optimized for ITO-coated SLG substrates. Nevertheless, these could not be replicated to a SS TiW/MoNa/Mo CIGS solar cell, despite the side-experiment proved the encapsulation of Au to be possible throughout this architecture.

5. Conclusion and Future Work

The work in this thesis aimed to establish reproducible process flows for the fabrication of rear light-management structures, in rigid and flexible substrates, to potentially improve the optical performance of ultrathin CIGS solar cells. NIL was employed for the fabrication of these light-trapping structures as an industrial approach.

A process flow for the fabrication of SiO_x pillars on a TiW/MoNa/Mo-coated SS substrate was achieved. NIL was used to replicate the pillars pattern (r = 225 nm, a = 100 nm, and h = 150 nm) from a master stamp. For SiO_x RIE, different conditions were tested, including process T and plasma chemistries. During these tests, the process T had to be minimized to reduce substrate bending effects, and consequent changes in the reactivity of the etching, while the plasma chemistry was adjusted in order to minimize the amount of available F in the plasma, to prevent the formation of undesired residues in the Mo layer. The final resist strip was optimized by testing a combination of wet and dry etching processes, for which a combination of plasma ashing and O_2 strip was chosen for this step. Spectrophotometry measurements show an increase in diffuse reflectance of the Mo rear contact when integrating SiO_x pillars, indicating light scattering behavior, and potential optical path length enhancement once integrated in ultrathin CIGS solar cells. The complete CIGS solar cells were produced via sputtering on SS flexible substrates. An initial study was performed to evaluate the CIGS solar cell performance dependency on the absorber thickness. The thickness of the absorber was varied and its optoeletronic properties were evaluated. It was observed that the J_{sc} decreased with decreasing absorber thickness values, while the EQE also diminished predominantly in the NIR region, showing the impact of absorber thickness in light absorption. The fabricated SiO_x pillars were integrated on ultrathin flexible CIGS solar cells. The pillars showed an optical enhancement in the NIR region, showing potential optical benefits. Nonetheless, the electric properties of the cell were degraded. SEM analysis show disrupted CIGS growth due to the roughness of the structures, which may have contributed to the electric losses.

For bifacial solar cells, an Au pillar array encapsulated by a dielectric material was developed on ITO-coated SLG substrates. Two different architectures (R150 and R100) were studied, aiming to maximize the optical gain in: i) Front, and ii) Bifacial Illumination, respectively. Furthermore, two different contact opening architectures were employed: lines

and holes, to ensure the electrical contact between ITO and CIGS. Different nanofabrication steps were optimized, including Au and dielectric etching, removal of Au redeposition, RR removals and resist strips. The ion milling process was optimized by adjusting the etching angle to achieve a cylindrical-like morphology of the pillars and fully remove the Au redeposition around the structure, for which different angles and times were established depending on the etched architecture. The resist strip was optimized by testing wet and dry processes, for which a combination of plasma ashing and O_2 strip was chosen for this step. The pillars were encapsulated by SiO_x, Al_2O_3, and TiO_2. A second imprint was employed to pattern the contact openings on the encapsulated Au pillars. Both RIE and IBE processes were tested, with IBE presenting better material compatibility and versatility. At this stage, some Au pillars were left exposed in the opening areas, which were removed by a wet etchant, which was successful in removing all uncovered Au, even if only slightly. A final resist strip, consisting of plasma ashing, was carried out to remove all of the remaining resist. Morphological and topological characterization confirmed the target structural dimensions, and the ITO over-etch, resulting from the ion milling processes, which is not expected to degrade the electrical performance of this back contact. Optical evaluation showed the light scattering properties of the samples, through an increase in diffuse reflectance and transmittance, relative to a flat ITO back contact. The R100 architecture, designed for bifacial illumination, proved to be more compatible with rear illumination than the R150 one, despite still showing a lower total transmittance than the flat ITO reference. Non-significant differences in optical behavior were observed across the various dielectric materials. Another study was carried out to assess the integration of dielectric-encapsulated Au pillars on flexible SS TiW/MoNa/Mo substrates. Although a complete process flow was not yet optimized, the fabricated samples allowed the evaluation of the compatibility between the encapsulated metallic structures and the ultrathin CIGS solar cell. The analysis showed encapsulated Au pillars maintained their structural integrity after integration and no evidence of Au diffusion into the absorber was observed, even with a Al_2O_3 encapsulation thickness of only $10\,\mathrm{nm}$.

Regarding future work, CIGS deposition should be further adjusted to improve the absorber growth quality. The aim is to achieve a conformal deposition that minimizes electrical losses associated with the integration of SiO_x pillars, while ensuring that the texturization induced by these pillars does not compromise the morphology of the subsequent buffer and top layers. Concerning dielectric-encapsulated Au pillars on a Mo back contact, the fabrication should be further optimized, particularly regarding the wet etching step to

remove the exposed Au, while avoiding Mo etching. Some mitigation strategies include: i) the investigation of wet etchant solution chemistries fully compatible with Mo; ii) redesign of the fabrication process flow, in which a sacrificial layer is introduced in the first fabrication step, protecting the Mo surface throughout the whole process, until the final step where the sacrificial layer is removed by IBE, thus preventing Mo etch during the exposed Au removal.

Overall, this work contributed to the development of reproducible nanofabrication process flows for light-management architectures to be integrated in ultrathin CIGS solar cells, addressing both flexible and rigid substrates, as well as bifacial configurations. The results obtained demonstrate the potential of nanostructured rear interfaces to improve absorption in ultrathin cells, while also highlighting the challenges associated with preserving the electrical properties of the devices after integration. Although further optimization and complete device evaluation are still required, the developed process flows establish a strong foundation for the integration of rear light-management strategies in ultrathin solar cells.

References

[1] S. K. Depren, M. T. Kartal, N. Ç. Çelikdemir, and Ö. Depren, "Energy consumption and environmental degradation nexus: A systematic review and meta-analysis of fossil fuel and renewable energy consumption," *Ecological Informatics*, vol. 70, p. 101747, 2022. [Cited on page 1.]

[2] Y. Chen, D. Chen, P. P. Altermatt, S. Zhang, L. Wang, X. Zhang, J. Xu, Z. Feng, H. Shen, and P. J. Verlinden, "Technology evolution of the photovoltaic industry: learning from history and recent progress," *Progress in Photovoltaics: Research and Applications*, vol. 31, no. 12, pp. 1194–1204, 2023. [Cited on page 1.]

[3] M. Di Sabatino, R. Hendawi, and A. S. Garcia, "Silicon solar cells: trends, manufacturing challenges, and ai perspectives," *Crystals*, vol. 14, no. 2, p. 167, 2024. [Cited on page 1.]

[4] K. Liu, X. Xu, R. Zhang, L. Kong, W. Wang, and W. Deng, "Impact of urban form on building energy consumption and solar energy potential: A case study of residential blocks in jianhu, china," *Energy and Buildings*, vol. 280, p. 112727, 2023. [Cited on page 1.]

[5] A. Faes, A. Virtuani, H. Quest, L. Maturi, A. Scognamiglio, F. Frontini, A. Schlueter, N. Martin-Chivelet, A. Reinders, and C. Ballif, "Building-integrated photovoltaics," *Nature Reviews Clean Technology*, vol. 1, no. 5, pp. 333–350, 2025. [Cited on page 1.]

[6] S. Aguacil, S. Duque, S. Lufkin, and E. Rey, "Designing with building-integrated photovoltaics (bipv): A pathway to decarbonize residential buildings," *Journal of Building Engineering*, vol. 96, p. 110486, 2024. [Cited on page 1.]

[7] R. Noufi and K. Zweibel, "High-efficiency cdte and cigs thin-film solar cells: highlights and challenges," in *2006 IEEE 4th World Conference on Photovoltaic Energy Conference*, vol. 1. IEEE, 2006, pp. 317–320. [Cited on pages 1 and 5.]

[8] W. Shafarman, S. Siebentritt, and L. Stolt, "In handbook of photovoltaic science and engineering 2nd ed.(eds luque, a. & hegedus, s.) ch. 13," 2011. [Cited on page 1.]

[9] T. Lopes, J. Teixeira, M. Curado, B. Ferreira, A. Oliveira, J. Cunha, M. Monteiro, A. Violas, J. Barbosa, P. Sousa *et al.*, "Cu (in, ga) se2 based ultrathin solar cells the

pathway from lab rigid to large scale flexible technology," *npj Flexible Electronics*, vol. 7, no. 1, p. 4, 2023. [Cited on pages 2, 7, and 9.]

[10] A. J. Oliveira, J. P. Teixeira, D. Ramos, P. A. Fernandes, and P. M. Salomé, "Exploiting the optical limits of thin-film solar cells: a review on light management strategies in cu (in, ga) se2," *Advanced Photonics Research*, vol. 3, no. 6, p. 2100190, 2022. [Cited on pages vi, 2, 9, 10, 12, 13, 14, 15, 16, 17, and 18.]

[11] F. Kessler and D. Rudmann, "Technological aspects of flexible cigs solar cells and modules," *Solar energy*, vol. 77, no. 6, pp. 685–695, 2004. [Cited on page 3.]

[12] T. Feurer, P. Reinhard, E. Avancini, B. Bissig, J. Löckinger, P. Fuchs, R. Carron, T. P. Weiss, J. Perrenoud, S. Stutterheim *et al.*, "Progress in thin film cigs photovoltaics–research and development, manufacturing, and applications," *Progress in Photovoltaics: Research and Applications*, vol. 25, no. 7, pp. 645–667, 2017. [Cited on page 3.]

[13] A. Gerthoffer, F. Roux, F. Emieux, P. Faucherand, H. Fournier, L. Grenet, and S. Perraud, "Cigs solar cells on flexible ultra-thin glass substrates: Characterization and bending test," *Thin Solid Films*, vol. 592, pp. 99–104, 2015. [Cited on page 3.]

[14] D. J. Schroeder and A. A. Rockett, "Electronic effects of sodium in epitaxial cuin 1-x ga x se 2," *Journal of Applied Physics*, vol. 82, no. 10, pp. 4982–4985, 1997. [Cited on page 3.]

[15] P. Salomé, V. Fjällström, A. Hultqvist, and M. Edoff, "Na doping of cigs solar cells using low sodium-doped mo layer," *IEEE Journal of Photovoltaics*, vol. 3, no. 1, pp. 509–513, 2012. [Cited on page 3.]

[16] R. Wuerz, A. Eicke, F. Kessler, P. Rogin, and O. Yazdani-Assl, "Alternative sodium sources for cu (in, ga) se2 thin-film solar cells on flexible substrates," *Thin Solid Films*, vol. 519, no. 21, pp. 7268–7271, 2011. [Cited on page 4.]

[17] B. Salhi, "The photovoltaic cell based on cigs: principles and technologies," *Materials*, vol. 15, no. 5, p. 1908, 2022. [Cited on pages 4 and 6.]

[18] X. Shao, S. Shi, B. Liang, L. Chen, T. Qi, X. Yuan, S. Yu, W. Tang, C. Yang, and W. Li, "Alkali metal pretreatment for precise na doping and v oc improvement in cigs thin-film solar cells," *ACS Applied Materials & Interfaces*, vol. 16, no. 23, pp. 30 147–30 156, 2024. [Cited on page 4.]

[19] X. Ma, D. Liu, L. Yang, S. Zuo, and M. Zhou, "Molybdenum (mo) back contacts for cigs solar cells," in *Eighth International Conference on Thin Film Physics and Applications*, vol. 9068. SPIE, 2013, pp. 192–202. [Cited on page 4.]

[20] P. K. Dakua, A. NagaJyothi, K. G. Sree, N. Rohini, N. Komala, and M. Tarun, "Investigation of possible front contact materials for efficient pv device using cigs as an active layer," *Journal of Optics*, pp. 1–13, 2024. [Cited on pages 4 and 6.]

[21] P. Salomé, J. Malaquias, P. Fernandes, and A. d. Cunha, "Mo bilayer for thin film photovoltaics revisited," *Journal of Physics D: Applied Physics*, vol. 43, no. 34, p. 345501, 2010. [Cited on page 4.]

[22] K. H. Ong, R. Agileswari, B. Maniscalco, P. Arnou, C. C. Kumar, J. W. Bowers, and M. B. Marsadek, "Review on substrate and molybdenum back contact in cigs thin film solar cell," *International Journal of Photoenergy*, vol. 2018, no. 1, p. 9106269, 2018. [Cited on page 4.]

[23] P. Pradhan, P. Aryal, A.-R. Ibdah, P. Koirala, J. Li, N. J. Podraza, A. A. Rockett, S. Marsillac, and R. W. Collins, "Effect of molybdenum deposition temperature on the performance of cuin1- xgaxse2 solar cells," in *2015 IEEE 42nd Photovoltaic Specialist Conference (PVSC)*. IEEE, 2015, pp. 1–4. [Cited on page 4.]

[24] Z.-H. Li, E.-S. Cho, and S. J. Kwon, "Molybdenum thin film deposited by in-line dc magnetron sputtering as a back contact for cu (in, ga) se2 solar cells," *Applied surface science*, vol. 257, no. 22, pp. 9682–9688, 2011. [Cited on page 4.]

[25] A. Violas, A. Oliveira, P. Fernandes, P. Salomé, and J. Teixeira, "Cigs bifacial solar cells with novel rear architectures: Simulation point of view and the creation of a digital twin," *Solar Energy Materials and Solar Cells*, vol. 272, p. 112899, 2024. [Cited on page 4.]

[26] S. A. Pethe, E. Takahashi, A. Kaul, and N. G. Dhere, "Effect of sputtering process parameters on film properties of molybdenum back contact," *Solar energy materials and solar cells*, vol. 100, pp. 1–5, 2012. [Cited on page 4.]

[27] T. Wada, N. Kohara, S. Nishiwaki, and T. Negami, "Characterization of the cu (in, ga) se2/mo interface in cigs solar cells," *Thin solid films*, vol. 387, no. 1-2, pp. 118–122, 2001. [Cited on page 4.]

[28] A. Khamis, N. Rodzi, and N. Naharuddin, “Absorber layer improvement and performance analysis of cigs thin-film solar cell.” *Journal of Ovonic Research*, vol. 20, no. 3, 2024. [Cited on page 4.]

[29] N. Mufti, T. Amrillah, A. Taufiq, Sunaryono, Aripriharta, M. Diantoro, Zulhadjri, and H. Nur, “Review of cigs-based solar cells manufacturing by structural engineering,” *Solar Energy*, vol. 207, pp. 1146–1157, 2020. [Online]. Available: https://www.sciencedirect.com/science/article/pii/S0038092X20307970 [Cited on pages 4 and 5.]

[30] A. Labadi, S. Tobbeche, O. Saidani, M. Bouladame, and F. Brahimi, “Efficiency improvement of cigs solar cells with znse buffer layer and sns bsf layer,” *Micro and Nanostructures*, p. 208257, 2025. [Cited on pages 4 and 6.]

[31] J. Ramanujam and U. P. Singh, “Copper indium gallium selenide based solar cells–a review,” *Energy & Environmental Science*, vol. 10, no. 6, pp. 1306–1319, 2017. [Cited on pages 4 and 5.]

[32] J. Keller, K. Kiselman, O. Donzel-Gargand, N. M. Martin, M. Babucci, O. Lundberg, E. Wallin, L. Stolt, and M. Edoff, “High-concentration silver alloying and steep back-contact gallium grading enabling copper indium gallium selenide solar cell with 23.6% efficiency,” *Nature Energy*, vol. 9, no. 4, pp. 467–478, 2024. [Cited on page 5.]

[33] M. Tomasik, N. Mangan, and J. Grossman, “Photovoltaic efficiency of an indirect bandgap material,” in *APS March Meeting Abstracts*, vol. 2015, 2015, pp. L34–011. [Cited on page 5.]

[34] J. Pettersson, T. Törndahl, C. Platzer-Björkman, A. Hultqvist, and M. Edoff, “The influence of absorber thickness on cu (in, ga) se_2 solar cells with different buffer layers,” *IEEE journal of photovoltaics*, vol. 3, no. 4, pp. 1376–1382, 2013. [Cited on page 5.]

[35] H. Kang, “Crystalline silicon vs. amorphous silicon: the significance of structural differences in photovoltaic applications,” *IOP Conference Series: Earth and Environmental Science*, vol. 726, p. 012001, 04 2021. [Cited on page 5.]

[36] M. Islam, N. Kassim, A. Alkahtani, and N. Amin, *Assessing the Impact of Spectral Irradiance on the Performance of Different Photovoltaic Technologies*, 05 2021. [Cited on page 5.]

[37] A. M. Alfantazi and R. Moskalyk, “Processing of indium: a review,” *Minerals Engineering*, vol. 16, no. 8, pp. 687–694, 2003. [Cited on page 5.]

[38] C. Onwudinanti, R. Vismara, O. Isabella, L. Grenet, F. Emieux, and M. Zeman, “Advanced light management based on periodic textures for cu (in, ga) se_2 thin-film solar cells,” *Optics Express*, vol. 24, no. 6, pp. A693–A707, 2016. [Cited on page 5.]

[39] W. Shafarman, S. Sieventritt, and L. Stolt, *Cu(InGa)Se₂ Solar Cells*, 2nd ed. John Wiley & Sons, 2011, ch. 13, pp. 546–599. [Cited on pages vi and 5.]

[40] M. Theelen and F. Daume, “Stability of cu (in, ga) se2 solar cells: A literature review,” *Solar Energy*, vol. 133, pp. 586–627, 2016. [Cited on page 5.]

[41] K. Machkih, R. Oubaki, and M. Makha, “A review of cigs thin film semiconductor deposition via sputtering and thermal evaporation for solar cell applications,” *Coatings*, vol. 14, no. 9, 2024. [Online]. Available: https://www.mdpi.com/2079-6412/14/9/1088 [Cited on page 5.]

[42] S. Aksu, J. Wang, and B. M. Basol, “Electrodeposition of in–se and ga–se thin films for preparation of cigs solar cells,” *Electrochemical and Solid-State Letters*, vol. 12, no. 5, p. D33, 2009. [Cited on page 5.]

[43] C.-H. Huang, W.-J. Chuang, C.-P. Lin, Y.-L. Jan, and Y.-C. Shih, “Deposition technologies of high-efficiency cigs solar cells: development of two-step and co-evaporation processes,” *Crystals*, vol. 8, no. 7, p. 296, 2018. [Cited on page 6.]

[44] Y. Singh, S. Rani, R. Parmar, R. Kumari, M. Kumar, A. B. Sairam, V. Singh *et al.*, “Sb2se3 heterostructure solar cells: Techniques to improve efficiency,” *Solar Energy*, vol. 249, pp. 174–182, 2023. [Cited on page 6.]

[45] M. M. Islam, S. Ishizuka, A. Yamada, K. Sakurai, S. Niki, T. Sakurai, and K. Akimoto, “Cigs solar cell with mbe-grown zns buffer layer,” *Solar energy materials and solar cells*, vol. 93, no. 6-7, pp. 970–972, 2009. [Cited on page 6.]

[46] D. Hariskos, S. Spiering, and M. Powalla, “Buffer layers in cu (in, ga) se2 solar cells and modules,” *Thin solid films*, vol. 480, pp. 99–109, 2005. [Cited on page 6.]

[47] G. Siddharth, V. Garg, B. S. Sengar, and S. Mukherjee, “Progress in thin film solar cell and advanced technologies for performance improvement,” 2022. [Cited on page 6.]

[48] H. I. Abdalmageed, M. Fedawy, and M. H. Aly, “Effect of absorber layer bandgap of cigs-based solar cell with (cds/zns) buffer layer,” in *journal of physics: conference series*, vol. 2128, no. 1. IOP Publishing, 2021, p. 012009. [Cited on page 6.]

[49] N. Matsuo, D. Hironiwa, J. Chantana, N. Sakai, T. Kato, H. Sugimoto, and T. Minemoto, “Evaluation of sputtering damage in cu2znsn (s, se) 4 solar cells with cds and (cd, zn) s buffer layers by photoluminescence measurement,” *Japanese Journal of Applied Physics*, vol. 54, no. 4, p. 042302, 2015. [Cited on page 6.]

[50] J. H. Park, Y. Jo, A. Cho, I. Jeong, J. G. An, K. Kim, S. K. Ahn, D. Shin, and J.-S. Cho, “Enhancement of cd-free all-dry-processed cu (in1-x, gax) se2 thin-film solar cells by simultaneous adoption of an enlarged bandgap absorber and tunable bandgap zn1-xmgxo buffer,” *Energy & Environmental Materials*, vol. 8, no. 1, p. e12796, 2025. [Cited on page 6.]

[51] M. Gloeckler, A. Fahrenbruch, and J. Sites, “Proceedings of the 3rd world conference on photovoltaic energy conversion,” in *Proceedings of the 3rd World Conference on Photovoltaic Energy Conversion, Osaka, Japan*, 2003, pp. 11–18. [Cited on page 6.]

[52] S. Bhattarai, A. Sharma, D. Muchahary, D. Gogoi, and T. Das, “Numerical simulation study for efficiency enhancement of doubly graded perovskite solar cell,” *Optical Materials*, vol. 118, p. 111285, 2021. [Cited on page 6.]

[53] A. R. Zanatta, “The shockley–queisser limit and the conversion efficiency of silicon-based solar cells,” *Results in optics*, vol. 9, p. 100320, 2022. [Cited on page 7.]

[54] S. Rühle, “Tabulated values of the shockley–queisser limit for single junction solar cells,” *Solar energy*, vol. 130, pp. 139–147, 2016. [Cited on page 7.]

[55] F. ISE, “Fraunhofer ise photovoltaics report,” 2026. [Cited on page 7.]

[56] S. Editor, “What are cigs solar panels and how do they compare to silicon panels,” 2025. [Cited on page 7.]

[57] A. Ali, B. Kadiri-English, D.-H. Son, J. Lee, J.-K. Kang, D.-K. Hwang, S.-J. Sung, K.-J. Yang, and D.-H. Kim, “Bifacial chalcogenide thin-film solar cells: Concepts, challenges, and opportunities,” *Solar RRL*, vol. 9, no. 24, p. e202500685, 2025. [Cited on pages 7 and 8.]

[58] N. Alhammadi, E. Rodriguez-Ubinas, S. Alzarouni, and M. Alantali, "Building-integrated photovoltaics in hot climates: Experimental study of cigs and c-si modules in bipv ventilated facades," *Energy Conversion and Management*, vol. 274, p. 116408, 2022. [Cited on page 7.]

[59] S.-C. Yang, T.-Y. Lin, M. Ochoa, H. Lai, R. Kothandaraman, F. Fu, A. N. Tiwari, and R. Carron, "Efficiency boost of bifacial cu (in, ga) se2 thin-film solar cells for flexible and tandem applications with silver-assisted low-temperature process," *Nature Energy*, vol. 8, no. 1, pp. 40–51, 2023. [Cited on pages 7 and 8.]

[60] R. Peleg, "Researchers fabricate bifacial perovskite-cigs tandem solar cell and develop a new low-temperature production process," 2022. [Cited on pages vi and 8.]

[61] L. Chen, J. Lee, and W. N. Shafarman, "The comparison of (ag, cu)(in, ga) se $_2$ and cu (in, ga) se $_2$ thin films deposited by three-stage coevaporation," *IEEE Journal of Photovoltaics*, vol. 4, no. 1, pp. 447–451, 2013. [Cited on page 8.]

[62] L. M. Mansfield, A. Kanevce, S. P. Harvey, K. Bowers, C. Beall, S. Glynn, and I. L. Repins, "Efficiency increased to 15.2% for ultra-thin cu (in, ga) se2 solar cells," *Progress in Photovoltaics: Research and Applications*, vol. 26, no. 11, pp. 949–954, 2018. [Cited on page 9.]

[63] E. Camarillo Abad, H. J. Joyce, and L. C. Hirst, "Light management for ever-thinner photovoltaics: A tutorial review," *APL Photonics*, vol. 9, no. 1, 2024. [Cited on pages 10 and 12.]

[64] E. Ribeiro, A. Violas, T. Lopes, J. Fernandes, J. Teixeira, P. Fernandes, and P. Salomé, "A review of nanoimprint lithography for improving the optical performance of solar cells," *Microelectronic Engineering*, p. 112455, 2026. [Cited on pages vi, 11, 18, and 19.]

[65] L. A. Kosyachenko, X. Mathew, P. Paulson, V. Y. Lytvynenko, and O. Maslyanchuk, "Optical and recombination losses in thin-film cu (in, ga) se2 solar cells," *Solar energy materials and solar cells*, vol. 130, pp. 291–302, 2014. [Cited on pages 11 and 12.]

[66] A. Khadir, A. Kouzou, and M. K. Abdelhafidi, "Effect of anti-reflective coating on cigs solar cells performance," in *2020 17th International Multi-Conference on Systems, Signals & Devices (SSD)*. IEEE, 2020, pp. 621–625. [Cited on pages vi and 12.]

[67] J. Nishinaga, T. Koida, S. Ishizuka, Y. Kamikawa, H. Takahashi, M. Iioka, H. Higuchi, Y. Ueno, H. Shibata, and S. Niki, "Effects of long-term heat-light soaking on cu (in, ga) se2 solar cells with kf postdeposition treatment," *Applied Physics Express*, vol. 10, no. 9, p. 092301, 2017. [Cited on pages vi and 12.]

[68] O. Poncelet, R. Kotipalli, B. Vermang, A. Macleod, L. A. Francis, and D. Flandre, "Optimisation of rear reflectance in ultra-thin cigs solar cells towards> 20% efficiency," *Solar Energy*, vol. 146, pp. 443–452, 2017. [Cited on page 13.]

[69] L. Gouillart, A. Cattoni, J. Goffard, F. Donsanti, G. Patriarche, M. Jubault, N. Naghavi, and S. Collin, "Development of reflective back contacts for high-efficiency ultrathin cu (in, ga) se2 solar cells," *Thin Solid Films*, vol. 672, pp. 1–6, 2019. [Cited on pages vi and 13.]

[70] M. A. Ashraf and I. Alam, "Numerical simulation of cigs, cisse and czts-based solar cells with in2s3 as buffer layer and au as back contact using scaps 1d," *Engineering Research Express*, vol. 2, no. 3, p. 035015, 2020.

[71] D. Fraga, T. S. Lyubenova, A. Rey, I. Calvet, R. Martí, and J. B. Carda, "Ceramic enamels as new back contacts for cu (in, ga) se2-based photovoltaic tile," *International Journal of Applied Ceramic Technology*, vol. 12, no. 4, pp. 728–737, 2015.

[72] K. Orgassa, H. W. Schock, and J. Werner, "Alternative back contact materials for thin film cu (in, ga) se2 solar cells," *Thin Solid Films*, vol. 431, pp. 387–391, 2003. [Cited on page 13.]

[73] P. Salomé, H. Rodriguez-Alvarez, and S. Sadewasser, "Incorporation of alkali metals in chalcogenide solar cells," *Solar Energy Materials and Solar Cells*, vol. 143, pp. 9–20, 2015. [Cited on page 13.]

[74] S. H. Zaidi, D. S. Ruby, and J. M. Gee, "Characterization of random reactive ion etched-textured silicon solar cells," *IEEE Transactions on electron devices*, vol. 48, no. 6, pp. 1200–1206, 2001. [Cited on page 14.]

[75] S. Mokkapati and K. Catchpole, "Nanophotonic light trapping in solar cells," *Journal of applied physics*, vol. 112, no. 10, 2012. [Cited on page 14.]

[76] E. Yablonovitch, "Statistical ray optics," *Journal of the Optical Society of America*, vol. 72, no. 7, pp. 899–907, 1982. [Cited on page 14.]

[77] M. A. García, "Surface plasmons in metallic nanoparticles: fundamentals and applications," *Journal of Physics D: Applied Physics*, vol. 44, no. 28, p. 283001, 2011. [Cited on page 15.]

[78] S. A. Maier *et al.*, *Plasmonics: fundamentals and applications*. Springer, 2007, vol. 1. [Cited on page 15.]

[79] J. Goffard, C. Colin, F. Mollica, A. Cattoni, C. Sauvan, P. Lalanne, J.-F. Guillemoles, N. Naghavi, and S. Collin, "Light trapping in ultrathin cigs solar cells with nanostructured back mirrors," *IEEE journal of photovoltaics*, vol. 7, no. 5, pp. 1433–1441, 2017. [Cited on pages vi, 15, and 16.]

[80] A. I. Kuznetsov, A. E. Miroshnichenko, M. L. Brongersma, Y. S. Kivshar, and B. Luk'yanchuk, "Optically resonant dielectric nanostructures," *Science*, vol. 354, no. 6314, p. aag2472, 2016. [Cited on page 17.]

[81] M. Schmid, "Review on light management by nanostructures in chalcopyrite solar cells," *Semiconductor Science and Technology*, vol. 32, no. 4, p. 043003, 2017. [Cited on page 17.]

[82] S. Jahani and Z. Jacob, "All-dielectric metamaterials," *Nature nanotechnology*, vol. 11, no. 1, pp. 23–36, 2016. [Cited on page 17.]

[83] W. G. van Sark, J. de Wild, J. K. Rath, A. Meijerink, and R. E. Schropp, "Upconversion in solar cells," *Nanoscale research letters*, vol. 8, no. 1, p. 81, 2013. [Cited on page 17.]

[84] J. Day, S. Senthilarasu, and T. K. Mallick, "Improving spectral modification for applications in solar cells: A review," *Renewable Energy*, vol. 132, pp. 186–205, 2019. [Cited on page 17.]

[85] D. Timmerman, I. Izeddin, P. Stallinga, I. Yassievich, and T. Gregorkiewicz, "Space-separated quantum cutting with silicon nanocrystals for photovoltaic applications," *Nature Photonics*, vol. 2, no. 2, pp. 105–109, 2008. [Cited on page 17.]

[86] T. Trupke, M. Green, and P. Würfel, "Improving solar cell efficiencies by up-conversion of sub-band-gap light," *Journal of applied physics*, vol. 92, no. 7, pp. 4117–4122, 2002. [Cited on page 17.]

[87] Z. Xiong, J. Gong, Y. Xiong, Y. Lan, M. Yin, Z. Ding, Z. Zhang, and X. Xiao, "Constructing a spectral down converter to enhance cu (in, ga) se2 solar cell performance using yttrium aluminum garnet: Ce3+ ceramics," *Solar RRL*, vol. 4, no. 5, p. 1900518, 2020. [Cited on page 17.]

[88] B. McKenna and R. C. Evans, "Towards efficient spectral converters through materials design for luminescent solar devices," *Advanced Materials*, vol. 29, no. 28, p. 1606491, 2017. [Cited on page 17.]

[89] S. Tripathy, J. Rodrigues, and N. G. Shimpi, "Top-down and bottom-up approaches for synthesis of nanoparticles," *Nanobiomaterials Perspect. Med. Appl. Diagn. Treat. Dis*, vol. 145, pp. 92–130, 2023. [Cited on page 18.]

[90] P. Iqbal, J. A. Preece, and P. M. Mendes, "Nanotechnology: the "top-down" and "bottom-up" approaches," *Supramolecular chemistry: from molecules to nanomaterials*, 2012. [Cited on page 18.]

[91] E. Sharma, R. Rathi, J. Misharwal, B. Sinhmar, S. Kumari, J. Dalal, and A. Kumar, "Evolution in lithography techniques: microlithography to nanolithography," *Nanomaterials*, vol. 12, no. 16, p. 2754, 2022. [Cited on page 18.]

[92] D. Kazazis, J. G. Santaclara, J. van Schoot, I. Mochi, and Y. Ekinci, "Extreme ultraviolet lithography," *Nature Reviews Methods Primers*, vol. 4, no. 1, p. 84, 2024. [Cited on page 18.]

[93] S. Ji, S. Park, J. Choe, J. Kim, J. Park, S. W. Bae, J. M. Oh, J. Kim, H. S. Woo, C.-W. Lee *et al.*, "Isotropic wet etching of molybdenum revealed by liquid-phase transmission electron microscopy," *Surfaces and Interfaces*, p. 107593, 2025. [Cited on page 19.]

[94] M. J. Madou, *Fundamentals of microfabrication: the science of miniaturization*. CRC press, 2018. [Cited on page 19.]

[95] S. Lindström, "An all-sputtering process and equipment for cigs solar cells: Productivity enhancment and cost reduction by highly automated equipment," *Vakuum in Forschung und Praxis*, vol. 25, no. 5, pp. 43–45, 2013. [Cited on page 21.]

[96] N. E. I. Boukortt, S. Patanè, and Y. M. Abdulraheem, "Numerical investigation of cigs thin-film solar cells," *Solar energy*, vol. 204, pp. 440–447, 2020. [Cited on page 22.]

[97] I. Nesterenko, B. Kalas, T. D. Dao, J. Schulze, and N. Andrianov, “Mechanism of selective sio2/photoresist reactive ion etching in an inductively coupled plasma operated in a c4f8/h2 gas mixture,” *Applied Physics Letters*, vol. 126, no. 3, 2025. [Cited on page 32.]

[98] H.-H. Doh, J.-H. Kim, K.-W. Whang, and S.-H. Lee, “Effect of hydrogen addition to fluorocarbon gases (cf4, c4f8) in selective sio2/si etching by electron cyclotron resonance plasma,” *Journal of Vacuum Science & Technology A: Vacuum, Surfaces, and Films*, vol. 14, no. 3, pp. 1088–1091, 1996. [Cited on page 36.]

[99] R. Carron, E. Avancini, T. Feurer, B. Bissig, P. A. Losio, R. Figi, C. Schreiner, M. Bürki, E. Bourgeois, Z. Remes *et al.*, “Refractive indices of layers and optical simulations of cu (in, ga) se2 solar cells,” *Science and Technology of advanced MaTerialS*, vol. 19, no. 1, pp. 396–410, 2018. [Cited on page 40.]

[100] T. Green, “Gold etching for microfabrication,” *Gold Bulletin*, vol. 47, no. 3, pp. 205–216, 2014. [Cited on page 48.]

[101] D. Jonker, Z. Jafari, J. Winczewski, C. Eyovge, J. Berenschot, N. Tas, J. Gardeniers, I. De Leon, and A. Susarrey-Arce, “A wafer-scale fabrication method for three-dimensional plasmonic hollow nanopillars,” *Nanoscale advances*, vol. 3, no. 17, pp. 4926–4939, 2021. [Cited on page 48.]